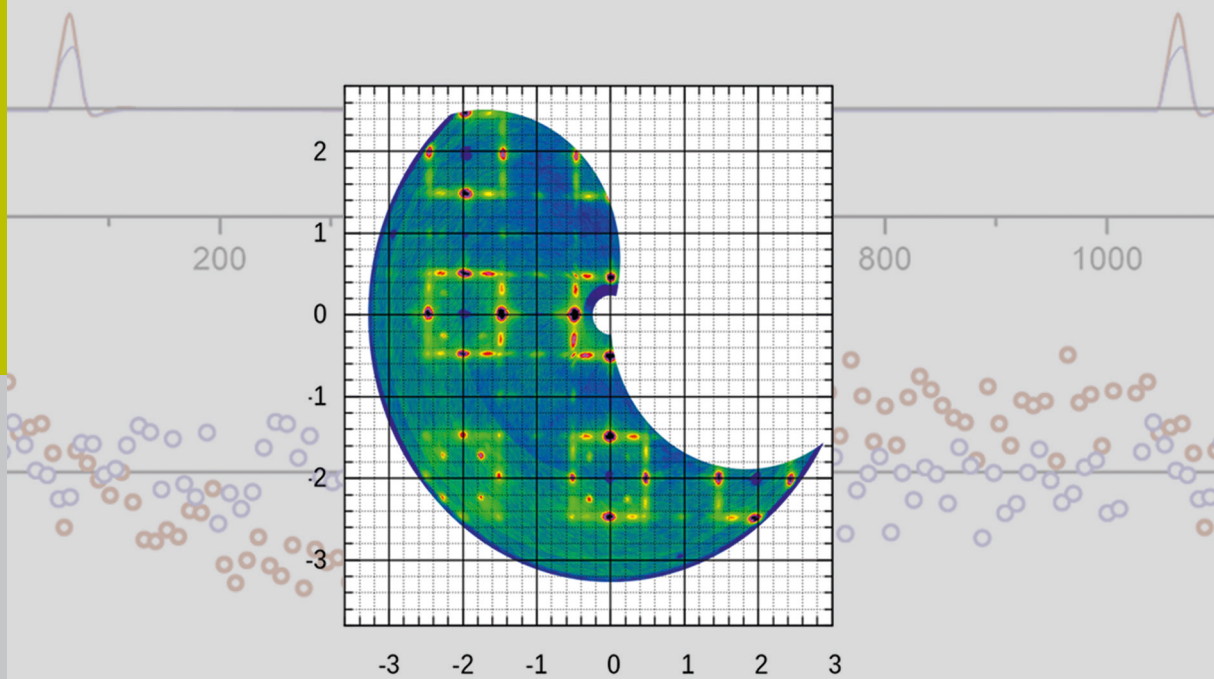


# Crystal growth and scattering studies on two ferrites

Shilpa Adiga



# **Crystal growth and scattering studies on two ferrites**

Von der Fakultät für Mathematik, Informatik und Naturwissenschaften der RWTH Aachen University zur Erlangung des akademischen Grades eines Doktors der Naturwissenschaften genehmigte Dissertation.

vorgelegt von  
Master of Science in Physics

**Shilpa Adiga**

aus Bengaluru, Indien

Berichter: Juniorprofessor Dr. M. Angst  
Universitätsprofessor Dr. U. Klemradt

Tag der mündlichen Prüfung: 22. Oktober 2015

Diese Dissertation ist auf den Internetseiten der Universitätsbibliothek online verfügbar.



Forschungszentrum Jülich GmbH  
Peter Grünberg Institute (PGI)  
Scattering Methods (PGI-4 / JCNS-2)

# Crystal growth and scattering studies on two ferrites

Shilpa Adiga

Schriften des Forschungszentrums Jülich  
Reihe Schlüsseltechnologien / Key Technologies

Band / Volume 135

---

ISSN 1866-1807

ISBN 978-3-95806-183-5



Bibliographic information published by the Deutsche Nationalbibliothek.  
The Deutsche Nationalbibliothek lists this publication in the Deutsche  
Nationalbibliografie; detailed bibliographic data are available in the  
Internet at <http://dnb.d-nb.de>.

Publisher and Distributor:	Forschungszentrum Jülich GmbH Zentralbibliothek 52425 Jülich Tel: +49 2461 61-5368 Fax: +49 2461 61-6103 Email: <a href="mailto:zb-publikation@fz-juelich.de">zb-publikation@fz-juelich.de</a> <a href="http://www.fz-juelich.de/zb">www.fz-juelich.de/zb</a>
Cover Design:	Grafische Medien, Forschungszentrum Jülich GmbH
Printer:	Grafische Medien, Forschungszentrum Jülich GmbH
Copyright:	Forschungszentrum Jülich 2016

Schriften des Forschungszentrums Jülich  
Reihe Schlüsseltechnologien / Key Technologies, Band / Volume 135

D 82 (Diss. RWTH Aachen University, 2015)

ISSN 1866-1807  
ISBN 978-3-95806-183-5

The complete volume is freely available on the Internet on the Jülicher Open Access Server (JuSER)  
at [www.fz-juelich.de/zb/openaccess](http://www.fz-juelich.de/zb/openaccess).



This is an Open Access publication distributed under the terms of the [Creative Commons Attribution License 4.0](https://creativecommons.org/licenses/by/4.0/),  
which permits unrestricted use, distribution, and reproduction in any medium, provided the original work is properly cited.

# Abstract

In this thesis I will describe investigations of two ferrite systems:

## (1) A detailed ferroelectric study of magnetite ( $\text{Fe}_3\text{O}_4$ )

Multiferroics, consisting of both ferroelectric and ferromagnetic phases, have attracted scientific and technological interest due possible magnetoelectric coupling between the phases. Such materials are very rare though, as conventional ferroelectricity requires an empty d-shell, preventing the presence of magnetism. Among unconventional mechanisms leading to ferroelectricity, multiferroicity due to charge ordering (CO) is a strong candidate for practical applications. However, proven examples are very rare as of yet. The 120 K Verwey transition ( $T_V$ ) in magnetite, reported in 1939, is the classical example for charge ordering. Despite controversies regarding the existence of CO, magnetite has been proposed as one of the CO-based multiferroics. Although early experiments already indicated for example a magnetoelectric effect, those studies were mainly focused on complex low temperature structure rather than possible multiferroicity.

In order to study the ferroelectric properties of magnetite by dielectric spectroscopy, a new dielectric measurement set-up was built at the institute. After an introduction and the description of experimental techniques, this thesis begins with the presentation of our newly built dielectric set-up and of the performed test experiments to standardize measurements of the dielectric constant.

The Verwey transition is very sensitive to oxygen stoichiometry. The oxygen stoichiometry was tuned by appropriate gas mixtures of  $\text{CO}_2$  and CO or  $\text{Ar}(\text{H}_2)_{4\%}$ . I first investigated appropriate ratios of  $\text{CO}_2/\text{Ar}(\text{H}_2)_{4\%}$  at high temperature on polycrystalline samples and confirmed the phase purity by x-ray diffraction. Verwey transition was characterized primarily by thermo-remanent magnetization and specific heat. The results obtained from the basic macroscopic analysis were used for the growth of high quality crystals by optical floating zone method. Proposed low temperature relaxor ferroelectric property of magnetite was studied by neutron and high energy X-ray diffuse scattering experiments. The observed weak diffuse scattering by neutron diffraction, which was absent in high energy X-ray studies, indicated that it is magnetic in origin.

For the first time, a time resolved X-ray diffraction technique has been implemented to test the switchability of the polar structure by application of an electric field in magnetite. The observed change in the intensity of the Bragg reflection to its Friedel mate (reflection related by inversion symmetry) constitutes to the first microscopic proof of ferroic behavior of classical magnetite.

## (2) Study of various physical properties of oxygen deficient strontium ferrite ( $\text{SrFeO}_{3-\delta}$ ).

Colossal magnetoresistance effect, i.e., the huge change in the electrical resistance by the application of magnetic field is a key to the next generation of magnetic memory devices. The oxygen deficient strontium ferrite ( $\text{SrFeO}_{3-\delta}$ ,  $\delta=0-0.5$ ) system exhibits various types of magnetoresistance effect depending on the presence of different magnetic phases. Oxygen deficient  $\text{SrFeO}_{3-\delta}$  crystals with  $\delta = 0.27$  and  $\delta = 0.35$  (as determined by infrared absorption) were grown by optical floating zone method using different growth conditions. This oxide system contains a mixture of Fe ions in tetravalent and trivalent states. Anomalies around  $\sim 70$  K,  $\sim 230$  K and  $\sim 130$  K observed by magnetization measurements indicated the presence of a tetragonal, orthorhombic and cubic phase respectively. Presence of these phases were confirmed by further microscopic measurements by neutron scattering. Two new magnetic phases at the propagation vector  $\mathbf{k} = (0.25 \ 0.25 \ 0.25)_c$  and  $(0.25 \ 0 \ 0.15)_c$  were observed by our detailed neutron diffraction experiments with polarization analysis. Results of  $xyz$ -polarization indicated that majority of the spins lies in the  $ab$ -plane. For the first time CO superstructure reflection was observed at  $(\bar{2} \ \bar{2} \ \frac{3}{2})_t$  position, which indicates the doubling of the  $c$ -axis. The observation of diffuse scattering around the magnetic Bragg reflection indicated the presence of short range spin correlations in the system. Observed frequency dependent ac-susceptibility and the presence of memory effect from magnetization indicated the presence of glassy state below  $\sim 60$  K in the system.

# Zusammenfassung

In dieser Dissertation beschreibe ich Untersuchungen von zwei Eisen-Oxid Materialien:

## **(1) Eine detaillierte Untersuchung von Ferroelektrizität in Magnetit ( $\text{Fe}_3\text{O}_4$ )**

Multiferroika, die ferroelektrische und ferromagnetische Phasen vereinen, sind von grossem wissenschaftlichem und technischem Interesse, aufgrund der möglichen magnetoelektrischen Kopplung zwischen den Phasen. Solche Materialien sind selten, da konventionelle Ferroelektrizität eine leere d-Schale bedingt, was die Präsenz von Magnetismus ausschliesst. Unter mehreren unkonventionellen Mechanismen, die zu Ferroelektrizität führen, ist Ladungsordnung (CO) besonders interessant im Hinblick auf mögliche Anwendungen. Experimentell verifizierte Beispiele sind jedoch zurzeit sehr selten. Der Verwey Übergang bei  $T_V = 120$  K in Magnetit, entdeckt in 1939, ist das klassische Beispiel von Ladungsordnung. Trotz Kontroversen über die Existenz von Ladungsordnung, wurde Magnetit als ein Multiferroikum basierend auf Ladungsordnung vorgeschlagen. Obschon es bereits Hinweise auf z.B. einen magnetoelektrischen Effekt aus frühen Untersuchungen gab, war der damalige Fokus auf die komplexe Kristallstruktur im ladungsgeordneten Zustand gerichtet, nicht auf mögliche Multiferroizität. Um die ferroelektrischen Eigenschaften von Magnetit mit dielektrischer Spektroskopie zu untersuchen, wurde am Institut eine entsprechende Messapparatur erstellt. Nach einer Einleitung und der Beschreibung der verwendeten experimentellen Techniken, beginnt diese Dissertation mit der Vorstellung unseres neuen dielektrischen Setups und den damit durchgeführten Testexperimenten.

Der Verwey-Übergang hängt sehr sensitiv von der genauen Sauerstoff-Stöchiometrie der Proben ab. Diese wurde während der Synthese gesteuert durch passende Mischungen von  $\text{CO}_2$  und entweder CO oder  $\text{Ar}(\text{H}_2)_{4\%}$ . Ich untersuchte zunächst die passenden Verhältnisse von  $\text{CO}_2/\text{Ar}(\text{H}_2)_{4\%}$  bei hohen Temperaturen in polykristallinen Proben. Der Verwey Übergang wurde dabei hauptsächlich über thermo-remanente Magnetisierung und spezifische Wärme charakterisiert. Die Ergebnisse wurden dann zur Zucht von Kristallen optimierter Qualität in einem Spiegelofen verwendet. Vorgeschlagene Relaxor-Ferroelektrizität in Magnetit wurde mit diffusen Streuexperimenten (Neutronen und Hochenergie-Röntgen) untersucht. Diffuse Streuung wurde mit Neutronen beobachtet, nicht jedoch mit Röntgenstrahlung, was auf einen magnetischen Ursprung schliessen lässt. Zum ersten Mal wurde eine zeitaufgelöste Röntgenbeugungstechnik implementiert, um die Schaltbarkeit einer polaren Struktur mittels eines elektrischen Feldes zu untersuchen, hier an Magnetit. Die beobachtete Intensitätsänderung eines Bragg-Reflexes impliziert die Schaltung zwischen zwei Strukturen, welche durch Inversionssymmetrie miteinander verbunden sind. Dies stellt den ersten mikroskopischen Beweis von ferroelektrischem

Schalten in Magnetit dar.

## **(2) Untersuchung verschiedener physikalischer Eigenschaften von Sauerstoff-defizientem Strontium Ferrit ( $\text{SrFeO}_{3-\delta}$ )**

“Colossal magnetoresistance”, d.h. die enorme Änderung im elektrischen Widerstand durch das Anlegen eines magnetischen Feldes ist ein Schlüssel zu einer möglichen nächsten Generation von magnetischen Speicherelementen. Sauerstoff-defizitäres Strontium-Ferrit ( $\text{SrFeO}_{3-\delta}$ ,  $\delta=0\text{--}0.5$ ) erfährt verschiedene Typen von Magnetowiderstands-Phänomenen, abhängig von der Präsenz verschiedener magnetischer Phasen. Sauerstoff-defiziente  $\text{SrFeO}_{3-\delta}$  Kristalle mit  $\delta=0.27$  und  $\delta = 0.35$  (gemäß Infrarot-Absorptions-Spektroskopie) wurden mittels Spiegelofen gezüchtet. Diese oxidischen Systeme enthalten eine Mischung von Eisen Ionen in tetravalenten und trivalenten Zuständen. Anomalien bei  $\sim 70$  K,  $\sim 230$  K, und  $\sim 130$  K, beobachtet in Magnetisierungsmessungen, deuten auf die Präsenz von tetragonalen, orthorhombischen, und kubischen Phasen hin. Die Präsenz dieser Phasen wurde durch zusätzliche mikroskopische Messungen mittels Neutronenstreuung bestätigt. Zwei bisher unbekannte magnetische Phasen mit Propagationsvektoren  $\mathbf{k} = (0.25\ 0.25\ 0.25)_c$  und  $(0.25\ 0\ 0.25)_c$  wurden beobachtet, mit detaillierter Polarisationsanalyse. Resultate der xyz-Polarisationsanalyse deuten darauf hin, dass die Spins hauptsächlich in der ab-Ebene liegen. Zum ersten Mal wurde ein Ladungsordnungs-Überstruktur-Reflex beobachtet, bei  $(\bar{2}\ \bar{2}\ \frac{3}{2})_t$ , was eine Verdopplung der c-Achse impliziert. Die beobachtete Frequenzabhängigkeit der ac Suszeptibilität und das Auftreten eines “Gedächtnis-Effekts” in der temperaturabhängigen Magnetisierung deuten auf die Präsenz eines Glas-Zustands unterhalb von  $\sim 60$  K hin.

# Contents

<b>1</b>	<b>Strongly correlated electronic system</b>	<b>1</b>
1.1	Complex ordering phenomena . . . . .	2
1.1.1	Charge order . . . . .	2
1.1.2	Orbital order . . . . .	3
1.1.3	Spin order . . . . .	5
1.2	Complex transition metal oxides: Novel phenomena . . . . .	7
1.2.1	Colossal magnetoresistance (CMR) effect . . . . .	7
1.2.2	Multiferroics . . . . .	10
<b>2</b>	<b>Experimental methods and theoretical background</b>	<b>17</b>
2.1	Synthesis of polycrystalline powders and growth of single crystals . . . .	18
2.1.1	Solid state reaction route . . . . .	18
2.1.2	Crystal growth by optical floating zone technique . . . . .	19
2.2	Magnetic properties . . . . .	20
2.2.1	AC and DC magnetization measurements . . . . .	20
2.3	Thermal properties . . . . .	24
2.3.1	Specific heat . . . . .	24
2.4	Scattering theory . . . . .	25
2.4.1	Basics of diffraction . . . . .	25
2.4.2	Bragg's law . . . . .	26
2.4.3	Reciprocal lattice and Ewald construction . . . . .	27
2.4.4	Diffraction from a crystal . . . . .	28
2.5	X-ray diffraction . . . . .	29
2.5.1	Laue method . . . . .	30
2.5.2	Powder X-ray diffraction . . . . .	31
2.5.3	Beamline P09 at PETRA III . . . . .	31
2.5.4	Beamline 6-ID-D at APS . . . . .	33
2.6	Neutron scattering . . . . .	34
2.6.1	Nuclear scattering . . . . .	34
2.6.2	Magnetic scattering . . . . .	35

2.6.3	Polarization analysis . . . . .	37
2.6.4	DNS instrument at MLZ . . . . .	38
2.6.5	SPODI at MLZ . . . . .	39
<b>3</b>	<b>New dielectric spectroscopy setup</b>	<b>41</b>
3.1	Dielectric response . . . . .	42
3.1.1	Interfacial or space charge polarization . . . . .	45
3.1.2	Dielectric mechanism . . . . .	45
3.2	Experimental setup . . . . .	47
3.3	Test measurements . . . . .	49
<b>4</b>	<b>Magnetite: crystal growth, macroscopic characterization and low temperature diffuse scattering studies</b>	<b>53</b>
4.1	Magnetite . . . . .	55
4.1.1	Verwey transition and the complex charge ordering . . . . .	56
4.1.2	History of ferroelectricity in Magnetite . . . . .	59
4.2	Synthesis and effect of non-stoichiometry on the Verwey transition . . . . .	62
4.2.1	High quality polycrystalline precursor synthesis for the crystal growth	63
4.2.2	High quality single crystal growth . . . . .	65
4.3	Diffuse scattering study on relaxor ferroelectric Magnetite . . . . .	67
4.4	Discussion . . . . .	71
<b>5</b>	<b>Time resolved experiment to test the ferroelectricity by switching the polar structure of magnetite</b>	<b>73</b>
5.1	Introduction . . . . .	74
5.2	Preliminary characterization . . . . .	78
5.2.1	Simulation . . . . .	78
5.2.2	Sample characterization . . . . .	79
5.3	Experiment . . . . .	81
5.4	Results and discussion . . . . .	84
5.5	Conclusions . . . . .	87
<b>6</b>	<b>Growth, characterization and neutron polarization analysis on <math>\text{SrFeO}_{3-\delta}</math> single crystal</b>	<b>89</b>
6.1	Introduction . . . . .	90
6.2	Synthesis and single crystal growth . . . . .	95
6.3	Crystal structure . . . . .	97
6.3.1	$\text{SrFeO}_{3-\delta}$ , $\delta \sim 0.27 \pm 0.04$ . . . . .	97
6.3.2	$\text{SrFeO}_{3-\delta}$ , $\delta \sim 0.35 \pm 0.03$ . . . . .	104
6.4	Macroscopic magnetic properties . . . . .	105

6.4.1	SrFeO <sub>3-<math>\delta</math></sub> ( $\delta \sim 0.27 \pm 0.04$ )	105
6.4.2	SrFeO <sub>3-<math>\delta</math></sub> ( $\delta \sim 0.35 \pm 0.03$ )	109
6.5	Neutron diffraction with $xyz$ -polarization analysis	112
6.5.1	Results SrFeO <sub>3-<math>\delta</math></sub> ( $\delta \sim 0.27 \pm 0.04$ )	114
6.5.2	Results SrFeO <sub>3-<math>\delta</math></sub> ( $\delta \sim 0.35 \pm 0.03$ ):	120
6.6	Summary	121
<b>7</b>	<b>Summary and Outlook</b>	<b>125</b>
	<b>Bibliography</b>	<b>131</b>
	<b>Acknowledgements</b>	





# Chapter 1

## Strongly correlated electronic system

Materials with strong electronic correlations can exhibit unusual and exciting low temperature electronic and magnetic properties ranging from metal-insulator transition [1–3], superconductivity [4, 5], multiferroics [6, 7], colossal magnetoresistance (CMR) effect [8, 9] and to heavy-fermion effect [10]. Understanding the physics behind these massive number of interesting phenomena in the complex transition metal oxides is the focus of intense research and debate in condensed matter science as these mechanisms cannot be explained within the standard model of solid state physics. For example the mechanism of high- $T_c$  superconductor, which is still under debate even after twenty five years. The reasons for the whole zoo of these exciting phenomena are the coulomb interaction between the electrons in the transition metal oxides and the resulting the strong interplay among the spin, charge, orbital and lattice degrees of freedom. These novel functionalities cause correlated electron systems to have high potential for technological applications for e.g., in superconducting magnets, magnetic storage and many more. Understanding the mechanism and interplay between these competing degrees of freedom is crucial for the novel applications.

## 1.1 Complex ordering phenomena

### 1.1.1 Charge order

Charge ordering (CO) is often observed in strongly correlated materials such as transition metal oxides or organic conductors with mixed valence state. As the term CO says it is the ordering of valence state of ions in a crystal from high temperature homogeneous intermediate valence state to a low temperature ordered-mixed valence state. CO is associated with a structural phase transition with a lowering of the symmetry, because of the long range ordering in which sites the electrons localizes. Though the charge order was first proposed by Eugene Wigner 1930, this concept and the associated phenomena were first observed in magnetite ( $\text{Fe}_3\text{O}_4$ ) by Verwey in 1934 (for details, see chapter 4). Later it has been observed in mixed-valence pervoskites, e.g., doped manganites ( $\text{A}_{1-x}\text{B}_x\text{MnO}_3$ : the ratio  $\text{Mn}^{3+}/\text{Mn}^{4+}$  depends on the doping level) [11], rare earth nickelates ( $\text{RNiO}_3$ :  $\text{Ni}^{3+} \rightarrow \text{Ni}^{3+\delta}/\text{Ni}^{3-\delta}$ ) [12, 13], in self-doped  $\text{NaV}_2\text{O}_5$  ( $\text{V}^{4+}/\text{V}^{5+}$ ) [14],  $\text{SrFeO}_3$  ( $\text{Fe}^{3+}/\text{Fe}^{5+}$ ) and  $\text{SrFeO}_{3-\delta}$  ( $\text{Fe}^{3+}/\text{Fe}^{4+}$ ) [15],  $\text{RFe}_2\text{O}_4$  ( $\text{Fe}^{2+}/\text{Fe}^{3+}$ ) [16],  $\text{Fe}_2\text{OBO}_3$

(Fe<sup>2+</sup>/Fe<sup>3+</sup>) [17] etc. Charge ordering induces an electric polarization whenever it breaks the spacial inversion symmetry. The types of charge ordering and its related novel phenomena, that are relevant to the present work are discussed in the section 1.2. CO can alter the lattice periodicity as it is always accompanied by a slight lattice distortion. Hence the observation of the charge ordering is possible. There are different methods to detect the CO phenomena. Few of them are: An empirical method, Bond Valence Sum (BVS) calculation [18, 19] through properly determined crystallographic bond lengths. The valence  $V$  can be calculated by the formula:

$$V = \sum \exp \frac{(R_0 - R_i)}{b}$$

Where  $R_i$  is the observed bond length,  $R_0$  is a tabulated parameter expressing the (ideal) bond length of the cation-anion pair and  $b$  is an empirical constant (0.37 Å).

Another method which has been widely used to study the CO is Resonance x-ray scattering [20]. The energy value of the absorption edge, also known as chemical shift for the different valences are slight different. Hence by tuning the incident x-ray energies near the absorption edge, the contrast between the atomic scattering factors for the different valence states can be significantly enhanced. The technique of Mossbauer spectroscopy is widely used to distinguish ions with different valence states by measuring the isomer shift [21]. However, it cannot determine the charge ordering, i.e. the spatial arrangement of different valence states.

#### 1.1.2 Orbital order

The orbital degrees of freedom often plays a crucial role in the physics of strongly correlated 3d transition metal oxides for e.g., metal-insulator transition, colossal magnetoresistance etc. In order to understand these phenomena first we discuss the basic interactions which are necessary to understand the orbital ordering.

##### 1.1.2.1 Crystal field effect

Crystal field theory has the basis on the basic principle of breaking of degeneracy of the d- orbitals due to Stark effect. d- orbitals are having their lobes that is the regions of highest electron density either along the axis of the orbitals or at 45 degree angle to the

axis. In case of a octahedral complex, the 3d level split in to doubly degenerate upper level,  $e_g$  ( $d_{z^2}$ ,  $d_{x^2-y^2}$ ) and triply degenerate lower level,  $t_{2g}$  ( $d_{xy}$ ,  $d_{yz}$ ,  $d_{zx}$ ), see fig 1.1. The difference between the energy of  $e_g$  and  $t_{2g}$  for an octahedral crystal field is called  $\Delta_o$ . But in case of a tetrahedral complex, the lower level is doubly degenerate and upper level is triply degenerate. The total crystal field splitting of tetrahedral crystals is called  $\Delta_t$ . In weak crystal field the energy associated with the first Hunds rule leads to a high spin states and when crystal field is stronger and it prefers to stay in the splitted low energy orbitals and a low spin state is found. Crystal field splitting energy depends upon the strength of the approaching crystal field. Different shapes of the d-orbitals and the level schemes of the 3d orbitals in an octahedral and in tetrahedral arrangement is shown the figure 1.1.

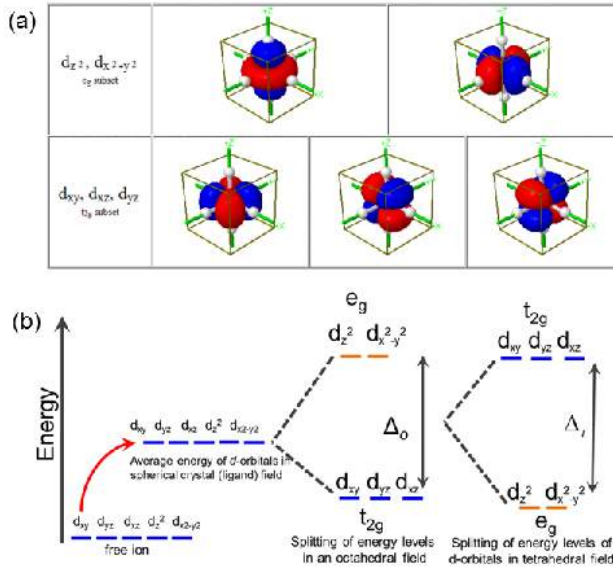


Figure 1.1: (a) Shapes of the d-orbitals, taken from reference [22]. (b) Crystal field effect: d-orbitals in the presence of octahedral and tetrahedral field

### 1.1.2.2 Jahn-Teller effect

The original statement of Jahn-Teller (JT) theorem [23] is as follows: *Any non-linear molecular system in a degenerate electronic state will be unstable and will undergo distortion to form a system of lower symmetry and lower energy thereby removing the*

*degeneracy*. If the two orbital of  $e_g$  level have unsymmetrical distribution of electrons, this will leads to either of shortening or elongation of the bonds. This breaks the degeneracy of the  $e_g$  orbitals i.e. the  $e_g$  orbitals will again split with different energies for  $e_g$  and  $t_{2g}$  orbitals. If the crystal field is same then the inversion center of the orbitals are retained. Similar but small and more complex effect can be observed in case of unsymmetrical electron distributions in the  $t_{2g}$  orbitals also.

For example in the case of  $\text{LaMnO}_3$ ,  $\text{Mn}^{3+}$  has a  $d^4$  configuration. According to first Hund's rule, all the spins are aligned parallel resulting in total spin of  $S = 1/2$  and the configuration is  $t_{2g}^3 e_g^1$ .  $\text{Mn}^{3+}$  is Jahn-teller active. Hence the oxygen octahedron is distorted. As a result the degeneracy of the  $e_g$  orbitals is removed, shown in the figure 1.2. This leads to a long range orbital ordering of  $e_g$  electrons. Charge order determines what orbital order is possible and this couples charge, orbital and spin order together.

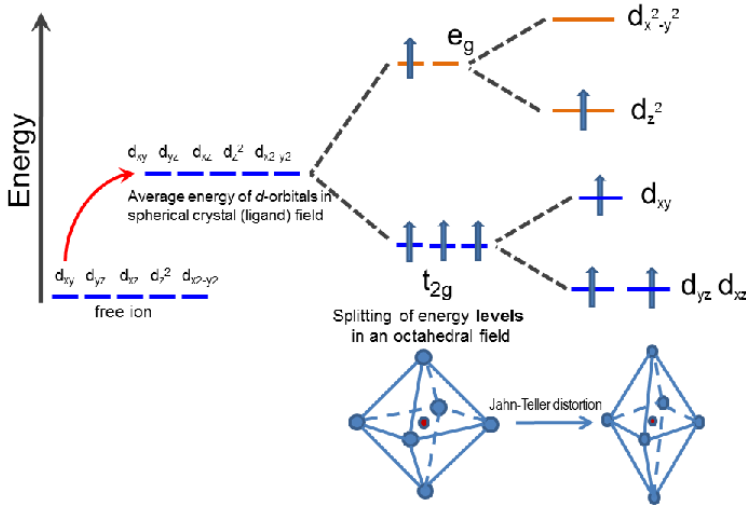


Figure 1.2: Jahn-teller splitting: The oxygen ions surrounding the  $\text{Mn}^{3+}$  is slightly distorted and the degeneracy of the  $e_g$  is remove

### 1.1.3 Spin order

The strong exchange interaction between the spins of neighboring magnetic ions leads to magnetic or spin order in a system. Good description of the interaction between the neighboring spins  $S_i$  and  $S_j$  are given by Heisenberg, within framework of model

Hamiltonian [24]:

$$H = \sum_{ij} -J_{ij} \vec{S}_i \vec{S}_j \quad (1.1)$$

Where  $J_{ij}$  is the exchange constant between the  $i^{th}$  and  $j^{th}$  spins, which describe the nature of the spins.  $J > 0$  favors parallel alignment of the neighboring spins, hence the system is ferromagnetic.  $J < 0$  favors antiparallel alignment of the spins, hence the system is antiferromagnetic. In case of ferromagnetic order the periodicity is equal to the separation of the magnetic moments. But in case of antiferromagnetic order the repeat period is doubled, which can lead to different types of magnetic structures. For example, commensurate antiferromagnetic order, where the period of the magnetic order is equal to an integer number of lattice units (A-type, G-type, C-type and E-type [see fig 1.3]).

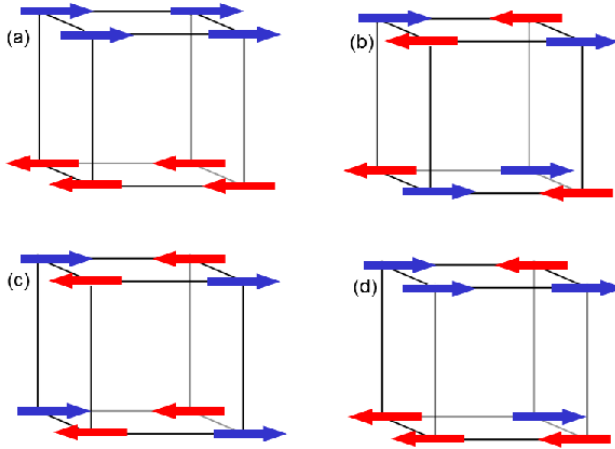


Figure 1.3: Different types of commensurate antiferromagnetic ordering: (a) A-type, (b) G-type, (c) C-type, (d) E-type.

Competitive neighbor and next nearest neighbor ferro and antiferromagnetic exchange or relatively more complex anisotropic exchange interaction can lead to incommensurate antiferromagnetic order where, the period of the magnetic order is not equal to an integer number number of lattice units (e.g., sinusoidal modulated spin density waves and spiral order). In the later case the spins will change their orientation by a fixed angle relative to their neighbors along the propagation direction. This can be determined macroscopically for e.g., by measuring the net magnetization in different crystallographic directions or microscopically by neutron polarization analysis in different orientations ( $hhl$ -plane,

$h0l$ -plane or  $00l$ -etc). Schematic representation of the charge spin and orbital ordering is shown in the figure 1.4.

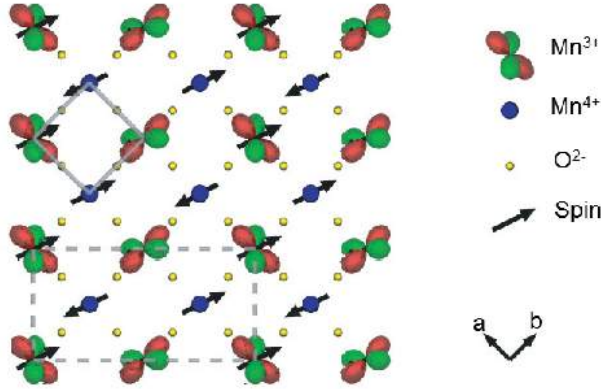


Figure 1.4: Schematic representation of charge, spin and orbital ordering in a doped manganite system, taken from reference [25].

## 1.2 Complex transition metal oxides: Novel phenomena

### 1.2.1 Colossal magnetoresistance (CMR) effect

Magnetoresistance (MR), the change in the resistivity of a material with the application of a magnetic field is well know phenomenon in all metals and semiconductors [26]. Most of these materials have gained much attention in a rapid development of our new technologies for e. g., in magnetic sensors, improved memory devices etc. However the effect of MR in conventional materials are very small and those which shows large MR effect are called Giant magneto resistance (GMR) or colossal magnetoresistance (CMR) materials. The first discovery of GMR effect in magnetic multilayers, Fe/Cr/Fe, by Peter Grünberg and Allbert Fert in 1988 [27, 28], honored by Nobel Prize in Physics in 2007. The term GMR generally associated with the certain metallic multilayers and the applications of them are already in the commercial products, for e.g., in read-heads of magnetic disks. The discovery of GMR effect in magnetic multilayers lead to the investigation of similar effects on bulk magnetic systems and were succeeded in discovering CMR effect. In CMR



materials, the change in resistivity with an applied magnetic field can be several orders of magnitude higher than for GMR. The effect of CMR is well studied in manganese-based perovskite oxides,  $R_{1-x}A_x\text{MnO}_3$  ( $R$  = rare earth: La, Pr, Sm etc and  $A$  = alkaline earth : Ca, Sr, Ba, Pb). The magnitude of CMR typically defined as the ratio of

$$MR = \Delta\rho/\rho_0 = [\rho(T, H) - \rho(T, 0)]/\rho(T, 0)$$

where  $\rho$ ,  $T$  and  $H$  are the resistivity, temperature and applied magnetic field respectively. The origin of the CMR effect is closely related to strong mutual coupling of spin, lattice, charge and orbital degrees of freedom involving charge ordering, Jahn-teller effect, double exchange interaction and electronic phase separation. The first observation of the CMR effect was in 1994 on  $\text{La}_{0.67}\text{Ca}_{0.33}\text{MnO}_3$  thin film [29]. MR ratio in this material was close to 100 % near 77 K and with 6 T field. Later the studies have extended to other hole doped manganites, for e.g.,  $\text{Pr}_{1-x}\text{Ca}_x\text{MnO}_3$ ,  $\text{Nd}_{1-x}\text{Sr}_x\text{MnO}_3$  etc. The ground state of parent compounds e.g.,  $\text{LaMnO}_3$  and  $\text{CaMnO}_3$  are A type and G type antiferromagnetic (AFM) respectively. In A-type AFM the inter-plane coupling is antiferromagnetic and intra-plane coupling is ferromagnetic. Whereas in G-type AFM both inter and intra-plane coupling are AFM. But when you dope the both, the spins will cant and induces both ferromagnetism and conduction. The mechanism leading to antiferromagnetic and ferromagnetic state is discussed below.

#### 1.2.1.1 Superexchange interaction

Here the superexchange interaction is an indirect magnetic interaction i.e., the interaction between two Mn(magnetic ion) ions via oxygen ion (non-magnetic). The Anderson-Goodenough-Kanamori rules [30, 31] determine whether the coupling is ferromagnetic or antiferromagnetic. If the Mn-O-Mn bond angle is 180 degree with half filled d-shell for both magnetic ions, then the resulting structure is antiferromagnetic. When the angle is 90 degree then it is ferromagnetic (FM). The schematic picture of the exchange interaction is shown in the figure 1.5.

#### 1.2.1.2 Double exchange interaction

The ferromagnetic ground state and the conductivity in the mixed valence manganese system was explained by Zener in 1951 [32]. According to him the two  $e_g$  electrons

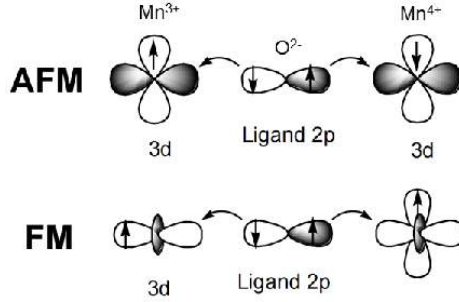


Figure 1.5: Two Mn atoms are separated by oxygen atom: superexchange interaction leading to antiferromagnetic and ferromagnetic ground state

between the Mn<sup>4+</sup> and Mn<sup>3+</sup> can transfer simultaneously i.e., one from O<sup>2-</sup> to Mn<sup>4+</sup> and one from Mn<sup>4+</sup> to O<sup>2-</sup> and during these transfers the electron will keep its spin direction. It is crucial for double exchange to follow first Hunds rule preferring parallel arrangements of spins. Since double exchange involves real hopping of  $e_g$  electrons, it links to ferromagnetism with conductivity. The double exchange mechanism is shown in the figure 1.6.

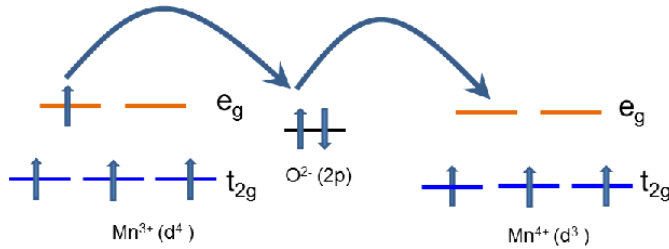


Figure 1.6: Double exchange mechanism in a mixed valence manganite proposed by Zener

In perovskite materials CMR generally occurs close to the Curie temperature when the spins are tending to line up. Application of magnetic field at this stage helps in aligning neighboring spins hence the hopping between Mn<sup>3+</sup> to Mn<sup>4+</sup> will be favored (DE interaction). Though the qualitative description of the CMR effect done by considering the DE mechanism origin from Hund's coupling between the  $e_g$  and  $t_{2g}$  electrons and the Jahn-teller distortion: altering the Mn-O-Mn bond angle affecting the electron hopping probability and the DE interaction, due to orbital degeneracy of the  $e_g$  state however, unable to explain it quantitatively. The CMR effect is also closely related to the real space

charge ordering [33–36], Jahn-teller polarons [37, 38], field-induced structural phase transitions [39] etc. For example in case of La-based manganite systems the CMR effect is also associated with the charge-lattice and spin-lattice couplings which is unable to explained by DE mechanism alone.

Besides manganites, the CMR- effect also has been studied in ferrite system for example in  $\text{Sr}_2\text{FeMoO}_6$ ,  $\text{SrFe}_{1-x}\text{Co}_x\text{O}_3$  etc [40–42]. In the present thesis we have studied one of those systems,  $\text{SrFeO}_{3-\delta}$ , where  $\text{Fe}^{3+}$  perovskite form a Ruddlesden-Popper series of lattice structures similar to the manganites system. Here the high spin  $\text{Fe}^{4+}$  ion is equivalent to Jahn-teller active  $\text{Mn}^{3+}$  ion of manganites [43]. Further discussion and the motivation for the work is discussed in chapter 6.

## 1.2.2 Multiferroics

In the search of materials for the novel devices with multiple degrees of control, an interesting class of multi-functional materials, known as multiferroics emerged as a potential candidate. Multiferroics are generally defined as single phase materials, which simultaneously exhibits more than one of the following primary ferroic order parameter: ferromagnetism, ferroelectricity and ferroelasticity [44]. The mutual coupling between these properties are shown in the figure 1.7. Today the definition of multiferroics extended to other long-range orders, such as antiferromagnetism combined with ferroelectricity.

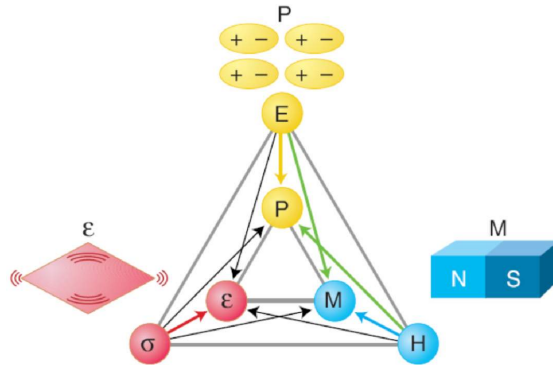


Figure 1.7: The mutual coupling between the ferroelectricity (electric field  $E$  controls polarization  $P$ ), magnetism (magnetic field  $H$  controls magnetization  $M$ ), and ferroelasticity (stress  $\sigma$  controls strain  $\epsilon$ ), taken from reference [45].

### 1.2.2.1 Magnetoelctric multiferroics

With the rapid growth of information technology, the demand for production of storage media with higher data density also increased. Indeed the functional electronic and magnetic materials are already in the use of important technological application, such as ferroelectrics in random access memory (Fe-RAM), ferromagnets in hard drives. But the current trend towards miniaturization technology leads the scientific community in search of multifunctional materials, which exhibit both ferroelectricity and ferromagnetism in a single phase, known as magnetoelectric multiferroics. In these materials, in principle, the induced polarization can be controlled by a magnetic field and the magnetization by an electric field, which is known as magnetoelectric effect. It is also important to note that not all multiferroics are magnetoelectrics (e.g., hexagonal YMnO<sub>3</sub> : magnetoelectric effect is forbidden by symmetry) and not all magnetoelectrics are multiferroics (e.g., Cr<sub>2</sub>O<sub>3</sub> : no electric ordering). The presence cross coupling between these two order parameter, in principle, can be conveniently used for e.g., in the four-state memory devices [46].

The magnetoelectric (ME) effect was first postulated by Pierre Curie in nineteenth century by discussing the symmetry constraints required for strong coupling between the ferroelectric and ferromagnetic degrees of freedom [47]. The linear ME effect was first predicted in Cr<sub>2</sub>O<sub>3</sub> by Dzyaloshinskii in 1959 [48] and was experimentally observed in this material by Astrov in 1960 [49]. They found that both time and spatial symmetry need to be broken simultaneously while combining the symmetry operation [figure 1.8]. Materials exhibiting Linear magnetoelectric effect have long-range magnetic ordering, but no spontaneous polarization. However, in these materials the polarization can be induced by applied magnetic field. ME effect in non-ferroic materials can be described by Landau theory by writing the general free energy (F) equation in terms of both electric  $\vec{E}$  and magnetic field  $\vec{H}$ . Using Einstein summation, F can be written as:

$$F(\vec{E}, \vec{H}) = F_0 - P_i^s E_i - M_i^s H_i - \frac{1}{2} \varepsilon_{ij} E_i E_j - \frac{1}{2} \mu_{ij} H_i H_j - \alpha_{ij} E_i H_j - \frac{1}{2} \beta_{ijk} E_i H_j H_k - \frac{1}{2} \gamma_{ijk} H_i E_j E_k - \dots, \quad (1.2)$$

Here,  $F_0$  is the part of the free energy not associated with magnetic or electric effects and subscripts  $(i, j, k)$  refer to the three components of a variable in spatial coordinates.  $P^s$  and  $M^s$  are the components of spontaneous polarization and magnetization, which is zero for non-ferroic materials.  $\varepsilon_0$  and  $\mu_0$  are the dielectric and magnetic

susceptibilities. The tensor  $\alpha_{ij}$  describes the linear magnetoelectric coupling.  $\varepsilon_{ij}$  and  $\mu_{ij}$  are the tensors describing linear magnetic and electric susceptibilities. The third rank tensors  $\beta_{ijk}$  and  $\gamma_{ijk}$  describe the higher order magnetoelectric couplings [7]. Later by minimizing the free energy both polarization and magnetization can be calculated.

$$P_i(E, H) = \frac{\partial F}{\partial E_i} = P_i^s + \varepsilon_{ij} E_j + \alpha_{ij} H_j + \frac{1}{2} \beta_{ijk} H_j H_k + \gamma_{ijk} H_i E_j + \dots, \quad (1.3)$$

$$M_i(E, H) = -\frac{\partial F}{\partial H_i} = M_i^s + \mu_{ij} H_j + \alpha_{ij} E_j + \beta_{ijk} H_j E_i + \frac{1}{2} \gamma_{ijk} E_j E_k + \dots, \quad (1.4)$$

Although the magnetoelectric effect was observed way back in 1960's in  $\text{Cr}_2\text{O}_3$  and other antiferromagnetic crystals [50], the coupling between the order parameter is very weak for any practical application. That means  $\alpha_{ij}$  always smaller than geometric means of electric and magnetic permeability [51]:  $\alpha_{ij}^2 < \chi_{ii}^e \chi_{jj}^m$ . In order to achieve a large coupling both electric and magnetic permeability should be large, as is naturally the case for ferromagnets and ferroelectrics.

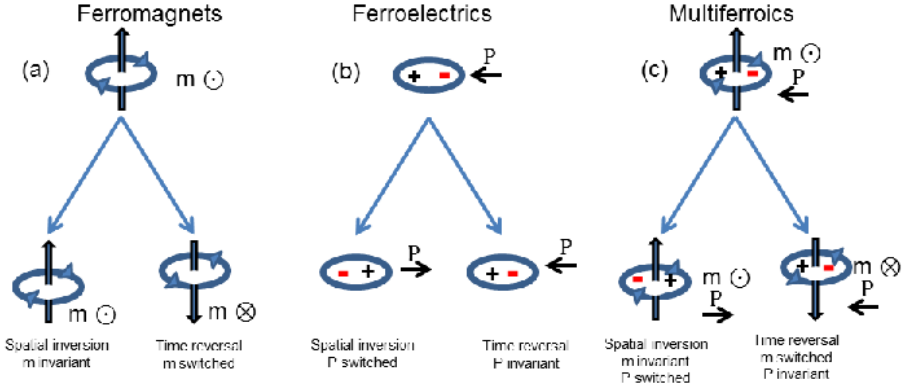


Figure 1.8: (a) Broken time reversal symmetry in the case of ferromagnets(antiferromagnetics): change of sign of the magnetic moment under the symmetry operation,  $M(-t) = -M$ , whereas spacial inversion symmetry is invariant. (b) Broken space inversion symmetry in the case of ferroelectrics: symmetry operation  $P(-x) = -P$ , whereas time reversal symmetry is invariant. (c) In the case of multiferroics, both the time and space inversion symmetry need to be broken simultaneously.

### 1.2.2.2 Classification of magnetoelectric multiferroics

By sticking to the strict definition of multiferroics, it is very difficult to find these materials. Because the mechanisms driving ferroelectricity and ferromagnetism are generally incompatible as conventional ferroelectricity involves an empty d-shell, preventing the presence of magnetism. A classical example of a conventional ferroelectric material is  $\text{BaTiO}_3$ . In this material the polar state emerges due to a structural instability, which caused by cooperative shifting of the  $\text{Ti}^{4+}$  cation along the [111] direction; this off-centering is stabilized by covalent bonding between the oxygen 2p orbitals and the empty d-shell of  $\text{Ti}^{4+}$  [52]. On the other hand, ferromagnetism usually requires a transition metal with a partially filled d-shell. Therefore, alternative mechanisms are required to combine these two properties. Depending on the mechanism driving ferroelectricity, the materials can be divided into two categories: proper ferroelectric and improper ferroelectrics. For example,  $\text{BiFeO}_3$  fall in to the category of proper multiferroics due to their similarity with conventional ferroelectric materials. In these materials the ferroelectricity is induced by stereochemical activity of  $\text{Bi}^{3+}$  “lone-pairs”. The two lone pair 6s electrons do not participate in chemical bonding, rather they move away from the centrosymmetric position of the cation with respect to the middle of the oxygen cage [53]. In these materials the value of the spontaneous polarization is of the order of  $10\text{-}100\mu\text{ C/cm}^2$  and ferroelectric state can be achieved at higher temperature. But the coupling between order parameter is relatively weak because the FM and FE are induced by different ions. Different types of ferroelectric are tabulated in the table 1.1.

In improper multiferroics, the ferroelectricity is induced by different types of ordering. For example in hexagonal manganites,  $\text{h-RMnO}_3$  ( $\text{R}$  = rare earth) ferroelectricity is induced by the rotation of  $\text{MnO}_5$  polyhedra, that favors a closer packing of the structure. This results in the oxygen ions moving closer to the rare-earth site, leading to the formation of an electric dipole as a secondary order parameter [55]. This is known as geometrically driven multiferroicity. In case of orthorhombic- $\text{RMnO}_3$  for e.g.,  $\text{TbMnO}_3$ , the electric polarization is induced by cycloidal antiferromagnetic ordering [56]. Microscopic mechanism for ferroelectricity in this class of systems can include inverse Dzyaloshinskii-Moriya interaction, electric current cancellation model and spin current model [57–60]. Another new class of system is ferroelectricity driven by symmetric exchange striction. In  $\text{Ca}_3\text{CoMnO}_6$  the ferroelectricity is induced by the combination

Table 1.1: Classification of ferroelectrics, taken from reference [54]

	<b>Mechanism of inversion symmetry breaking</b>	<b>Materials</b>
Proper	covalent bonding between 3d <sup>0</sup> transition metal (Ti) and oxygen	BaTiO <sub>3</sub>
	polarizability of 6s <sup>2</sup> lone pair	BiMnO <sub>3</sub> , BiFeO <sub>3</sub>
Improper	structural transition 'Geometric ferroelectrics'	K <sub>2</sub> SeO <sub>4</sub> , Cs <sub>2</sub> CdCl <sub>4</sub> h-RMnO <sub>3</sub>
	charge ordering 'Electronic ferroelectrics'	<span style="border: 1px solid blue; padding: 2px;">LuFe<sub>2</sub>O<sub>4</sub></span> , Fe <sub>3</sub> O <sub>4</sub> ?
	magnetic ordering 'Magnetic ferroelectrics'	o-RMnO <sub>3</sub> , RMn <sub>2</sub> O <sub>6</sub> , CoCr <sub>2</sub> O <sub>4</sub> , MnWO <sub>4</sub>

of both, using spin magnet of the up-up-down-down type magnetic order and the nonequivalence of Mn<sup>4+</sup> and Co<sup>2+</sup> ions [54, 61]. Though the magnetoelectric coupling is intrinsically strong in these spin driven ferroelectrics the achievable polarization is very small, of the order of 10<sup>-2</sup>  $\mu\text{Ccm}^{-2}$  also, their ordering temperatures are very low.

### 1.2.2.3 Multiferroicity due to charge ordering

As discussed in the previous section, magnetoelectric multiferroics are of high interest for potential information technology. But for practical applications we need materials which show both, the strong magnetoelectric coupling as well as a high magnitude of electric polarization and at room temperature. Finding such a material is a great challenge. In this respect ferroelectricity originating from charge ordering that is coupled to spin ordering yielding a multiferroic phenomena is highly relevant application in information technology: because of the large achievable polarization [62] and strong magnetoelectric coupling due to presence of both charge and spin degrees of freedom on the same ion. Such materials are rare however. Though the CO-based ferroelectricity was predicted in hole doped manganites Pr<sub>1-x</sub>Ca<sub>x</sub>MnO<sub>3</sub> (x = 0.4 and 0.5), due to the intermediate state between site and bond-center [63]. Experimental proof is elusive due to rather high electrical conductivity. Thus the presence of ferroelectricity in such a high conducting material is questionable. Another material often considered as an example this type of

system is quasi-one-dimensional organic charge transfer salt [64]. Among the very few materials exhibiting CO-based ferroelectricity, the well cited example and most promising candidate material was  $\text{LuFe}_2\text{O}_4$  since discovery of charge order in it in 2005 [65]. The charge ordering temperature is at  $\sim 320$  K and ferrimagnetic ordering is at  $\sim 240$  K. It has a bilayer structure with iron lying on a triangular lattice within each layer. The  $\text{Fe}^{2+}$  and  $\text{Fe}^{3+}$  charge order in this bilayer is frustrated which leads to the formation of charged planes. The average valence of Fe is +2.5. It was proposed that the net polarization is induced by the charge transfer between the alternating triangular layer with the 2:1 and 1:2 ratio of  $\text{Fe}^{2+}$  and  $\text{Fe}^{3+}$  ions fig 1.9.

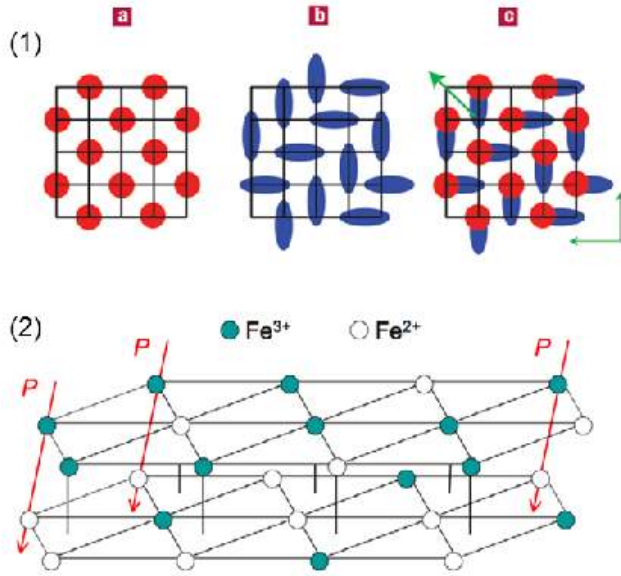


Figure 1.9: Schematic diagram of (1) (a) site-centered and (b) bond-centered charge order (b) intermediate ferroelectric state (lack of inversion symmetry) due to the presence of both site and bond centered charge order simultaneous. Arrow indicate the resulting polarization, taken from reference [63]. (2) View of proposed charge redistribution within bilayer of the  $\text{FeO}_2$  triangular lattices in  $\text{LuFe}_2\text{O}_4$ . The interlayer charge-ordering inducing electric polarization is indicated by red arrow, taken from reference [62].

Surprisingly in 2012, charge ordered crystal structure refinement based on single crystal x-ray diffraction by J.deGoort et al disproved the polar nature of Fe/o bilayer [66] and their bond valence sum calculation supported the charged bilayer. Dielectric spectroscopy also suggests absence of any intrinsic ferroelectricity. Hence the  $\text{LuFe}_2\text{O}_4$  is now can be



excluded from this category. Another most likely candidate in this class of system is classical magnetite. Magnetite exhibit first order metal-insulator transition associated with charge ordering around 120 K. Theoretical calculations indicated that ferroelectricity in this material originates from the  $\text{Fe}^{2+}/\text{Fe}^{3+}$  charge order [62, 67]. However, microscopic experimental proof of intrinsic polarization switching in magnetite is still absent. This is the motivation of our work, to prove/disprove the CO-based ferroelectricity in magnetite by microscopic experiments. CO based ferroelectricity specifically in magnetite will be discussed in detail in chapters 4 and 5.

## Chapter 2

### Experimental methods and theoretical background

In the present thesis, single crystals of high quality magnetite ( $\text{Fe}_3\text{O}_4$ ) and oxygen deficient strontium ferrite ( $\text{SrFeO}_{3-\delta}$ ) were grown and various physical properties were studied using different experimental techniques. This chapter provides a brief description of sample preparation and the crystal growth unit used. Details of the different in-house laboratory techniques used to characterize the samples are presented. A brief description of the different instruments used for microscopic studies at the large scale neutron and x-ray diffraction facilities and its theoretical background are also provided.

## 2.1 Synthesis of polycrystalline powders and growth of single crystals

Subtle changes in the composition adversely affect the physical properties of the system. One of the great challenges is to obtain high quality single crystals with the fine control over the composition. Therefore extreme care was taken during the synthesis.

### 2.1.1 Solid state reaction route

The starting point for a single crystal growth is a polycrystalline precursor. The polycrystalline precursors were prepared by conventional solid state synthesis method. This method is most commonly used to prepare polycrystalline materials by heating a homogeneous mixture of two or more starting materials. The heating temperature required to obtain a desired phase depends very much on the form and reactivity of the reactants. In order to get a phase pure sample, very high quality starting materials are weighed and taken in an appropriate amount (stoichiometric ratio), mixed well in a ball mill to reduce the grain size and hence maximize the surface area and homogeneity, which is crucial for the better reaction. Then the mixture is heated in a crucible to a desired temperature several times by regrinding in between until a phase-pure polycrystalline sample was obtained. For many oxides the oxygen stoichiometry is not fixed and an appropriate oxygen partial pressure needs to be provided during synthesis. Within this thesis this was the case both for magnetite, the synthesis of which is described in detail in section 4.3 and for  $\text{SrFeO}_{3-\delta}$  in section 6.2.

### 2.1.2 Crystal growth by optical floating zone technique

The oxide crystals studied in the present thesis have relatively high melting points and can only be grown at high temperatures (much higher than  $1000^{\circ}\text{C}$ ). Single crystals of various congruently and incongruently melting oxides can be grown by the floating zone and traveling solvent floating zone techniques [68, 69]. This technique has been considered as one of the most effective techniques available for the growth of phase pure bulk single crystals of large size of compounds with very high melting point. An illustration of floating zone furnace is presented in figure 2.1. The polycrystalline powder, as prepared by the method described in the previous section was made in to very dense rods of length  $\sim 8 - 10$  cm with a diameter of  $\sim 6 - 8$  mm, by filling tightly in to a latex tube homogeneously without any voids. Then it was pressed in a hydrostatic press and sintered again at high temperature by placing them in ceramic boats or in a platinum foil. As prepared feed and seed rods were aligned in a four mirror furnace in such a way that the tips of both the rods meet at the focal point of ellipsoidal mirror (see figure 2.1). The halogen lamps are located at one of the foci of the semi-ellipsoidal mirrors. The growth chamber is enclosed by a quartz tube to employ different gases to provide the desired atmosphere. Providing suitable gas atmosphere or partial pressure is necessary for most of the oxide crystals to stabilize the phase or to tune the stoichiometry. The growth was started by melting and eventually touching the tips of feed and seed rods and establishing molten interface called floating zone. After the zone is formed it was moved upwards by moving the feed and seed setup down (minimum growth rate used : 1 mm/hour, maximum growth rate used: 5 mm/hour). As the melt moves up from the hot zone, the liquid cools and crystallizes on the seed rod. For a better homogeneity of the material and to avoid the defects the feed and seed rods were rotated (minimum rotation speed used: feed 12 rpm, seed 11 rpm, maximum rotation speed used: feed 20 rpm, seed 18 rpm) in opposite directions with experimentally established rates. Usually several growth-runs have to be performed in order to optimize the various parameter and to obtain a high quality single crystals. As grown crystals were characterized and used in different scattering studies, which are described in the following sections.

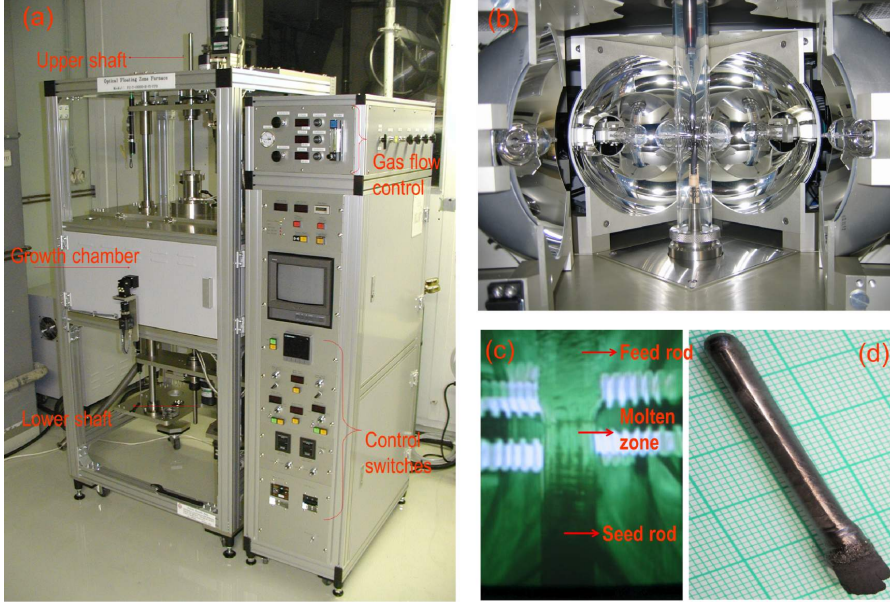


Figure 2.1: (a) The optical floating zone furnace FZ-T-10000-H-VI-VPO, (b) inside view of the growth chamber: at the center two rods can be seen fixed to upper (feed rod) and lower shaft (seed rod) and fixed with a quartz tube. Four halogen lamps and hemi-ellipsoidal mirrors are also seen (c) the growth chamber as seen in CCTV during a growth and a schematic of the growth process and (d) as grown  $\text{Fe}_3\text{O}_4$  single crystal.

## 2.2 Magnetic properties

### 2.2.1 AC and DC magnetization measurements

As grown crystals were studied using a wide range of in-house experimental techniques covering many properties of the material. In case of  $\text{Fe}_3\text{O}_4$ , the quality of the crystals were tested by thermoremanent magnetization measurement, performed at MPMS and the specific heat measurements were performed at PPMS. The results of which are discussed in the chapter 4. Also different physical properties (magnetometry, isothermal magnetization and ac susceptibility) of oxygen deficient  $\text{SrFeO}_{3-\delta}$  crystals were investigated (see chapter 6).

AC and DC magnetic measurements are two different tools that provide different supplementary information about magnetic properties. AC magnetic measurement provide the information about magnetization dynamics, because the induced sample moment is time dependent. During the measurement, the sample is centered within a

coil and a small external AC field is superimposed on the DC field. This will result in a time varying magnetization that a second detection coil senses. In a small AC field the induced AC moment is  $M_{AC} = \frac{dM}{dH} H_{AC} \sin(\omega)t$ . where  $H_{AC}$  is the amplitude of the driving field,  $\omega$  is the driving frequency and  $\chi_{ac} = \frac{dM}{dH}$  is the slope of the M-H curve, called AC susceptibility, which is the quantity of interest in AC magnetic measurements. The AC susceptibility measures the magnetic susceptibility as a function of frequency and temperature, and it is capable to separate the real and imaginary component of the complex susceptibility.

In case of DC magnetic measurements the sample is kept quasi stationary during the measurement time and the equilibrium value of the magnetization in a sample is measured. The sample is subjected to and magnetized by a static dc field and magnetic moment of the sample is measured as a function of temperature, as well as M-H curve is measured by varying the applied magnetic field by keeping the temperature constant.

### 2.2.1.1 SQUID option at MPMS

The Superconducting Quantum Interference Device (SQUID) consists of a closed superconducting loop extending to the pickup coils at the sample position employing Josephson junctions (junction between two superconductors separated by a thin insulating barrier) in the loop's current path [70, 71]. The SQUID option at magnetic property measurement system (MPMS) is the most effective instrument to measure magnetic moments of liquid or solid samples. It is a very sensitive magnetometer which can measure magnetic moments in the order of  $10^{-7}$  emu and even below. In the presence of a constant bias current in the SQUID, the measured voltage has an oscillatory dependence on the phase change of the two junctions which in turn is a function of magnetix flux change. Therefore measurement of the oscillations is a measure of the flux change. The SQUID magnetometer used in our laboratory was manufactured by Quantum Design and has a temperature range from 1.9 to 400 K and up to 800 K with oven option and the magnetic field ranges from -7 to +7 Tesla. There are two different options which can be used to measure the magnetization, DC and RSO. In DC option the sample is moved through the coils in discrete steps, in Reciprocating Sample Option (RSO) a servo motor rapidly oscillates the sample.

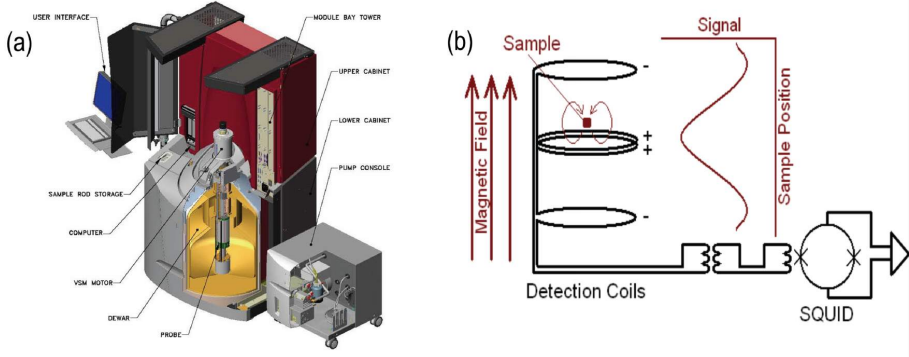


Figure 2.2: Schematic of a SQUID magnetometer setup for RSO option, taken from reference [72]

### 2.2.1.2 VSM option at PPMS

The Quantum Design vibrating sample magnetometer (VSM) option at physical property measurement system (PPMS) is a sensitive DC magnetometer for fast data collection. The basic measurement is performed by oscillating the sample near a detection (pickup) coil and synchronously detecting the voltage induced. VSM option in PPMS uses a compact Gradiometer pick up coil and a larger amplitude of oscillation (1-3 mm Peak) at 40 Hz frequency of oscillations. This allows the system to resolve changes in magnetization of the order of  $10^{-6}$  at a comparatively higher data acquisition frequency of 1 Hz. The VSM option consists primarily of a VSM linear motor transport (head) for vibrating the sample, a coilset puck for detection, electronics for driving the linear motor transport and detecting the response from the pickup coils, and a copy of the MultiVu software application for automation and control. Detailed description can be found in the user's manual [73]. The measurement can be performed in the temperature range of 1.9 K to 400 K (up to 800 K with the oven option) and the external magnetic field can be varied from 0 T to  $\pm 9$  T.

### 2.2.1.3 ac Susceptibility

Ac susceptibility measurement involves an application of varying magnetic field  $H_{ac}$  to a sample and recording sample response by a sensing coil. In this case  $\chi$  can be written as:

$$\chi_{ac} = \frac{dM}{dH_{ac}} \quad (2.1)$$

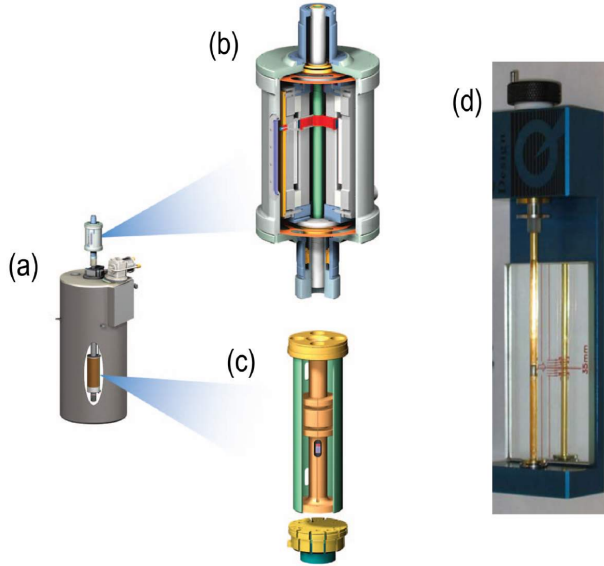


Figure 2.3: (a) SQUID magnetometer setup (b) schematic of RSO option (c) sample holder and PPMS-VSM mounting station, taken from reference [73]

In an ac-measurement the moment of the sample is changing in response to an applied ac field. Thus the dynamics of the magnetic system can be studied. An ACMS option is used at the instrument PPMS to measure the ac susceptibility of the sample. In a typical ACMS alternating AC excitation is provided by an AC-drive coil and a detection coil set inductively responds to combination of sample moment and excitation field. The drive coil consisting of copper along with the detection coils are used as PPMS insert and is connected to the superconducting DC magnet of PPMS. Maximum applicable drive field depends upon the frequency applied and temperature of the PPMS probe, but in any time minimum of  $\pm 10$  Oe can be applied within 10 HZ to 10 KHz frequency limit. At lower temperature and low frequency higher field can be applied. The benefits of this option is, as it measures frequency dependent of real and imaginary part of complex susceptibility and also provides an opportunity to measure higher harmonics of real and imaginary part of complex susceptibility. From this measurement one can get information about relaxation process, relaxation time, spin glass nature of the magnetic system studied [74].



## 2.3 Thermal properties

### 2.3.1 Specific heat

Specific heat (heat capacity) measurements of sample provides information about the lattice, electronic and magnetic properties of the material. In particular, specific heat measurements are well suited to describe phase transitions in any material. The Quantum Design heat capacity option measures the heat capacity at constant pressure,  $C_P = (dQ/dT)_p$ . Where,  $dQ$  is the amount of heat added to the system to raise its temperature by an amount  $dT$ . The schematic diagram of the sample platform with the heater and thermometer connection is presented in figure 2.4. The small connecting wire at the bottom of the platform provide an electrical connection to both the heater and thermometer and also gives the structural support to the platform. A very small amount of sample was taken and mounted on to the platform by using a thin layer of grease, which provides a good thermal contact between the sample and platform [75]. Before the sample measurement, a background measurement was performed by measuring the specific heat of the grease and later it was subtracted from the sample measurement. In the present thesis specific heat measurements were performed to check the sample quality e.g., by checking the presence, location and width of first order phase transition in magnetite. Specific heat has a pronounced anomaly at the transition.

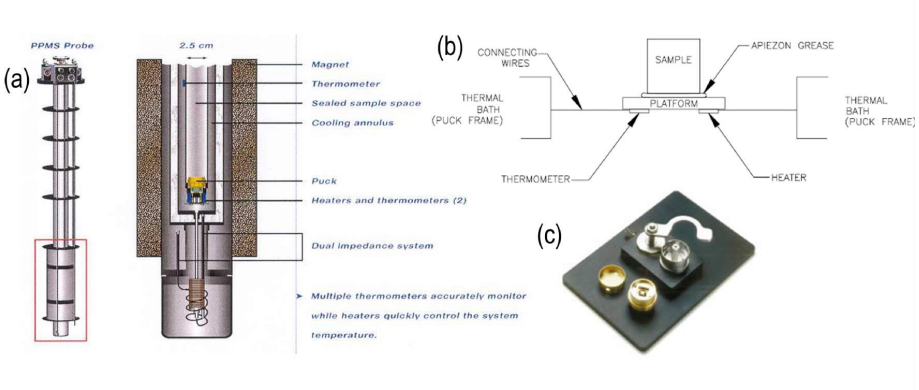


Figure 2.4: Thermal connections to the sample and to the sample platform in PPMS heat capacity option.

## 2.4 Scattering theory

Different types of scattering techniques were used to investigate various microscopic properties of the system. The choice of scattering methods for the present study is to provide the unambiguous proof for the long standing question of presence of ferroelectricity in magnetite and to study the spin-correlation and magnetic structure of  $\text{SrFeO}_{3-\delta}$ .

### 2.4.1 Basics of diffraction

Any diffraction experiment is a Fourier transformation from direct or crystal space into reciprocal space (only in the Born approximation). The intensity collected in the detector  $I$  is directly proportional to the squares of the crystallographic structure factors  $F$  *i.e.*,  $I \propto |F|^2$ , which leads only to the absolute value of  $F$ ,  $|F|$ , while the phase information is lost. Finding the phase is the main obstacle in crystallography, which can be achieved by different ways, for example direct methods, anomalous x-ray scattering *etc* [20, 76].

In neutron scattering, the simplest model for the diffraction experiment is obtained by solving the schrödinger equation (2.2) using the Green-function (2.3) within the Born approximation for a plane wave impinging on a localized potential  $V(\vec{r})$ .

$$H\psi = \left( -\frac{\hbar}{2m}\Delta + V(\vec{r}) \right) \psi = i\hbar \frac{\delta}{\delta t} \psi \quad (2.2)$$

$$G(\vec{r}, \vec{r}') = \frac{\exp(ik|\vec{r} - \vec{r}'|)}{4\pi |\vec{r} - \vec{r}'|} \quad (2.3)$$

The differential equation (2.2) is transformed into an integral equation using (2.3).  $\vec{r}$  and  $\vec{r}'$  are the particle's position. For an incoming plane wave, the wavefunction far away from the scattering region (Fraunhofer approximation),  $|\vec{R}| = |\vec{r} - \vec{r}'|$  is much bigger than the size of the  $|\vec{r}'|$ , the equation 2.3 must have the form

$$\Psi_{\vec{k}(\text{Born})}(\vec{r}) = \underbrace{e^{i\vec{k}\vec{R}}}_{\text{incoming}} + \underbrace{\frac{e^{ikR}}{R} \frac{2m}{4\pi\hbar} \int V(\vec{r}) e^{i\vec{r}'\vec{Q}} d^3r'}_{\text{elastic-scattered}} \quad (2.4)$$

The scattering vector,  $\vec{Q} = \vec{K}_f - \vec{K}_i$ , is the difference between the two wave vectors.  $\vec{K}_i$  is the wave vector of the incident wave with wavelength  $2\pi/\lambda$  and  $\vec{K}_f$  is the scattered wave. The first Born approximation is valid for a weak scattering potential. In this case the multiple scattering is of lesser importance, and an approximation of the scattering waves to first order inside the target potential is accurate enough. The second term in the right

hand side of the equation 2.4 represents the scattering amplitude,  $f(\vec{Q})$ . Figure 2.5(a) shows a sketch of scattering geometry in case Fraunhofer approximation.

A scattering experiment measures the intensity distribution as a function of scattering vector  $\mathbf{I}(\vec{Q})$  and the scattered intensity is proportional to the so-called differential scattering cross section, that can be schematically defined by figure 2.5(b). The angular dependence of scattering in elastic case is given by:

$$\frac{d\sigma}{d\Omega} = \int_0^\infty \frac{d^2\sigma}{d\Omega dE'} dE' \quad (2.5)$$

The total scattering cross section gives us the total scattering probability in all the  $4\pi$  solid angle, independent of changes in energy and scattering angle:

$$\sigma = \int_0^{4\pi} \frac{d\sigma}{d\Omega} d\Omega \quad (2.6)$$

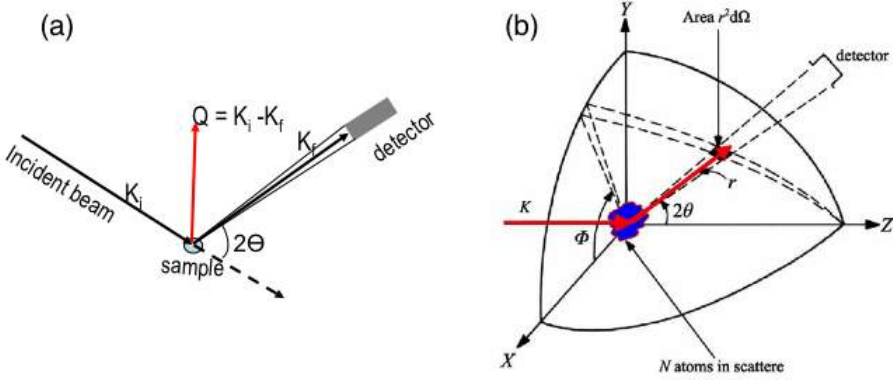


Figure 2.5: (a) Scattering geometry in the case of Fraunhofer approximation. (b) Geometry used for the definition of the scattering cross section, taken from reference [77]

## 2.4.2 Bragg's law

The diffraction process from a periodic arrangement is described by well known *Bragg's law*,  $n\lambda = 2d_{hkl} \sin\theta$ , gives the diffraction condition for the constructive interference. Here 'n' is an integer,  $d_{hkl}$  inter-planar distance of parallel lattice planes with Miller indices  $hkl$ ,  $\lambda$  is the wavelength of the incident x-rays,  $2\theta$  is the diffraction angle. A pictorial illustration of Bragg's law is presented in the figure 2.6. Bragg

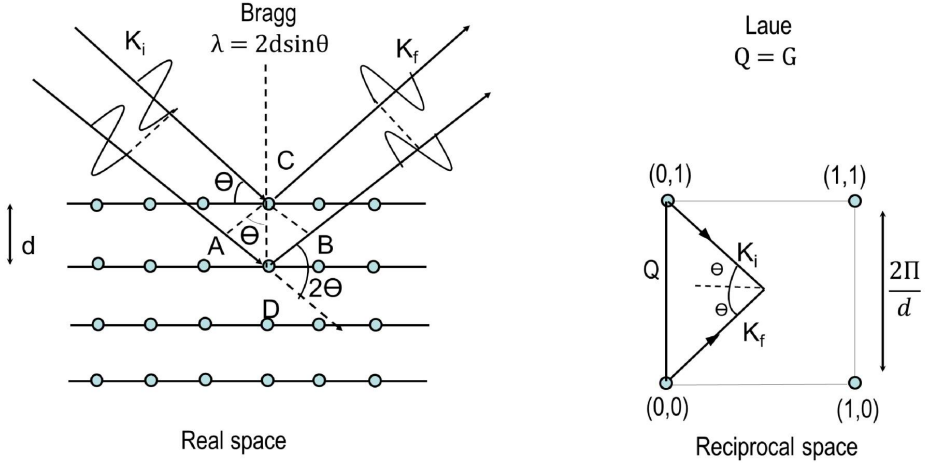


Figure 2.6: The equivalence of Bragg's law and Laue condition from a 2-D crystal

proposed that the incident x-rays produces diffraction patterns (Bragg peak) only if the constructive interference of reflection off the various planes takes place satisfying the above condition. Thus when the 2-D diffraction pattern is recorded, it shows concentric rings (Debye-Scherrer lines) of scattered intensities corresponding to various  $d_{hkl}$ -spacings in the crystal lattice for randomly oriented powder crystallites. The positions and intensities of the peaks are used to identify the underlying structure of the material for e.g., by refining the data with different models [76, 78].

### 2.4.3 Reciprocal lattice and Ewald construction

The reciprocal lattice is the set of vectors  $G$  in reciprocal space (Fourier space to direct space) that satisfy the requirement

$$\vec{G} \cdot \vec{R}_n = 2\pi \times \text{integer},$$

$R_n$  is the lattice vector in real space, which can be written as :  $R_n = n_1 a_1 + n_2 a_2 + n_3 a_3$ . Here,  $(a_1, a_2, a_3)$  are the basis vector of the lattice and  $(n_1, n_2, n_3)$  are integers. The  $G$  vectors in the reciprocal lattice is given by  $G = ha_1^* + ka_2^* + la_3^*$  where

$$a_i^* = 2\pi \frac{a_2^* \times a_3^*}{a_1 \cdot (a_2 \times a_3)}, \text{ and cyclic}$$

Ewald construction is a geometrical construction which helps us to visualize the properties of Bragg's law in reciprocal space. The constructive interference in diffraction process occurs only when the reciprocal lattice points lies on the surface of the Ewald sphere, which is demonstrated in the figure 2.7. Since both wave vectors have the same length the scattering vector must lie on the surface of a sphere of radius  $2\pi/\lambda$ . This is called Ewald sphere. For diffraction to occur the scattering vector must be equal to reciprocal lattice vector i.e.,  $\vec{Q} = \vec{G}$ . This is known as "Laue condition". For elastic scattering, the scattering triangle shown in figure 2.7 yields the formula

$$|Q| = \frac{4\pi \sin\theta}{\lambda} \quad (2.7)$$

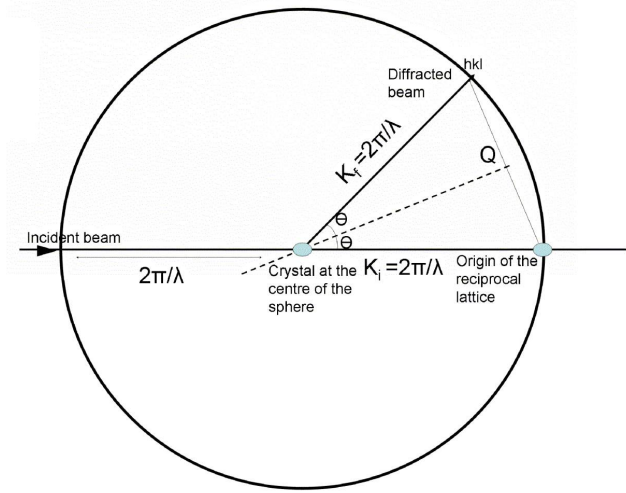


Figure 2.7: Ewald construction

#### 2.4.4 Diffraction from a crystal

Bragg's law only describes the condition for constructive interference, which is necessary for diffraction to occur, but it does not enable us to calculate the intensity of the scattering. For that we need to know the structure factor,  $F$ , of the crystal which is a product of two terms:

$$F^{crystal}(Q) = \sum_{r_j} \underbrace{f_j(Q)}_{\text{atomic form factor}} \overbrace{e^{iQr_j} e^{W_j(Q,T)}}^{\text{unit cell structure factor}} \underbrace{\sum_{R_n} e^{iQR_n}}_{\text{lattice sum}} \quad (2.8)$$

where  $r_j$  is the position of atoms with respect to any one particular lattice site and  $W_j$  is the Debye-Waller factor (DWF) which is defined as

$$W_j(Q, T) = \frac{1}{2} Q^2 \langle (U_j(T))^2 \rangle \quad (2.9)$$

The DWF is  $Q$  dependent.  $(U_j(T))$  is the thermal displacement of  $j^{th}$  atom from its equilibrium position. The DWF describes the effect of the lattice vibrations on intensities from the Bragg peak. The effect of these vibrations smear out the Bragg peak intensities and appear as diffuse scattering away from the Bragg peak positions. These diffuse intensities are known as thermal diffuse scattering or inelastic phonon scattering.

## 2.5 X-ray diffraction

X-ray diffraction is one of the powerful methods to study the structure of condensed matter on atomic scale. X-rays are relatively short wavelength (much shorter than visible light), high energy beams of electromagnetic radiations. Another description of X-rays is as particles of energy called photons. All electromagnetic radiation is characterized either by its wave character using its wavelength  $\lambda$  or its frequency  $\nu$  or by means of its photon energy  $E$ . The relation between the energy and wavelength of X-ray photon is,

$$E = \frac{hc}{\lambda} = \frac{h}{2\pi} k \quad (2.10)$$

where  $C$  is the speed of light and  $h$  is Planck's constant.

In the electromagnetic spectrum X-rays can be found between ultraviolet light and high energy gamma rays. The energy of X-rays ranges between about 0.1 to 100 keV or in terms of wavelength, 0.01 and 10 nm. X-rays with energies less than 2 keV are called soft X-rays. The standard method used to produce X-rays is by accelerating electrons with high voltage and allowing them to collide with a metal target. When electrons are decelerated upon collision with the metal target, the X-rays are produced. Target metals have their characteristic emission lines corresponding to their electronic transitions with higher intensities and rest remains background. But in this process the energy efficient is only 0.1 %, the rest will be lost in heat. Another alternative and extremely powerful method to produce and use X-ray radiations is from synchrotron, which are usually linear electron accelerators combined with storage rings. Here X-rays are produced by changing the electrons speed vector, i.e. directions of path of high energy moving electrons by

bending magnets or undulators. The main advantage of synchrotron is the tunability of X-ray energy. In the present study we have used hard X-rays at synchrotron sources at DESY in Hamburg and at APS in Argonne national laboratory, USA.

X-ray diffraction involves the measurement of the intensity of X-rays scattered from electrons bound to atoms. Hence the X-rays scattering power, also known as atomic form factor  $f(\vec{Q})$ , increases with the increased number of electrons. The scattering process of photons has both coherent (Rayleigh scattering) and incoherent components (Compton scattering). Elastic scattering of electromagnetic radiation by a charged particle is described as Thomson scattering. The atomic scattering is strongly depends on the types of radiation involved. In the case of X-ray,  $f(\vec{Q})$  is the Fourier transform of the atomic electron density,  $\rho(r)$ , of a particular element.

$$f(\vec{Q}) = \int \rho(\vec{r}) e^{i\vec{Q}\vec{r}} d^3r \quad (2.11)$$

The atomic form factor varies with scattering angle  $2\theta$ .  $f(\vec{Q})$  decreases with the increasing scattering angle and is approximately proportional to number of electrons when  $\theta = 0$ .

### 2.5.1 Laue method

In order to check the single crystalline nature and to orient the crystal the real-time Laue camera was used (Figure 2.8). In this method a white X-ray beam (beam with different wavelengths) is incident on a stationary crystal, which is mounted on a goniometer. In a stationary crystal the orientation of the crystal selects the wavelength out of the white beam to give constructive interference. The computer control of goniometer allow the sample to rotate and translate in each direction. Collimated beam passes through the center of the flat area detector towards the sample and then back diffracts from the sample to the detector. The diffracted pattern were collected using the charged-coupled device connected to the computer. Image Pro Express software allows control over the data collection, including exposure times and number of images recorded. For a known crystal structure the Laue pattern can be simulated using OrientExpress [79] software. By comparing the obtained Laue pattern by simulation and from experiment it is possible to orient the crystal.

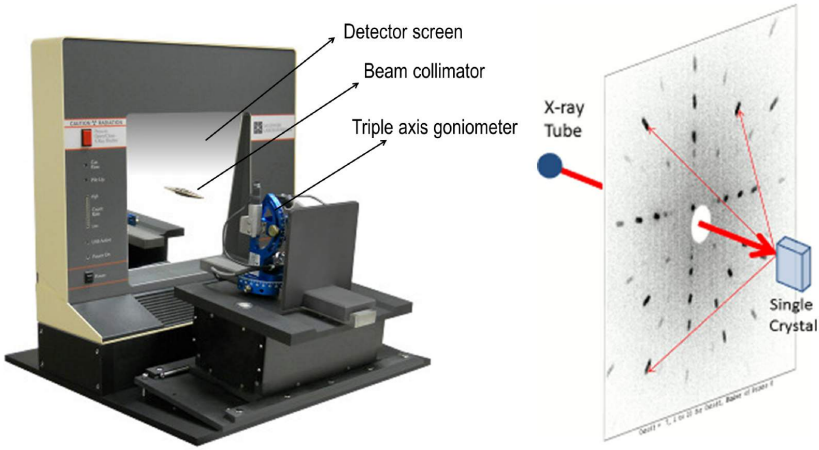


Figure 2.8: Real time, back reflection, X-ray laue camera, taken from reference [80]

## 2.5.2 Powder X-ray diffraction

Compared to single crystal diffraction, the diffraction of powder samples are relatively weak because of the random orientation of microcrystals. The Bragg condition will be met only for those crystals which are in the proper orientation for any particular scattering angle.

In order to determine the phase purity and crystallinity of the prepared sample, in-house laboratory powder X-ray diffraction technique was used. All the XRD patterns were collected in transmission geometry using a Huber diffractometer operating with  $\text{Cu-K}\alpha$  radiation and equipped with a G670 Guinier camera with integrated imaging plate detector. A schematic view of powder diffractometer setup with Guinier geometry is presented in figure 2.9. A small amount of sample was mounted on a flat sample holder (a thin polythene film) and illuminated with X-rays of fixed wavelength and the intensity of the transmitted radiation is recorded by an image plate detector.

## 2.5.3 Beamline P09 at PETRA III

The beamline P09 located at the sector 6 of the PETRA III experimental hall and designed for hard X-ray experiments in the range of 2.7 to 50 keV. The choice of this beam line for our experiment was due to: 1) the need of high energy X-ray, above Fe K-absorption edge, to observe the anomalous scattering and 2) feasibility to set up the high voltage supply



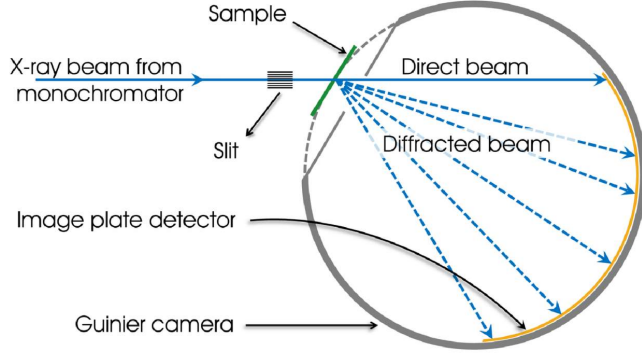


Figure 2.9: A schematic view of the powder diffractometer in Guinier geometry.

which was needed for the present study. Further, state-of-the-art techniques and set ups used during the experiment to study the ferroelectricity in magnetite is discussed in the chapter 5. We have performed experiments in the 6-circle diffractometer and used different energies above the Fe-K absorption edge. The 6-circle diffractometer along with the beam collimator, analyzer and the point detector is shown in the figure 2.10 and its parameters are tabulated in 2.1. Out of 6-circles, 4-circles ( $\theta$ ,  $\mu$ ,  $\chi$ ,  $\phi$ ) are for position control of the sample and 2 ( $\delta$ ,  $\gamma$ ) for detector and all these axes can be changed independently. Horizontal as well as vertical diffraction with a large vertical scattering angles can be performed at the instrument. The cryostat is mounted on the  $\phi$  cradle which is equipped with the Huber 512.12M motorized xyz-cryostat( designed to hold and position a cryostat) carrier and can be rotated full  $360^\circ$ , but will limit the  $\chi$  rotation. After mounting the sample, it will be covered by beryllium domes. The outer dome (0.5 mm thickness) is for vacuum, the second dome (0.38 mm thickness) will act as heat shield and the third dome (0.38 mm thickness) is for gas exchange (alternative to use liquid helium). Further details of this beam line can be found in the article [81].

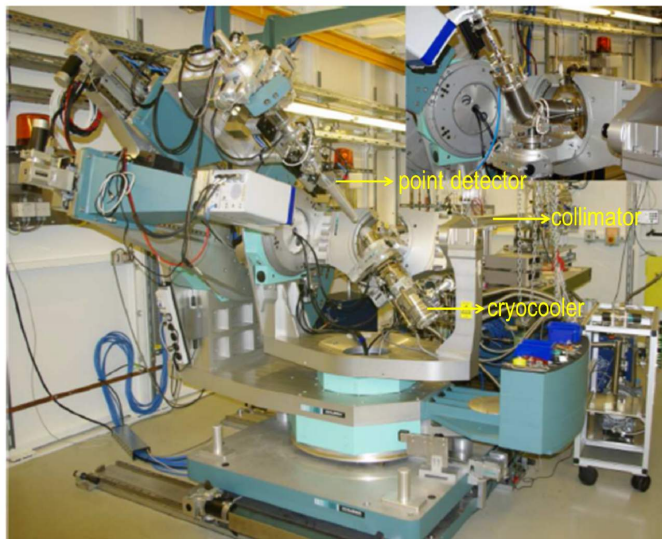


Figure 2.10: Six circle diffractometer at the beamline P09, taken from reference [81].

Table 2.1: Parameters of the 6-circle diffractometer. The values are taken from the reference [81]. Spheres of confusion (SOC) are obtained for loaded sample stage and detector arm.

Motor	Range (deg)	Accr (arcsec)	SOC( $\mu\text{m}$ )	comment
$\theta$	-10/+90	0.18	30	vertical $\theta$
$\delta$	-30/+180	0.36	20	vertical $2\theta$
$\mu$	$\pm 30$	0.18	25	horizontal $\theta$
$\gamma$	-20/+180	0.36	60	horizontal $2\theta$
$\chi$	$\pm 90$	0.36	15	without cryostat
	$\pm 48$	0.5	30	with cryostat
$\phi$	0-360	0.18	5	

### 2.5.4 Beamline 6-ID-D at APS

6-ID-D side station is a high energy X-ray beamline located at the advanced photon source (APS). The energy range can be varied between 70-130 keV with the use of three different facets (cut along the facets) of annealed silicon crystals (Si 111: 28-54 keV, Si 311: 53-103

keV: Si 331: 69-136 keV). We have used this beam line to study the diffuse scattering on magnetite. With high energy X-ray, because absorption is less penetrating power is more, and so same sample can be used both for neutrons and X-ray experiments. The side station uses a Bragg double monochromator in horizontal geometry. Further specifications about the beamline can be found in the reference [82]. The single crystal was mounted on a four circle diffractometer, which is also equipped with a cryostat. The diffracted photons were detected on a circular detector, Mar345 image plate, with 345 mm diameter and  $100\mu\text{m} \times 100\mu\text{m}$  pixel size each with a dynamic range of 17bit intensity resolution. In order to get a good Q resolution or to get the wide Q rage, sample detector distance can be varied, typically between the 0.25 to 1.6 m. Since we were interested in diffuse scattering studies, the crystal was oriented in  $hhl$  plane and we mapped the reciprocal space by an adequate sample movement and by using the X-ray energy of 100 keV. Strong Bragg reflections were covered by lead pieces in order to avoid the over-exposure, which may cause damage to the image plate. The obtained results are discussed in the chapter[4].

## 2.6 Neutron scattering

A neutron is an uncharged elementary particle with spin  $1/2$ , mass  $m = 1.675 \times 10^{-24}$  kg and a magnetic moment of  $\mu_n$  of -1.9132 nuclear magnetons. The Kinetic energy of a free neutron is  $E = \frac{1}{2}mv^2$ . The wave nature of the neutrons can be described by the de Broglie formalism  $\lambda = h/\sqrt{2mE}$ . Neutrons can be produced either by fission reaction (fission of  $\text{U}^{235}$  in a chain reaction) or by bombarding heavy metal with high energy protons in a spallation source. Depending on the energy range of neutrons, from 0.1 meV to 100 meV, they are called as thermal and cold neutron. Neutrons with above 100 meV energy range are called hot neutrons. Neutron spins interacts with magnetic moments of the sample allowing to study of magnetic structure and excitations of the sample. This is one of the main advantages of neutrons over X-rays. The theory of neutron scattering is briefly explained in the following sections. More explanations can be found in the references [83, 84].

### 2.6.1 Nuclear scattering

Neutrons interact strongly with nuclei through the strong nuclear force. Hence in any neutron experiments the total scattering contains a major contribution from nuclear elastic scattering because of the short range of nuclear force. The interaction potential of

neutron with nuclei  $j$  at the position  $r_j$  is well approximated by the Fermi pseudopotential,

$$V_N(\vec{r}) = \frac{2\pi\hbar}{m_n} \sum_j b_j \delta(r - r_j) \quad (2.12)$$

where  $b_j$  's are the scattering amplitude of the  $j^{\text{th}}$  atom and  $m_n$  is the neutron mass. The neutron wavelength is long compared to intra-nuclear distance. Therefore  $\delta$ -potential can be used as part of the Fermi pseudopotential. The Fourier transform of a delta function is unity and thus there is no form factor i.e., the scattered amplitude,  $b$ , is independent of  $Q$ . This is in contrast to X-ray scattering where the scattering occurs from the electron cloud and for neutron it is point like. The nuclear structure factor,  $F_N$ , can be written as:

$$F_N(\vec{Q}) = \sum_j b_j e^{i\vec{Q}\vec{r}_j} e^{W_j(Q,T)} \quad (2.13)$$

where the sum runs over all atoms  $j$  and  $W_j$  is the Debye-waller factor which takes account of temperature dependent of fluctuations of the atom. The coherent nuclear scattering (Bragg scattering by crystal lattice planes) cross section is given by

$$\frac{d\sigma}{d\Omega} = N \frac{(2\pi)^3}{V_0} |F_N(Q)|^2 \quad (2.14)$$

Where  $N$  is the number of unit cells in the crystal and  $V_0$  is the volume of the unit cell. The scattering intensity and the amplitude  $b$  is different for same element of the different isotopes, which gives rise to so called incoherent scattering observed as an isotropic background. Hence the total nuclear cross section contains an addition term, incoherent cross section  $N(b - \langle b \rangle)^2$ , which represents neutrons emitted in all directions without interference. Therefore before analyzing the data the background subtraction must be performed. The coherent scattering contain the phase information where incoherent scattering doesn't contain any phase information, it only depends on  $N$ .

## 2.6.2 Magnetic scattering

Magnetic neutron scattering allows us to study the atomic-scale magnetic structure and the dynamic properties of condensed matter. Since neutrons have an intrinsic magnetic dipole moment, they interact with the magnetic field of the electron according to

$$V_M(\vec{r}) = -\vec{\mu}_n \cdot \vec{B}(\vec{r}) \text{ and the magnetic moment, } \vec{\mu}_n = -\gamma_n \vec{\mu}_N \cdot \sigma \quad (2.15)$$

Here the magnetic field  $\vec{B}$  of an electron is due to both spin and orbital part.  $\vec{B}$  can be related to  $\vec{M}$  using Maxwell's equations,  $B = \mu_0 (H+M)$ , the Fourier transform of the interaction potential takes the form:

$$V_M(\vec{Q}) = -\vec{\mu}_n \cdot \vec{B}(\vec{Q}) = \vec{\mu}_n \vec{\mu}_0 \vec{M}_\perp(\vec{Q}) \quad (2.16)$$

The magnetic scattering cross section for elastic scattering when the neutron changes its wave vector and the spin moment projected in to a quantization axis  $z$  from  $\sigma_z$  to  $\sigma'_z$  can be written as,

$$(\gamma_n r_0)^2 \left| -\frac{1}{2\mu_B} \overbrace{\langle \sigma'_z | \sigma \vec{M}_\perp(\vec{Q}) | \sigma_z \rangle}^{\text{scattering amplitude}} \right|^2 \quad (2.17)$$

Where,  $\sigma$  denotes the spin operator and  $\gamma_n$  is the gyromagnetic factor of the neutron.  $\vec{M}_\perp(Q)$  represents the component of the Fourier transform of the sample magnetization, which is perpendicular to the scattering vector  $Q$ .

$$\vec{M}_\perp(Q) = \frac{\vec{Q}}{|\vec{Q}|} \times \vec{M}(\vec{Q}) \times \frac{\vec{Q}}{|\vec{Q}|} \quad (2.18)$$

$$M(\vec{Q}) = \int \vec{M}(\vec{r}) e^{i\vec{Q} \cdot \vec{r}} d^3r \quad (2.19)$$

$$\text{with, } \vec{M}(\vec{r}) = \vec{M}_s(\vec{r}) + \vec{M}_L(\vec{r}) \quad (2.20)$$

It is clear from the equation 2.17 that neutrons only see the component of the magnetization perpendicular to the scattering vector  $Q$ . Magnetic scattering caused by the electron cloud of an atom will not necessarily consists of a spherical wave. Hence the correction factor for the scattering cross section is required, which is obtained by considering the dipole approximation so that we can use the dipole moment of the scattering electrons  $\mu$  instead of complicated  $\vec{M}_\perp(\vec{Q})$ . For transition metals with  $3d$  ions the orbital angular momentum  $L$  is often quenched and only pure spin scattering will be present. Under such circumstances in the dipole approximation the magnetisation can be written as

$$\vec{M}(\vec{Q}) = -g\mu_B f(\vec{Q}) S = f_m(\vec{Q}) \mu \quad (2.21)$$

$f_m(\vec{Q})$  is the magnetic form factor,  $g$  is a function of spin and orbital angular momentum and is equal to 2 for spin-only angular momentum. For spin-only case the, form factor is

the Fourier transform of the normalized spin density  $S(\vec{r})$

$$f_m(\vec{Q}) = \int_{unit} d^3r e^{i\vec{Q} \cdot \vec{r}} S(\vec{r}) \quad (2.22)$$

Since the magnetic scattering caused by the electron cloud of an atom, it does require an atomic form factor: which describes that the scattering amplitude decreases with increasing momentum transfer ( $Q$  dependent). The magnetic form factor is similar to X-ray factor. But only the exception is that the magnetic form factor include more extended density of unpaired electrons. Since only the outer electron in open shells contribute magnetic scattering, the magnetic form factor decreases rapidly with  $Q$  compare to X-ray scattering.

### 2.6.3 Polarization analysis

In order to achieve a separation of magnetic and nuclear scattering cross sections, analysis of the spin of scattered neutron is very beneficial. However, to probe the spin transitions, we need to produce a polarized neutron beam of a definite spin state and analyze the state of the spin after the scattering needs to be done. The polarization of the neutron beam is the expectation value of the neutron spins divided by its modulus,

$$P = 2 \langle \hat{s} \rangle = \langle \hat{\sigma}_\alpha \rangle \quad (2.23)$$

Where  $\sigma_\alpha$  denotes the Pauli-spin matrices given by:

$$\hat{\sigma}_x = \begin{pmatrix} 0 & 1 \\ 1 & 0 \end{pmatrix}, \quad \hat{\sigma}_y = \begin{pmatrix} 0 & -i \\ i & 0 \end{pmatrix}, \quad \hat{\sigma}_z = \begin{pmatrix} 1 & 0 \\ 0 & -1 \end{pmatrix} \quad (2.24)$$

for a spin  $\frac{1}{2}$  particle, the spin up and down states can be written as,

$$|+\rangle = \begin{pmatrix} 1 \\ 0 \end{pmatrix}, \quad |-\rangle = \begin{pmatrix} 0 \\ 1 \end{pmatrix}$$

where,  $|+\rangle$  and  $|-\rangle$  are the eigenvectors with  $+(1/2)\hbar$  and  $-(1/2)\hbar$  respectively. The neutron polarization analysis carried out under the condition of equation 2.24 is considered as longitudinal polarization analysis experiment. The scattering amplitude for the magnetic

scattering can be written as,

$$A(Q) = \langle S'_z | -\frac{\gamma_n r_0}{2\mu_b} \hat{\sigma} \cdot \vec{M}_\perp(Q) | S_z \rangle = \frac{\gamma_n r_0}{2\mu_b} \sum_\alpha \langle S'_z | \hat{\sigma} | S_z \rangle \vec{M}_\perp \alpha(Q) \quad (2.25)$$

where,  $\alpha$  stands for x, y, z directions. After substituting the equation 2.24 in 2.25 we get the matrix element for spin-flip and non-spin-flip scattering:

$$A(Q) = \frac{\gamma_n r_0}{2\mu_B} \times \begin{cases} -\vec{M}_{\perp z}(Q) \\ +\vec{M}_{\perp z}(Q) \\ -\vec{M}_{\perp x}(Q) + i\vec{M}_{\perp y}(Q) \\ -\vec{M}_{\perp x}(Q) - i\vec{M}_{\perp y}(Q) \end{cases} \text{ for } \begin{cases} + \rightarrow + \\ - \rightarrow - \\ + \rightarrow - \\ - \rightarrow + \end{cases} \quad (2.26)$$

With this we obtain two rules for spin-flip and non-spin flip magnetic scattering processes that are spin flip processes can be observed only when  $\vec{M}_\perp(Q) \perp \vec{P}$  and non-spin flip processes can be observed only when  $\vec{M}_\perp \parallel \vec{P}$ . Further, theory of  $xyz$  - polarization analysis used to investigate the spin directions in single crystals of  $\text{SrFeO}_{3-\delta}$  are presented in chapter 6.

## 2.6.4 DNS instrument at MLZ

In order to study the presence of diffuse scattering related to relaxor ferroelectricity in magnetite low temperature diffuse scattering experiment was conducted at the instrument DNS (Diffuse neutron spectrometer) MLZ (Heinz-Maier-Leibnitz Zentrum), Garching. Also, to study the spin structure and isotropic spin correlation in a non-stoichiometric  $\text{SrFeO}_{3-\delta}$  crystals  $xyz$  -polarization analysis was performed. The multidetector instrument DNS is a cold neutron time of flight spectrometer equipped with polarization analysis. The magnetic and nuclear scattering cross section of a single crystal can be extracted by reciprocal space mapping. The schematic diagram of the instrument is shown in figure 2.11. Monochromatic beam with wavelength 4.2 Å was used in the present study. The incident beam is polarized with a curved stack of super mirrors in spin dependent regions of total reflection. Further, to guide and maintain the polarization of the neutron beam a weak magnetic guide field is used. The strength of the guide fields are stronger than the earth magnetic field or any other stray field from the surrounding however, typically weaker in order to not to destroy the sample magnetization. To reverse the polarization and to detect

the sample magnetic properties, a  $\pi$ -spin-flipper is placed in between the polarizer and the sample. On an average the degree of polarization is about 95 % [85]. The presence of  $xyz$ -field coils allows for a change of the polarization at the sample to any desired direction [for further details see chapter 6] and the scattered neutrons are detected by 24 detector tubes filled with  $^3\text{He}$  gas. To analyze the polarized neutrons again a large stack of, curved, supermirrors are kept in front of the detectors. Further details of  $xyz$ -polarization analysis are discussed in the section 6.5.

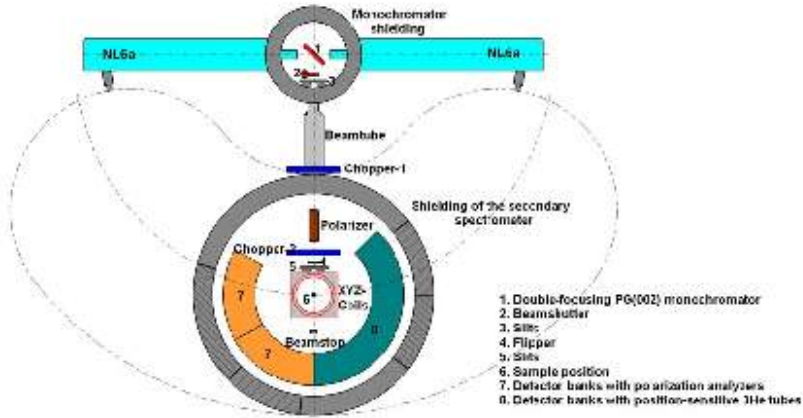


Figure 2.11: Schematic diagram diffuse neutron scattering spectrometer located at FRM II, taken from reference [86]

## 2.6.5 SPODI at MLZ

SPODI is a high resolution thermal neutron powder diffractometer located at the research reactor FRM II in Garching. The instrument and its schematic sketch is shown in the figure 2.12. The instrument is equipped with a stack of 15 focusing germanium wafer crystals with (551) orientation with the mosaicities of  $20'$  in the horizontal and  $11'$  in the vertical directions. Different wavelengths can be achieved by using the different orientations of the Ge monochromator (Ge(551):  $1.548 \text{ \AA}$ , Ge(331):  $2.536 \text{ \AA}$ , Ge(771):  $1.111 \text{ \AA}$ ). The sample is fixed during the measurement. A very good resolution up to very high  $2\theta$  can be achieved by using the high monochromator take-off angle of  $155^\circ$  [see figure 2.12(b)]. The distance between the sample position to monochromator is 5 m and to the detector is 1.12 m. List of available wavelengths are tabulated in 2.2.



Table 2.2: List of available wavelengths at SPODI delivered by Germanium stack monochromator, taken from reference [87]

Reflection	Take off $155^\circ$	Take off $135^\circ$
	5 m distance	2.8 m distance ( $\text{\AA}$ )
Ge(331)	2.536	2.396
Ge(551)	1.549	1.463
Ge(7711)	1.111	1.050

The multidetector array of SPODI consist 80  $^3\text{He}$  detector tubes, which are position sensitive in vertical direction with a resolution of about 3 mm and can cover an angular range of  $2\theta = 160^\circ$ . The two dimensional raw data will be collected. Each detector covers  $2^\circ$  corresponding to  $160^\circ / 80$  detectors. In order to get the desired step width, typically of  $\Delta 2\theta = 0.05^\circ$ , data will be collected by stepwise positioning of the detector array. And hence to collect the complete diffraction pattern in the whole angular range ( $0\text{-}160^\circ$ ) 40 (i.e.  $160^\circ / [180\ ^3\text{He} \times \Delta 2\theta]$ ) individual steps needs to be performed. Further details of the instrument and facilities can be found in the article [87].

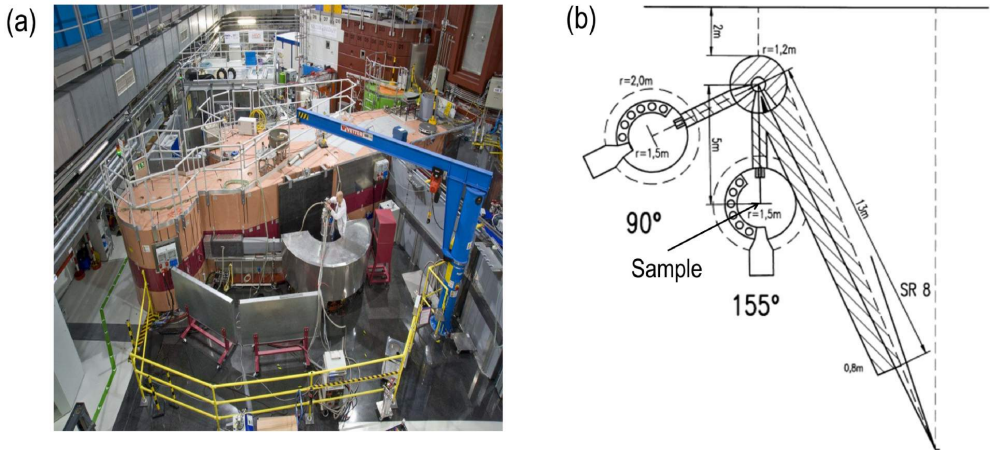


Figure 2.12: (a) The instrument SPODI, taken from reference [88] and (b) its schematic sketch taken from reference [87].  $90^\circ$  and (mainly used)  $155^\circ$  are monochromatic angles.

## Chapter 3

### New dielectric spectroscopy setup

One of the objectives of this thesis was to perform measurements to characterize ferroelectric properties of magnetite and to provide the conclusive proof of ferroelectricity, and thus multiferroicity in this material. Among the wide verity of experimental techniques used to study ferroelectric properties, broad-band dielectric spectroscopy is considered as a key technique, to give evidence of presence or absence of ferroelectricity of a material. The measured permittivity and its frequency, temperature, and electric field dependence is proportional to capacitance, which characterizes the type of ferroelectric behavior (relaxor or normal) and ferroelectric transition. At the time we started our project, there were no detailed investigations by dielectric spectroscopy to provide, particularly the ferroelectric properties of this material. The difficulty associated with the low temperature ferroelectric measurements was the presence of residual conductivity. Quality of the sample also plays a major role in this [for details see chapter 4]. Therefore our aim was, first to grow a high quality single crystal and then to use this crystal for further investigations, including dielectric measurement. However the ability to investigate the ferroelectric properties with an electrical measurement system was not possible at our institute. Therefore the part of the project was to design and build an in-house dielectric measurement setup in the framework of the present thesis. In this chapter we introduce our newly built dielectric measurement setup along with a brief theoretical background of dielectric spectroscopy. Furthermore, results of our test measurements on a multiferroic  $\text{MnWO}_4$  and  $\text{Fe}_3\text{O}_4$  are discussed.

### 3.1 Dielectric response

Ferroelectric materials are insulating materials that exhibit spontaneous electric polarization [89]. The presence of a polarization implies that the crystal structure of these materials lacks a centre of symmetry. The polarization can be switched between different stable states by the application and removal of electric field, called as ferroelectricity which is manifested by well defined ferroelectric hysteresis loop. This switchability is one of the necessary conditions which constitutes a to be ferroelectric.

As mentioned previously, one of the techniques to study the ferroelectric properties of a material is dielectric spectroscopy. A way to measure the dielectric constant is to measure

the capacitance of a parallel plate capacitor containing the ferroelectric substance as a dielectric, in the presence of an electric field  $E$  [as shown in the figure 3.1]. The linear relationship between the induced polarization  $P$  and the applied electric field vector  $E$  can be described as,

$$P = \epsilon_0(\epsilon_r - 1)E = \epsilon_0\chi_e E \quad (3.1)$$

where  $\epsilon_0$  is the dielectric permittivity of vacuum and the dielectric susceptibility  $\chi_e$  describes the linear response reaction of a material to an electric field. The electric displacement field  $D$  related to the polarization  $P$  can be written as,

$$D = \epsilon_0 E + P = \epsilon_0 \epsilon_r E \quad (3.2)$$

Where  $\epsilon_r$  is the relative permittivity.

Ferroelectric materials exhibits characteristics phase transition near the critical temperature  $T_c$  (paraelectric to ferroelectric transition) that are determined by the divergence in the response function  $\chi(\omega)$  i.e., characteristic response in dielectric susceptibility as a function of frequency. The divergence near the  $T_c$  occurs because of the lattice instability. In case of convention displacive ferroelectrics the relation between dielectric constant and the response function is,

$$\epsilon(\omega) = 1 + 4\pi\chi(\omega) \quad (3.3)$$

The nature of fluctuation in the system near the  $T_c$  is provided by the temperature dependence of the response function. Certain ferroelectric materials are characterized by the frequency dependent of diffuse phase transition near the  $T_c$ , called as relaxor ferroelectrics [see details in the chapter 4]. In this case, according to Debye formula with a broad distribution of relaxation times [90], the relation between the dielectric constant can be written as:

$$\epsilon(\omega) = \epsilon(\infty) + \frac{\epsilon(s) - \epsilon(\infty)}{1 + i\omega\tau} \quad (3.4)$$

Here  $\tau$  is the relaxation time and  $\epsilon_0(s)$  and  $\epsilon_0(\infty)$  are the dielectric constant in the static field and at high frequency condition. Empirical Vogel–Fulcher relation approximately describes the distribution of relaxation times [91]. When  $T \geq T_f$  (freezing temperature ),

$$\frac{1}{\tau} = \omega_0 \exp\left[-\frac{E_a}{K_B(T - T_f)}\right] \quad (3.5)$$

Here  $E_a$  is an activation energy and  $K_B$  is Boltzmann constant and  $\omega_0$  is a characteristic hopping frequency.  $\frac{1}{\tau} = \infty$  when  $T \leq T_f$ . In the above equation the long relaxation time implies that with the decreasing temperature the thermally activated reorientations of dipoles which are responsible for polarization will slow down and freeze at  $T = T_f$ .

Dielectric spectroscopy is a unique technique to measure the dielectric response of a material under the influence of an external electric field, in both time and frequency domain. The resulting polarization inside the material relates to the motion of free charge carriers or the permanent dipole moment. The outcome of the measurement is typically given in the form of a dimensionless, complex dielectric-permittivity  $\epsilon^*$ , which depends on the temperature, pressure and composition of the dielectric. This complex dielectric permittivity can be written as a combination of real or in-phase component ( $\epsilon'$ ) and imaginary or out-of-phase component ( $\epsilon''$ ).

$$\epsilon^*(\omega) = \epsilon'(\omega) + i\epsilon''(\omega) \quad (3.6)$$

The loss factor,  $\epsilon''$ , is the measure of energy dissipation per period in the system and is given by  $W = 2\pi f E^2 \epsilon''$ . The frequency dependent  $\epsilon'$  and  $\epsilon''$  are connected through the *Kramers – Kronig* (K-K) relation:

$$\epsilon' = \frac{1}{\pi} \int_{-\infty}^{\infty} \frac{\epsilon''(x)}{x - \omega} dx \quad (3.7)$$

The real part is the “Hilbert transform” of the imaginary part. The K-K relation allows to calculate the static conductivity because dc-conductivity enters only the imaginary component of the complex dielectric permittivity. The figure of merit of a material is decided by the loss angle  $\delta$ , which corresponds to lack of instantaneous polarization to an applied field. The loss tangent can be written as:

$$\tan \delta = \frac{\epsilon''}{\epsilon'}$$

Hence the power dissipation  $W = 2\pi f E^2 \epsilon' \tan \delta$ . The value of loss angle describes how lossy a dielectric is (related to conductivity of a material).

The dielectric material neutralizes the charge at the electrodes, thus increases the storage capacity of the parallel plate capacitor. This generally would contribute to the applied external field. In this case the capacitance of the capacitor, having the surface area 'A'

and the electrodes being separated by a distance 'd', related to dielectric constant as,

$$C = \frac{Q}{V} = \frac{Q}{Ed} = \frac{Q}{\frac{Q}{A\epsilon_0(1+\chi_e)}d} = \epsilon_0(1+\chi_e)\frac{A}{d}$$

$$C = \epsilon_r C_0 \quad (3.8)$$

Where,  $C_0 = \epsilon_0 \frac{A}{d}$  is the capacitance of the capacitor with no dielectric and  $\epsilon_r = (1 + \chi)$  is the relative permittivity. Since the  $\chi$  is always positive the capacitance of the capacitor filled with dielectrics is always larger than one.

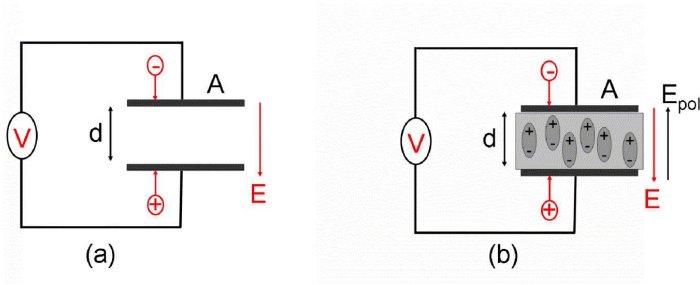


Figure 3.1: (a) A charged parallel plate capacitor in vacuum, (b) A charged parallel plate capacitor in the presence of dielectric.

### 3.1.1 Interfacial or space charge polarization

Interfacial or space charge polarization occurs when the charges are trapped within the interfaces of a materials towards low frequencies [92]. This inherent electrode polarization effect in the interface between electrode and the sample can give rise to giant values of dielectric constant and a strong drop of conductivity which has to be taken in to account for unambiguous determination of the intrinsic properties [93].

### 3.1.2 Dielectric mechanism

Different types of polarization or relaxation mechanisms occur when a dielectric material is subjected to an external electric field. The types relaxation/polarization mechanisms are briefly described in this section.

**Electronic polarization or the charge displacement:** This resonance process happens due to the relative displacement of the electron cloud or the positive and negative electric charge with respect to the center of its atomic nucleus or from their equilibrium

position. This slight separation of charges makes one side of the atom more negative and the opposite side more positive and thus induce the dipole moment.

**Ionic polarization:** As the name suggests ionic polarization happens in ionic materials which already have dipoles but which get canceled due to symmetry of the crystals. In the presence of electric field these cations and anions get displaced in opposite directions giving rise to net dipole moment.

**Dipolar or orientational polarization:** In the case of orientation polarization, the dipoles are independent of each other i.e. they can rotate freely. These dipoles are randomly oriented due to thermal noise. With the application of electric field, these dipoles would turn in to the field direction and induce the polarization.

**Dielectric relaxation:** This relaxation is the combination of both -the movement of the dipoles (dipolar polarization) and the electric charges (ionic polarization) with an applied electric field. Dielectric relaxation usually observed in the frequency range of  $10^2 - 10^{10}$  Hz. With the masses getting larger from electronic to dipolar polarization, the frequency of the applied electric field is increasing as the masses of these entities to be displaced are different, as shown in the figure 3.2. Our present research focuses on the low frequent, ionic polarization, region.

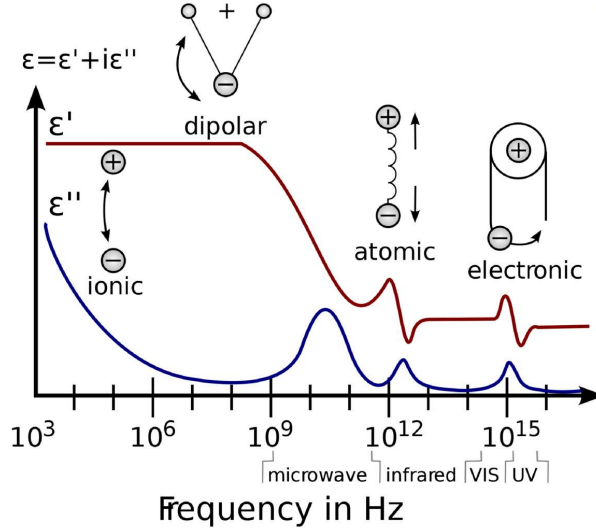


Figure 3.2: Frequency response of dielectric mechanisms.

## 3.2 Experimental setup

As a part of the project, we have designed a sample holder and built up an in-house dielectric measurement setup. The description of the measurement technique is briefly explained in this section.

The sample holder/insert was designed in such a way that the capacitance and the dielectric loss of the sample can be measured with the electric field both in parallel and perpendicular direction to the external magnetic field. The probe head and bottom are shown in the figure 3.3. After mounting the sample on the bottom part of the probe, the bottom is covered by two thin layers of alumina cap in order to provide the required vacuum. The sample chamber can be continuously pumped by the external turbo pump to maintain the necessary high vacuum inside the chamber. The experiment can be performed in the temperature range from 2 K to 400 K, in the magnetic field up to 14 T.

A frequently encountered difficulty with single crystal is to prepare them with below  $\sim 100\text{ }\mu\text{m}$  thickness, needed to resolve small dielectric constants with a given capacitance sensitivity. Since the sensitivity of a capacitance is directly related to sample geometry the resulting dielectric constant can be small. To relax this thickness requirement as much as possible we aimed for the maximum capacitance sensitivity possible. Therefore we wanted a capacitance bridge which can measure the capacitance with as high sensitivity as possible,

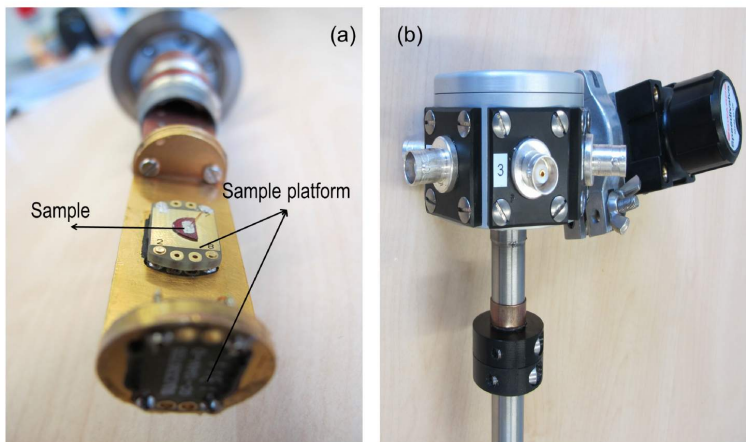


Figure 3.3: (a) The bottom part of the sample insert. The sample can be mounted both in parallel and perpendicular to the magnetic field. (b) Top part of the sample insert. The sample chamber can be pumped continuously using an external turbo pump.



certainly below 100 aF. The measurement presented in the figures 3.6 and 3.7 were performed with an ultra high precision capacitance bridge 'Andeen-Hagerling 2700A' (AH 2700A) that offers frequency range from 50 Hz–20 kHz (26 discrete frequencies). Some of the performance specification includes: it can measure the accuracy for a small-capacitance samples better than 1 aF at 1 kHz and measures extremely low loss-down to dissipation factor of,  $\tan(\delta) \times 1.5 \times 10^{-8}$ , a resistance up to  $1.7 \times 10^6 \text{ G}\Omega$ . An external dc bias voltage up to 100 V can be applied. The construction of the basic bridge circuit is as shown in the figure 3.4. The bridge works like a standard basic bridge circuit with a pair of known and unknown impedance. The leg 1 and 2 in the ratio transformer are generated by sine wave generator, which decides the optimal voltages to drive leg 3 and 4. Leg 3 consists of known impedance which has fused-silica capacitor and a pseudo-resistor. Taps 1 and 2 in the transformer and the value of  $R_0$  and  $C_0$  will be selected by the microprocessor in the bridge and thus the voltage through the detector is minimized (null condition). This will allow to measure both the resistive and capacitive components of the unknown impedance independently. When the microprocessor is able to obtain this null condition, the unknown capacitance can be easily determined, since the ratio of the unknown capacitance ( $C_x$ ) to  $C_0$  is equal to the ratio of voltage on the Tap 1 to the voltage on Tap 2. Similarly, unknown resistance can be determined, as the ratio of  $R_x$  to  $R_0$  is equal to the ratio of the voltage on the Tap 2 to voltage on Tap 1.

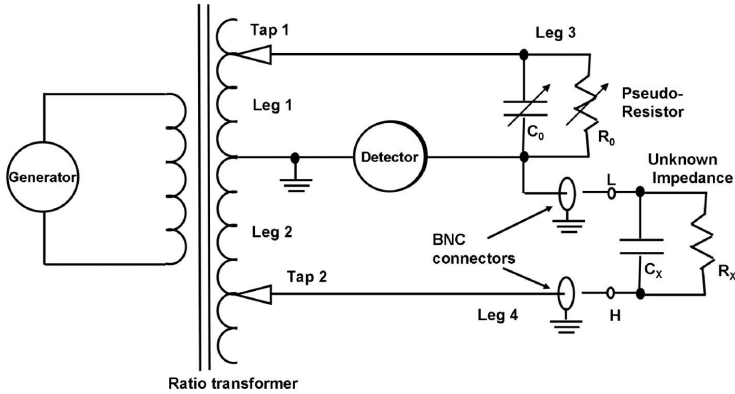


Figure 3.4: AH2700A basic bridge circuit.

A LabVIEW program for the dielectric measurement was developed with the help of Jürgen Lauer and Dr. Benedikt Klobes. The program enable computer to communicate

with the capacitance bridge and to control PPMS operations. Using this program one can measure the sample capacitance by varying the frequency keeping the temperature constant and vice versa (shown in figure 3.5). The temperature can be varied continuously or by step wise.

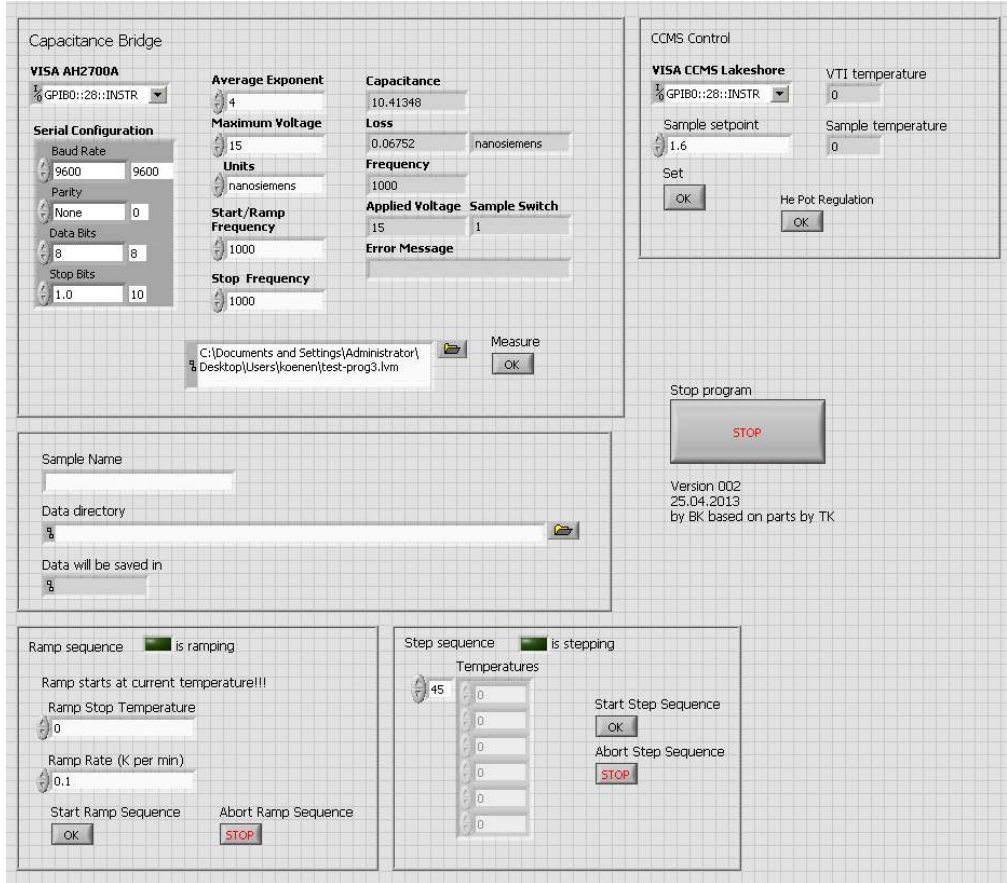


Figure 3.5: Developed LabView program to measure the dielectric contact.

### 3.3 Test measurements

Several trial experiment was performed on a well known and well characterized multiferroic material,  $\text{MnWO}_4$  in order to standardize results. The choice of this material as a standard sample for testing the setup is because of its field (H) dependent dielectric

properties and very sharp ferroelectric phase transition with relatively high value of dielectric response. Moreover it is a very good insulator. A thin disc of sample was polished down to  $27\text{ }\mu\text{m}$  ( $A = 5 \times 5\text{ mm}$ ) and made as a capacitor by applying silver paste on both the sides in a precise shape. The contacts were made on both the sides of the sample and the voltage was applied. The value of the capacitance of the parallel plate capacitor was recorded in the capacitance bridge. During the course of testing this new setup, it was discovered that in order to get the dielectric signal the applied voltage needs to be relatively high, more than 10 V (maximum limit of the instrument is 15 V) and the sample need to be as thin as possible, that is obvious from the equation 3.8. The noise to signal ratio can be reduced by using three probe method, instead of two probe, by making the third contact ground. Though the results obtained from the three probe method did not make much difference as the sample was displaying relatively high value of dielectric constants however, it helped during the low frequency measurement. In order to make the better electrical contact one can also use gold sputtering instead of silver paste.

**Multiferroic  $\text{MnWO}_4$ :**  $\text{MnWO}_4$  crystallizes in the monoclinic struture with the space group  $P2_1/c$ . This material exhibits three magnetic transitions, AF1, AF2 and AF3, upon cooling. At AF1(  $T_N \sim 7.6\text{ K}$ ) the structure is collinear and AF2 ( $7.8 < T_N < 12.6\text{ K}$ ), AF2 ( $12.6 < T_N < 13.5\text{ K}$ ) exhibits incommensurate magnetic structure followed by sinusoidal and noncollinear helical spin phase respectively. Ferroelectricity in this materials is induced by the AF2 phase with cycloidal component in which the inversion symmetry is broken by magnetic structure itself and induce the net polarization along the  $b$ -axis. Figure 3.6 shows the temperature dependence of the dielectric constant measured at zero field and at 1 T. The material exhibits ferroelectric transition at  $\sim 12.7\text{ K}$  (AF2) followed by a stepwise anomaly around  $7.5\text{ K}$  (AF1) upon cooling. With the application of magnetic field perpendiclr to  $b$ -axis, the ferroelectric transition shifted to low temperature region. The obtained results were comparable with the reports, e.g, [94], though those measurements were performed with  $H$  parallel to  $b$ -axis.

**Multiferroic  $\text{Fe}_3\text{O}_4$ :** Along with the building an in-house dielectric set up, another aim of the project was to use this setup to characterize the as grown single crystals for further microscopic measurements. One of the major interest of our research was to prove the ferroelectricity in classical magnetite by microscopic as well as by macroscopic measurement. At room temperature magnetite crystallizes inverse cubic spinel struture with the space group  $\text{Fd}\bar{3}m$  and followed by a metal-insulator transition at  $\sim 120\text{ K}$

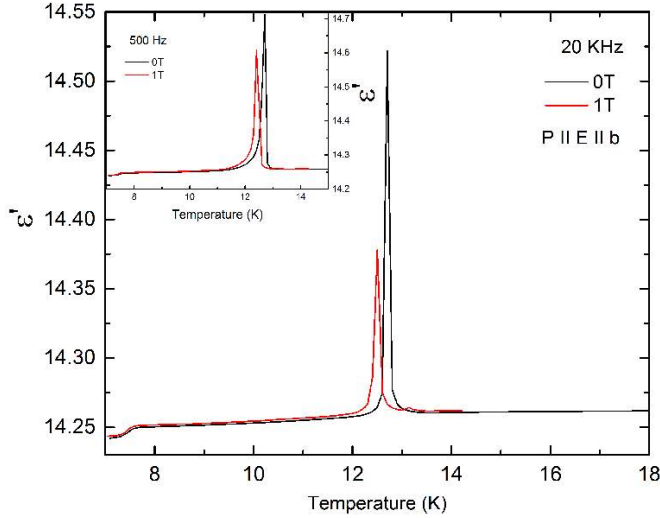


Figure 3.6: Temperature dependence of dielectric constant measured on  $\text{MnWO}_4$  along  $b$ -axis at 0 T and 1 T with the frequency of 20 kHz. Inset shows the measurement performed at 500 Hz.

upon cooling associated with the  $\text{Fe}^{3+}$  and  $\text{Fe}^{2+}$  charge ordering. Below this transition the symmetry of the crystal lowered to monoclinic  $Cc$ . Though CO based ferroelectricity in this material was proposed in early 2000 [95], the low temperature charge ordered structure was solved very recently and proved as polar [96]. During the course of building the set up, Loidl group has published the results of detailed dielectric spectroscopy measurement and proposed it as relaxor ferroelectric [reference [97] and figure 4.5]. As discussed earlier in this chapter the relaxor ferroelectrics are characterized by diffuse phase transitions: exhibits frequency dependence of dielectric constant as shown in figure 4.11. But the problem with the magnetite is it is a poor insulator. This is one of the reasons behind the long puzzling question of ferroelectricity in magnetite, stoichiometry also plays a major role. Figure 3.7 exhibits the dielectric measurements performed on magnetite. The contribution attributed by the Loidl-group to intrinsic relaxation consistent with relaxor behavior is not visible in the figure 3.7 - mainly due to lower frequency limit. Another reason could be that we have used silver electrode for our measurement. In this case the interface effect is larger compare to gold electrodes. The observed frequency dependent steps in  $\epsilon'$  is Maxwell-Wagner effect caused by spacial inhomogeneity. Moreover our capacitance bridge permits only a narrow range frequencies, 50 Hz - 20 kHz, which is not sufficient enough to characterize, particularly the dielectric properties of

magnetite. Therefore further measurements were performed in collaboration with Prof. Hemberger from Cologne university and the obtained results are shown in the figure 5.5(b).

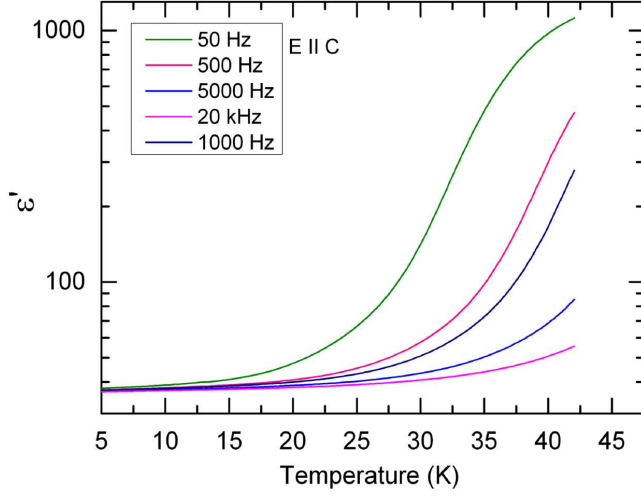


Figure 3.7: Temperature dependence of dielectric constant measured on  $\text{Fe}_3\text{O}_4$  along  $c$ -axis at 0 T at different frequencies.

## Chapter 4

Magnetite: crystal growth,  
macroscopic characterization and  
low temperature diffuse scattering  
studies

Multiferroic materials, consisting of both ferroelectric and ferromagnetic phases, have garnered an increasing scientific and technological interest due to the potentially large magnetoelectric coupling. For practical applications the magnetoelectric coupling must be large as well as active at room temperature. Proper ferroelectrics exhibit relatively weak coupling between the magnetism and ferroelectricity as they are induced by different ions. Among improper ferroelectrics spin-spiral based ferroelectricity has attracted considerable attention in the recent years however, its practical prospects is limited because of very low achievable polarization. A general approach to combine both large electric polarization and strong magnetoelectric coupling is based on the ferroelectricity originating from charge ordering [62] [see section 1.2.2] and the most likely candidate in this category is classical magnetite  $\text{Fe}_3\text{O}_4$ .

The 120 K Verwey transition ( $T_V$ ) in Magnetite ( $\text{Fe}_3\text{O}_4$ ) is the classical example of charge ordering [3]. The very complex low-temperature structure was unsolved despite decades of research, and there was even controversy about the existence of  $\text{Fe}^{2+}/\text{Fe}^{3+}$  charge ordering below  $T_V$  [98–100]. The controversy and the complex low temperature structure is discussed in the section 4.1.1. Being one of the first materials studied regarding the magnetoelectric (ME) effect [101] the existence of ferroelectricity in magnetite was unclear over the decades. Early studies have suggested the existence of a spontaneous polarization at temperatures below 4.2 K [102], and also, two recent calculations provide theoretical support for ferroelectricity due to charge order [67, 95]. More recent studies of real-time ferroelectric switching in magnetite epitaxial thin film seem to be consistent with this [103]. Only very recently the complex charge order structure has been solved and proved as polar [96]. The detailed history of ferroelectricity in magnetite is discussed in the section 4.1.2.

The Verwey transition in magnetite is highly sensitive to ideal metal-oxygen stoichiometry. Any slight deviation from 3:4 cation to anion ratio greatly alter the  $T_V$  from first order to second order [104, 105] and hence this can provide the justification for some of the discrepancy in numerous prior studies of this material. The difficulty associated with sufficient ambient oxygen fugacity control constitutes the main obstacle for the crystal growth of magnetite. The best way to obtain high-quality crystals is the direct synthesis in an appropriate  $\text{CO}/\text{CO}_2$  flow [106]. Our studies of use of appropriate ratios of  $\text{CO}/\text{CO}_2$  gas mixtures at high temperature on polycrystalline samples preparation, as well as the growth of high quality single crystals under the tailored growth conditions by floating zone method are presented in the section 4.2. Further, results of preliminary

characterization of Verwey transition by thermo remanent magnetisation and specific heat measurements are presented.

In a very recent comprehensive dielectric spectroscopy study of magnetite, Schrettle and co-workers proposed magnetite is not a normal ferroelectric [97], but rather a relaxor ferroelectric. However the state of microscopic experimental verification confirming the proposed relaxor ferroelectricity is still absent. In order to test the relaxor-hypothesis of Schrettle *et al*, we have performed a comprehensive diffuse scattering study focusing on the temperature well below the Verwey transition, the results of which are discussed in the section 4.3.

## 4.1 Magnetite

Magnetite ( $\text{Fe}_3\text{O}_4$ ) is the oldest magnetic mineral known to man kind (indeed the name magnetic comes from magnetite). It was discovered in the town of Magnesia, Greece, around 2000BC. It is one of the most abundant metal oxide and was used to magnetize the mariner compass. Because of its anomalously high Neel temperature (840K) and predicted half metallic ferromagnetic properties [107, 108], it is a promising candidate for the room temperature spintronics.

Magnetite crystallises in inverse spinel structure  $AB_2O_4$  with the space group of  $Fd\bar{3}m$  and the lattice constant  $a = 8.3960\text{\AA}$ . Its ionic formula can be written as  $\text{Fe}_A^{3+}[\text{Fe}^{2+}\text{Fe}^{3+}]_B\text{O}_4$ , where  $8\text{Fe}^{3+}$  or  $1/3$  of the total iron ions are located in the tetrahedra A site and  $16\text{Fe}$  ( $8\text{Fe}^{2+}$  and  $8\text{Fe}^{3+}$ ) or  $2/3$  of the total iron ions are located in the octahedral B site. The iron at B sites located at the center of the oxygen octahedra and these sites form a pyrochlore lattice, consisting of a network of corner sharing tetrahedra. The room temperature cubic structure of magnetite is shown in the figure 4.1. The delocalization between the neighbouring electrons in the octahedral B-site yields an average oxidation state of  $\text{Fe}^{2.5+}$  and makes magnetite a good metallic conductor at high temperature [109, 110]. Magnetite has a ferrimagnetic ordering, typical of neel's two-sublattice model, which implies that the moments of Fe ions in the A and B sub-lattices are aligned antiparallel to each other and parallel within the each sub lattice. The magnetization of the  $\text{Fe}^{3+}$  in both the sites cancel each other and the net magnetic moment arises only from the  $\text{Fe}^{2+}$  ions, which is  $4\mu_B$ .



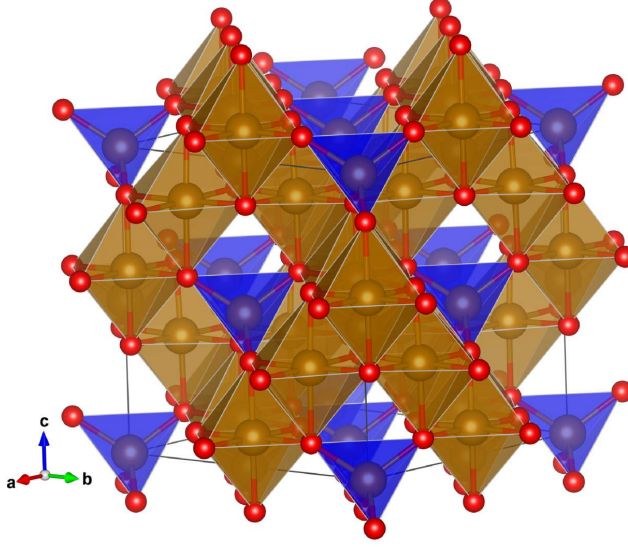


Figure 4.1: Room temperature structure of Magnetite

#### 4.1.1 Verwey transition and the complex charge ordering

Apart from the magnetic property magnetite shows a very prominent first order metal - insulator transition, where the resistivity drops by two orders of magnitude while heating above  $T_V \sim 120\text{K}$ . The temperature-dependence of the electrical conductivity is shown in the figure 4.2. Research on magnetite was triggered by the discovery of this classical transition ( $T_V$ ) by Verwey in 1939 [3]. According to Verwey, the high temperature conductivity ( $T > T_V$ ) is due to the continuous interchange of electrons between the  $\text{Fe}^{2+}$  and  $\text{Fe}^{3+}$  ions at the octahedral B-site through thermally activated fast electron hopping. Upon cooling below  $T_V$ , the electrons get localized and  $\text{Fe}^{2+}$  and  $\text{Fe}^{3+}$  ions on octahedral site orders periodically. The onset of charge localization at the respective iron ions reduces the conductivity. This simple model was very successful in giving a reasonable interpretation of the electrical resistivity measurements [3]. The model also says that at  $T_V$  along with the charge ordering the symmetry of the crystal reduces from cubic to orthorhombic, where  $\text{Fe}^{2+}$  and  $\text{Fe}^{3+}$  ions occupy alternate positions along the (001) planes on the octahedral iron sites. Verwey's charge order model satisfied the Anderson criterion for minimum inter-site electrostatic energy [111] that requires that each tetrahedral group of four B sites should contain two electrons (i.e.  $2\text{Fe}^{2+}$  and  $2\text{Fe}^{3+}$ ) analogous to the ice rules in frozen  $\text{H}_2\text{O}$ , thus leading to short range charge ordered

pattern. Moreover with the discovery of Verwey transition, Magnetite has become a classical example of charge ordering in transition-metal oxides.

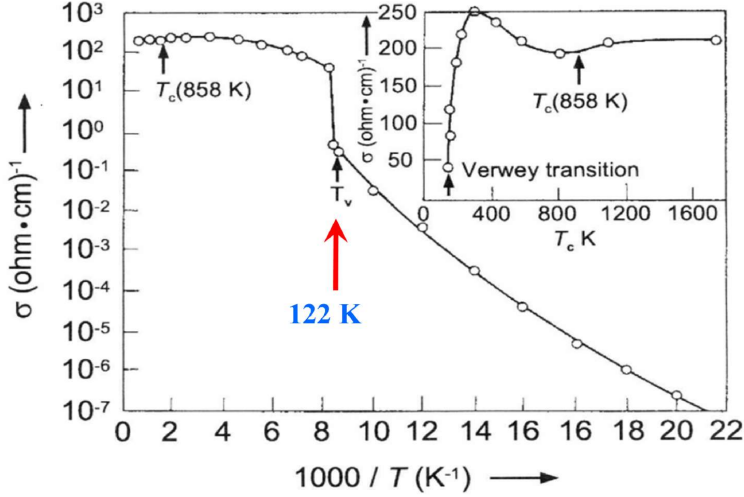


Figure 4.2: Temperature vs electrical conductivity of magnetite, taken from reference [112]

Ever since the Verwey's model was proposed, the origin and even the existence of charge ordering in magnetite has been a subject of discussion, as different experiments conducted to study the Verwey transition yielded seemingly contradictory. Although an early neutron experiment by W.C Hamilton supported the Verwey model [113], later the model was disproved by further studies [114], which showed that multiple-scattering effect flawed this experiment. Though the electron diffraction [115], mössbauer spectroscopy [116] and NMR studies [117] were able distinguish different kinds of ions, unable to support the charge ordered model proposed by Verwey. Further diffraction studies indicate the doubling of the cubic unit cell along the c-axis by the observation of the super structure reflection ( $h k l + 1/2$ ) and show the symmetry to be monoclinic Cc [118–120]. Even lower symmetry, triclinic P1, was indicated by magneto electric measurement in the low temperature phase [121]. One of the largest difficulty involved in solving structure by single crystal diffraction is caused by microtwinning at the Verwey transition. The first low temperature superstructure refinement by Iizumi et al [114] using neutron diffraction on a partially detwinned crystal proposed large atomic displacements of Fe and O atoms

in a  $a_c/\sqrt{2} \times a_c\sqrt{2} \times 2a_c$  crystallographic subcell with space group  $Cc$  (with an additional orthorhombic  $Pmca/Pmc2_1$  symmetry constraints). However this refinement, unable to significant evidence for a charge ordered arrangement, although some differences were found in the inequivalent B sites. Later structural evidence for charge ordering has been provided by Wright et al [122, 123] based on high-resolution neutron and synchrotron x-ray powder diffraction. However the CO pattern deduced by wright et al, is more complicated than the Verwey model and does not satisfy the Anderson criterion. In the assumed model, refinement of the  $P2/c$  subcell structure of the  $Cc$  unit cell with the  $Pmca$  symmetry constrains, the crystal structure shows  $a_c/\sqrt{2} \times a_c/\sqrt{2} \times 2a_c$  supercell with space group  $Cc$ . A bond valence sum analysis revealed four independent octahedral Fe site split into two groups, each with a charge of +2.4 and +2.6 and does not meet Anderson's condition of minimal electrostatic repulsion. Resonant x-ray diffraction studies by joly *et al* supported the monoclinic  $Cc$  structure with a twice larger unit cell and they have found a small charge disproportion, around  $\pm 0.023$  at octahedral site. Further studies by Garcia and co-workers [98, 99] using resonant x-ray scattering performed at the Fe K edge claimed the absence of charge ordering and explain the Verwey transition by structural changes due to the strong electron-phonon interaction. However, despite continuous efforts, conclusive low temperature structural model, charge ordered pattern or even the existence charge ordering has not been concluded until very recently because of the complexity of the low temperature structure. After the decades of research, a more reliable and most convincing crystal structure refinement was recently shown by Senn et al [96], via high- energy x-ray diffraction by screening through a number of micro-crystals to find the one which is least affected by multiple domains/twins. Their experimental results undoubtedly showed the low-temperature structure to be monoclinic  $Cc$  ( $\sqrt{2}a_c \times \sqrt{2}a_c \times 2a_c$ ), which is in agreement with the DFT electronic structure calculations by Yamauchi et al [67]. Although the  $Fe^{3+}/Fe^{2+}$  charge ordering and  $Fe^{2+}$  orbital ordering showed Verwey's hypothesis correct to a useful first approximation [3], the proposed model varies from the Verwey's original prediction of  $Fe^{2+} - Fe^{3+}$  charge-arrangement and explained by a "trimeron" charge -ordering model: It was shown that, in the crystal structure an additional shortening of  $Fe^{2+} - Fe^{3+}$  distances are due to delocalized extra down-spin electrons from an  $Fe^{2+}$  site onto two adjacent  $Fe^{3+}$  sites in the linear three-Fe-site units, called trimeron ( $Fe^{3+}-Fe^{2+}-Fe^{3+}$ ), running on B Sites.

### 4.1.2 History of ferroelectricity in Magnetite

Despite the controversies about the existence of charge ordering, magnetite has been proposed as one of the charge- order- based multiferroics. Indeed experimental indications of ferroelectric polarization [102, 124] and the anomalous dielectric properties were already reported in the early 1980's [125]. Even before that, magnetoelectric effect was measured below the Verwey transition and interpreted by a model with spontaneous polarization along the b-axis [101, 126]. Despite these experimental reports about ferroelectricity neither detailed ferroelectric properties and its mechanism, nor a clear proof of ferroelectricity were available. In 2006 Khomskii had proposed a theoretical model for charge order based ferroelectricity in magnetite by the co-existence of both site and bond centered charge ordering, which break the inversion symmetry and shows the net dipole moment [62, 95]. Besides the site-centered charge ordering, the distances between the charge ordered  $\text{Fe}_B^{2+}$  and  $\text{Fe}_B^{3+}$  sites are strongly modulated along the monoclinic b-direction in which the polarization is observed. In addition to alternation of  $\text{Fe}_B^{2+}$  and  $\text{Fe}_B^{3+}$  ions, there is an alternation of short and long Fe-Fe bonds and is supported by the low temperature structural refinement by Wright *et al* [123] where they observed the strong modulation between the two charge ordered Fe sites along the b-direction from 2.86 Å to 3.05 Å. Also his model, based on Wright *et al* [123], assuming the iron ions on the octahedrally coordinated site form a network of iron tetrahedra, proposed each tetrahedron to show 3:1 charge order arrangement (three  $\text{Fe}^{2+}$  and one  $\text{Fe}^{3+}$ ). However this model is in contrast to Anderson's criterion, where each tetrahedron has a 2:2 pattern. But the low temperature refinement by Wright *et al* was performed using a small sub cell  $a_c/\sqrt{2} \times a_c/\sqrt{2} \times 2a_c$  instead of the large  $a_c\sqrt{2} \times a_c\sqrt{2} \times 2a_c$   $Cc$  cell [114].

Subsequent to Khomskii's model, a theoretical calculation(DFT) done by Yamauchi *et al* proposed the ferroelectricity in magnetite to be induced by a noncentrosymmetric charge ordering with the polarization primarily being induced by the localised charged shifts [67]. The calculated P2/c structure as paraelectric shows 3:1 charge configuration, but cancels out the total polarization due to the structure shows inversion symmetry. Whereas the calculations done considering the  $Cc$  lattice symmetry is ferroelectrically active due to the lack of center of symmetry and shows mixed pattern of 3:1 and 2:2 charge ordered configuration (25 % of 2:2 and 75 % of 3:1 tetrahedra). In the figure below, the charge shift can be understood assuming the shift of  $\text{B12}'$  from  $\text{B14}'$  site and  $\text{B12}$

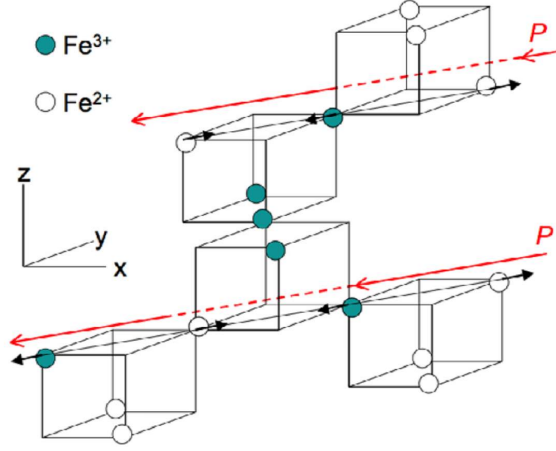


Figure 4.3: Schematic representation of the possible origin of ferroelectricity in magnetite, from ref [62]. Emphasized are the Fe chains in the B-site running along the  $[110]$  directions (in the cubic setting). In the  $xy$  chain, in addition to the alternation of  $\text{Fe}^{2+}$  and  $\text{Fe}^{3+}$ , there is also an alternation of short and long Fe-Fe bonds. The black arrow indicates the shift of the Fe ions and the red arrows indicate the resulting net polarization.

to B14 site of the cell. Each charge shift produces two 2:2 charge ordered tetrahedra, so as to form four 2:2 tetrahedra. The resulting charge ordered pattern lacks inversion symmetry and allows for ferroelectric polarization.

The polarization values calculated from DFT on a monoclinic  $C_c$  structure (from Berry phase model [127, 128],  $P_a = 4.41 \mu\text{C}/\text{cm}^2$ ,  $P_c = 4.12 \mu\text{C}/\text{cm}^2$ ) is fairly in good agreement with the recently reported experimental value of real-time ferroelectric switching in magnetite epitaxial thin film ( $P \sim 11 \mu\text{C}/\text{cm}^2$ ) [103] as well as with earlier reports on single crystals ( $P_a = 4.8 \mu\text{C}/\text{cm}^2$  and  $P_c = 1.5 \mu\text{C}/\text{cm}^2$ ) [102]. But the recent polarization measurement on a single crystals [97] showed  $P = 0.5 \mu\text{C}/\text{cm}^2$  which is very less compare to the value obtained by thin film. However, point-charge model calculation from Senn *et al* on recently solved low temperature charge ordered structure provided the polarization  $P_a = 0.118 \text{ C}/\text{cm}^2$  and  $P_c = 0.405 \text{ C}/\text{cm}^2$ , which is several order higher than the previous calculations. Their calculation also indicated that the more than 80% of the polarization in magnetite is induced by charge order and three site distortion. However, there was no microscopic experimental proof of supporting the CO ferroelectricity in magnetite. Even though for a ferroelectric material even if the

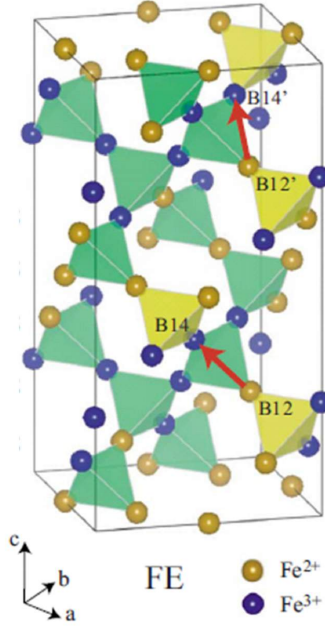


Figure 4.4: Ionic structure model of Fe octahedral sites in Cc cell.  $\text{Fe}^{2+}$  and  $\text{Fe}^{3+}$  ions are represented by orange and blue balls respectively. Yellow and green color planes indicates the 2:2 and 3:1 charge ordered pattern of  $\text{Fe}_4$  tetrahedra. Red arrow indicates the charge shift with will induce the electric dipole moment, taken from reference [67].

polar structure is established, the switching of this polar structure needs to be shown. Recently, Schrettle and co-workers proposed that magnetite is a relaxor ferroelectric below 40 K rather than a normal ferroelectric, based on their observation of strongly frequency dependent of dielectric properties and a continuous slowing down of its polar dynamics, dominated by tunnelling at low temperatures [97]. As shown in the figure 4.5, magnetite shows a broad peak in the real part of the dielectric permittivity as a function of temperature and this peak decreases in magnitude and is shift to higher temperature with increasing frequency. This is the typical behavior of relaxor ferroelectrics [129]. But compared to the dielectric properties of classical relaxor, e.g., figure 4.11 magnetite exhibits larger step like feature, which is of extrinsic origin. One of the reason could be the presence of residual conductivity in the ferroelectric phase of magnetite, which is very well visible in the P(E) curves shown in the figure 5.3.

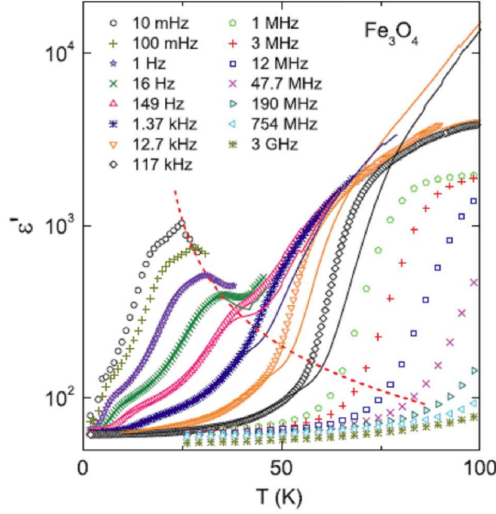


Figure 4.5: Temperature dependent of  $\epsilon''$  of magnetite for various frequencies taken from reference [97]. Symbols are with silver contact and dotted line indicates the measurements repeated with the gold contacts. The intrinsic features, indicated by the dashed line representing Curie-Weiss behavior, are better visible in the measurements done with gold contacts.

## 4.2 Synthesis and effect of non-stoichiometry on the Verwey transition

At the Verwey transition not only the resistivity jumps, but also many other physical properties show spectacular anomalies. Apparently all these anomalies are greatly influenced by the oxygen stoichiometry. Even a small departure from the 3:4 cation to anion ratio greatly alter the thermodynamic properties of the Verwey transition.  $T_V$  is maximum and first order for stoichiometric magnetite. Any deviation from this 3:4 stoichiometry will lower the transition and for  $\delta > 0.004$  the transition is of second or higher order, ( $\text{Fe}_{3(1-\delta)}\text{O}_3$ , where  $\delta$  is the cation deficiency) [104, 130]. The effects of nonstoichiometry on the thermodynamic properties is shown in figure 4.6. For the first order transition the remanence decreases sharply and discontinuously, where as for the second order transition remanence decreases continuously [figure 4.6 (b)]. Also above the Verwey transition the moments remains positive for the first order transition, but become negative for second order transition [130].

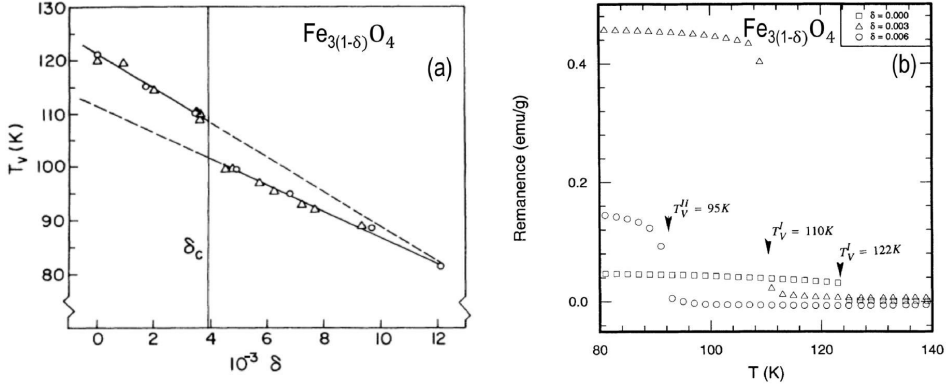


Figure 4.6: (a) Variation of Verwey phase transition with  $\delta$ , taken from reference [104]. (b) Thermoremanent magnetization measured by field cooling to 4.5 K at 10 kOe after heating the sample in zero applied field. Samples with  $\delta = 0.000$ , 0.003 and 0.0006 are denoted by squares, triangles and circles respectively, taken from reference [130]

### 4.2.1 High quality polycrystalline precursor synthesis for the crystal growth

An extreme care was taken to prepare the precursors for the single crystal growth. Samples which are not carefully prepared could have FeO and  $\text{Fe}_2\text{O}_3$  impurities. Polycrystalline precursors were prepared by using the hematite,  $\text{Fe}_2\text{O}_3$ , as a starting material. The materials were sintered in a tube furnace at  $1000^\circ\text{C}$ , for 24 hours in the presence of appropriate ratio of  $\text{CO}_2$  and  $\text{H}_2$  gas mixtures.  $\text{H}_2$  acts as a reducing agent [131], which converts  $\text{Fe}_2\text{O}_3$  to  $\text{Fe}_3\text{O}_4$  and  $\text{CO}_2$  acts as a oxidizing agent which prevents the further reduction of  $\text{Fe}_3\text{O}_4$  to FeO and Fe. Mixing these gases leads to a certain oxygen partial pressure, which determines the Fe-O phase and stoichiometry. Hence optimizing the ratios of these gas mixtures is very crucial to obtain the high quality  $\text{Fe}_3\text{O}_4$ . The flow rates of the gas mixtures were controlled by flow controllers. The stoichiometry of  $\text{Fe}_{3(1-\delta)}\text{O}_3$  depends on the oxygen partial pressure it is in equilibrium with. At any particular temperature the equilibrium between these components establishes a definite oxygen partial pressure. The furnace, flow controller and schematic diagram of the furnace is shown in the figure 4.7.

As-prepared precursors were characterised by x-ray diffraction. The diffraction patterns and the Rietveld refinements of two selected samples were shown in the figure 4.8. Structural refinement shows the pure phase of magnetite, which can be indexed by a cubic structure with the space group  $Fd-3m$  and the lattice constant  $a = 8.3997$ . After confirming the phase purity, polycrystalline samples then pressed in to pellet and the





Figure 4.7: A picture of the tube furnace used to synthesize the polycrystalline samples, flow controller and schematic diagram of the furnace respectively.

Verwey transition was characterized primarily by thermo-remnant magnetization and heat capacity measurements. The results for selected samples are shown in the figure 4.9. From the figures we could clearly see the effect of stoichiometry on the Verwey transition of magnetite.

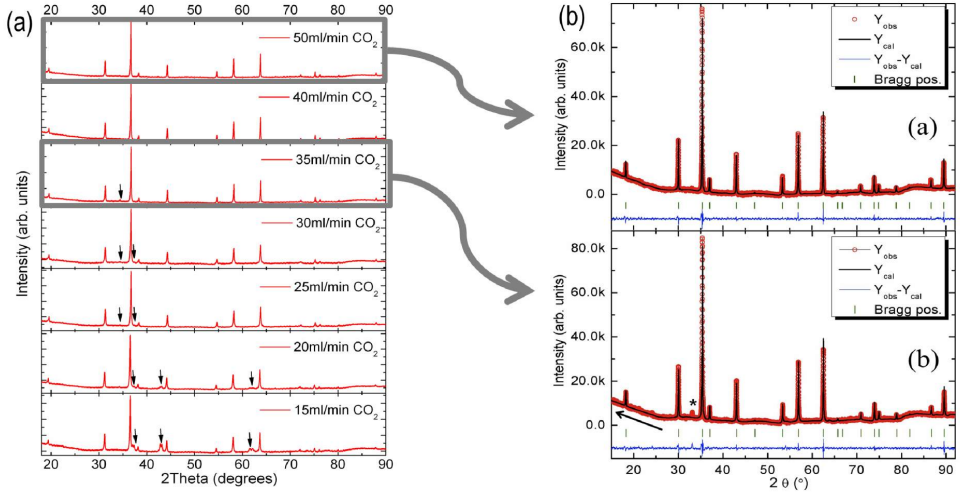


Figure 4.8: (a) Powder XRD patterns of polycrystalline  $\text{Fe}_3\text{O}_4$  synthesized with different flow rates of  $\text{CO}_2$  and fixed 50ml of 96%  $\text{Ar}/4\%\text{H}_2$  (arrows indicate impurity peaks). (b) Rietveld refinement of the powder XRD patterns of (a) pure sample and (b) sample with impurities ( $\text{Fe}_2\text{O}_3$  impurity peak is denoted by star).

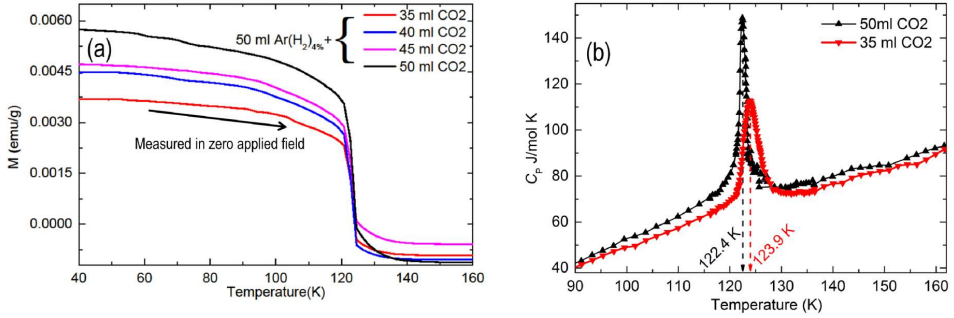


Figure 4.9: Characterizing the Verwey transition of Polycrystalline magnetite sample. (a) Change in the remanent moment obtained by field cooling to 40 K at 10 kOe. (b) Specific heat anomaly near the Verwey transition.

## 4.2.2 High quality single crystal growth

Single crystal growth trials were conducted after obtaining highly stoichiometric polycrystalline precursors by using the floating zone furnace as described in the chapter 2. During the growth instead of H<sub>2</sub>, carbon monoxide was used as a reducing agent because H<sub>2</sub> affects the nucleation by forming water. Highly stoichiometric crystals were obtained by fine tuning the gas mixtures of CO and CO<sub>2</sub>. For all the growth trials the rotation speed of the feed and seed rods were kept 18 and 14 rotation/min respectively and the growth rates were 1 mm/hour. The different growth conditions used during the single crystal growth is presented in the table 4.1. As-grown crystals were characterized by specific heat and thermoremanent magnetization measurements, shown in the figure 4.10 [only few selected measurements are shown]. As can be seen, crystals with a very sharp Verwey transition at a high temperature could be obtained, indicating highly stoichiometric and homogeneous Fe<sub>3</sub>O<sub>4</sub>.

Table 4.1: Crystal growth conditions

Growth	CO <sub>2</sub> (ml/min)	CO(ml/min)	Growth length	T <sub>V</sub> (K)	FeO impurity peak
1	99.4	16.17	42	121.6	Present (huge)
2	99.4	12	38.5	121.69 (top) 122 (bottom)	Very small peak Absent
3	99.4	12.2	30.5	120.5	Present
4	99.4	11.2	30	119.25	Present
5	99.4	11.8	28.2	118.77	Present
6	99.4	11.6	42.3	119.31	Present
7	99.4	10.24	22.6	120.5	Present
8	99.4	12	73.5	121.4	Present (huge)
9	96	4	29	123.8	Absent
10	96	4.5	48	122.86	Absent
11	96	4.25	32	123	Absent

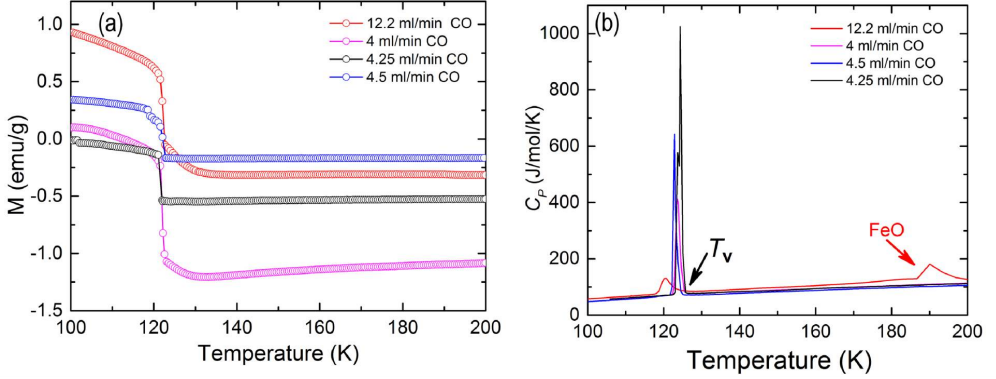


Figure 4.10: Characterizing the Verwey transition of magnetite single crystal. (a) Remanent magnetization of different crystals grown by 100 ml of CO<sub>2</sub> and different flow rates of CO measured while heating, after cooling the sample to 4.5 K in 10 kOe. (b) Specific heat ( $C_p$ ) of different samples grown by 100 ml of CO<sub>2</sub> and different flow rates of CO. The anomaly in  $C_p$  corresponds to Verwey transition ( $T_V$ ). The anomaly around 190 K is the magnetic order-disorder transition in the Fe-rich wüstite [132].

### 4.3 Diffuse scattering study on relaxor ferroelectric Magnetite

Relaxor ferroelectrics relate to normal ferroelectrics similar as spin glasses relate to magnetically ordered phases. The relaxor behaviour normally originates from the compositionally induced disorder or frustration. This behavior was mostly observed and extensively studied in disordered  $\text{ABO}_3$  perovskite ferroelectrics [133, 134]. However, the origin of the relaxor phase has been a subject of intense research over decades. At high temperature the non-polar paraelectric (PE) phase is similar to a PE phase of normal ferroelectric. As temperature decreases they transform into the relaxor state, in which polar clusters of nanometer size with randomly oriented direction of dipole moments appear. The formation of these nano-sized polar clusters below a characteristic temperature, known as Burns's temperature ( $T_d$ ) gives rise to a characteristic dielectric dispersion [135, 136], strongly resembling ac-susceptibility on spin glasses, see figure 4.11. Near the Burns temperature these polar nano regions (PNR) are mobile and as temperature is lowered, their dynamics slow down and at a low enough temperature the PNR in the canonical relaxors become frozen into a nonergodic state. Freezing of these PNR or the dipodynamics is associated with the wide peak in the temperature

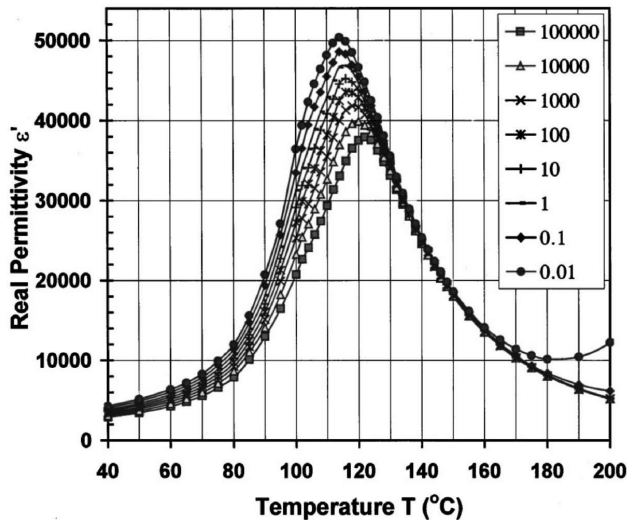


Figure 4.11: Temperature dependencies of the real part of dielectric permittivity of 0.75PMN-0.25PT ceramics, taken from reference [129]

dependence of the dielectric constant with the characteristic dispersion and in contrast to normal ferroelectric it is highly diffuse and frequency dependent. Because of this “diffuseness” of the dielectric properties, relaxors are often called as “ferroelectric with diffuse phase transition”, even though an actual phase transition to a ferroelectric phase does not occur. Since these polar nano domains are randomly oriented the zero field polarization is significantly smaller. Temperature dependence of  $P(E)$  curves are shown in figure 4.12. It is possible to induce the large polarization in relaxor ferroelectrics with a sufficiently large electric field [137].

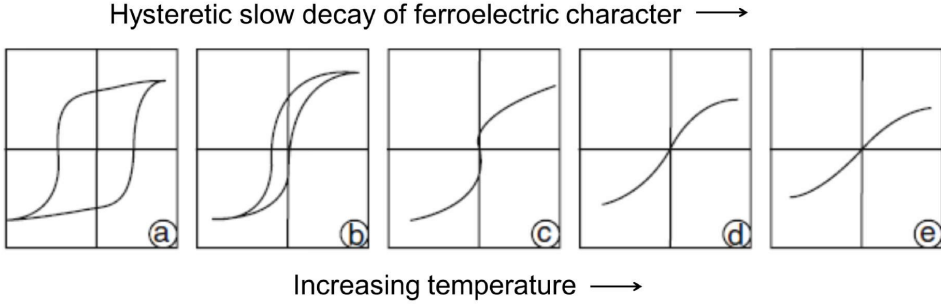


Figure 4.12: Dielectric hysteresis in PMN as a function of temperature, taken from reference [133]

Although there is still much debate about the cause and mechanism and even the exact nature of these PNRs and hence the relaxor behaviour, typical relaxors like potassium lithium tantalate (KLT) and lead magnesium niobate (PMN) show specific diffuse scattering at low temperature associated with PNR [138]. It has been observed that in these materials instead of long range ferroelectric order, the formation of diffuse scattering near the Burns temperature where the local polar regions are formed and the intensity of the diffuse scattering increases with decreasing temperature below  $T_d$ . Several models have been proposed to describe the diffuse scattering in terms of phase-shifted polar nonoregions and the static stain fields [139–141]. However, all these models relate diffuse scattering to the presence of polar correlations in the relaxor ferroelectric material. If magnetite is indeed a relaxor ferroelectric, it is expected that such diffuse scattering as observed in classical relaxors can be seen. In the past few decades there have been a number of diffuse scattering studies on magnetite [142–145]. However they almost exclusively focus on the strong diffuse scattering at and above  $T_v$ , which is not connected

to possible relaxor dynamics at much lower temperature.

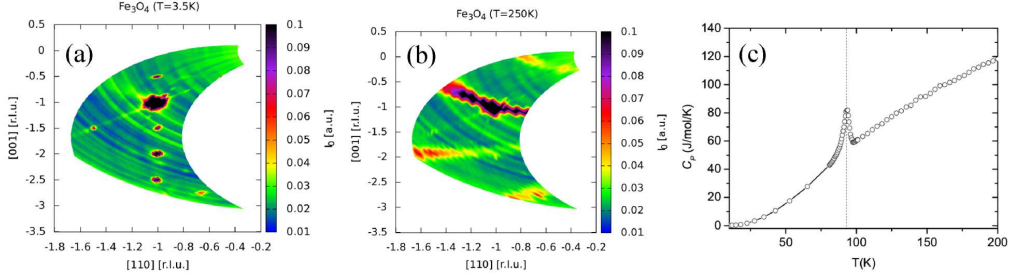


Figure 4.13: Temperature dependent of Diffuse neutron scattering in (hhl) plane at (a) 4.2 K and (b) 250 K, (c) Specific heat,  $C_P$  of the crystal measured at zero magnetic field ( $T_V = 93$  K).

In order to test the relaxor-hypothesis of Schrettle et al, we therefore performed a comprehensive study of diffuse scattering focusing on low  $T \ll T_V$ . The figure 4.13 is the neutron diffuse scattering in magnetite measured by mapping the reciprocal space in (hhl) plane of magnetite single crystal at the instrument DNS [section 2.6.4] MLZ. In panel (b) the observed diffuse scattering, well above the Verwey transition is well understood by polaron model by Yamada. A polaron is a quasiparticle, which describes the interaction between a charge carrier (electrons or holes) and atoms in a solid material. This diffuse scattering was interpreted in terms of cooperative motion of molecular polarons [145] and these polarons describes the properties of valence fluctuations in magnetite above Verwey transition. At sufficiently high temperatures, the polarons are randomly distributed and are fluctuating independently by hopping through the crystals and each of these molecular polaron induces instantaneous strain field around it. Based on this model it was interpreted that the observed diffuse scattering should be Huang scattering [that is, the scattering induced by the an impurity introduced into an elastic medium], due to the strain field induced by independent molecular polarons. However our measurement in the very low temperature, below 4 K, suggested that a type of diffuse scattering unique to low temperature is present. The new result is shown in the fig 4.13 (a) and the figures are plotted in the cubic setting of the high temperature structure. This diffuse scattering is in the [111] direction and perpendicular to scattering at 250 K and also the intensity is very weak compared to the one at high temperature.

This result from first neutron measurement to study the relaxor ferroelectricity was

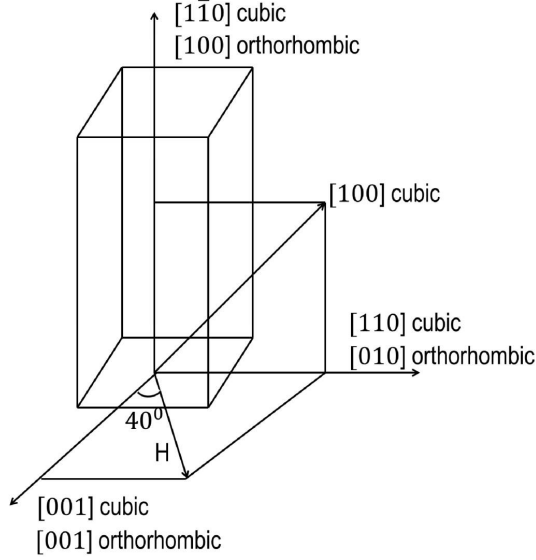


Figure 4.14: Experimental arrangement to reduce the number of domains. Crystal was tilted  $40^\circ$  to the  $c$ -axis. Incident and diffracted beams were in the plane of  $[001]$  and the orientation of the field  $H$ , as shown, removed the  $[a,b]$  twinning.

obtained on the non-stoichiometric sample. The Verwey transition temperature is 93 K and, accordingly, of second order as well visible in fig 4.13(c). We performed an analogous measurement at DNS on a very high quality sample with  $T_V = 123$  K to check whether the previously observed diffuse scattering is sample specific or a real intrinsic property. Even after repeating the measurement we have observed the same diffuse scattering, although it is weaker 4.15 (a) [indicated by the white arrow]. However the observed extremely weak diffuse scattering could be because of the sample size as in the previous measurement the measured sample was with 10 grams and in the second measurement the sample size was 200 mg. Though there was large difference in the sample size we were able to reproduce the result, which confirmed the intrinsic properties of the crystal. To exclude any magnetic contribution, and to test the contribution from lattice part, we have performed a diffuse scattering experiment on a (much smaller) higher quality crystal with  $T_V = 123$  K by high energy X-rays at 6-ID-D (APS). Since magnetite has 24 structural domains in the low temperature monoclinic  $Cc$  structure, the crystal was cooled under the magnetic field of 1 T along a cubic  $[001]$ - direction. With magnetic field cooling through  $T_V$  the number of domains will be reduced due to the magnetoelastic coupling, makes it low temperature  $c$ -axis [146]. We also tried to remove the  $[a,b]$  twinning by orienting the crystal  $40^\circ$  to the

c-axis[shown in figure 4.14] and cooled system under the magnetic field [113]. Because the diffuse scattering is very close to strong reflections, lead pieces were used to mask them. However despite increasing the dynamic range and very long (1 hour) exposures we did not observe any diffuse scattering related to relaxor ferroelectricity (figure 4.15(b)).

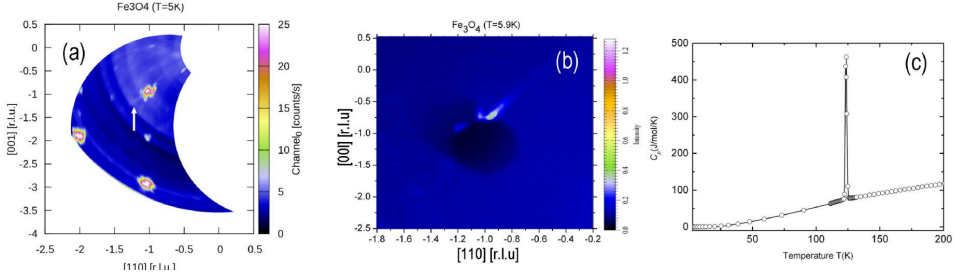


Figure 4.15: (a) Neutron Diffuse neutron scattering in(hhl) plane at 5 K (b) Diffuse scattering by high energy X-rays in (hhl) plane at 6 K. (c) Specific heat,  $C_p$  of the crystal measured at zero magnetic field ( $T_V=123$  K).

## 4.4 Discussion

One of the reasons for the large discrepancies in the results of various experiments on magnetite is due to the effect of nonstoichiometry. This is very clear from our macroscopic measurements performed on polycrystalline as well as on the single crystals. Therefore extreme care was taken to prepare the single crystals of magnetite and as grown high quality crystals were used for further scattering experiment. Compared to the report [130] (figure 4.6(b)), our samples did not show much variations in  $T_V$ , but there is a comparative difference in the moment above the  $T_V$  for different samples. The clear evidence for the first order transitions were obtained by specific heat measurements, which exhibits very sharp anomaly near the Verwey transition. Even the presence of FeO impurity with the increased carbon monoxide was also evidenced from specific heat measurement.

In order to study the proposed relaxor ferroelectricity diffuse neutron as well as high energy x-ray scattering experiments were conducted at the instrument DNS at MLZ and at the beam line 6-ID-D, APS, respectively. Although we have observed an extremely weak diffuse scattering at very low temperature by neutron diffraction studies which however, was absent in high energy x-ray studies. Based on all these obtained results we have to conclude that the observed diffuse scattering is magnetic in origin and therefore



not related to relaxor ferroelectric.

However, the lack of diffuse scattering in the ferroelectric phase leads us to the question of whether the magnetite is a relaxor ferroelectric or not. If it is a relaxor, then in what context? Considering the proposed charge-order based ferroelectricity, should it be expected to behave like a classical perovskite relaxor with classical ferroelectric mechanism?. As our present microscopic study is unable to prove/disprove the proposed relaxor ferroelectricity, the question is still outstanding. Although there were few reports on macroscopic indications of ferroelectricity (relaxor or not), as well as recently proposed relaxor ferroelectric, the most direct proof of ferroelectricity would be by switching of polar structure by electric field. The next chapter presents the state-of-the-art technique used the study the ferroelectricity and obtained results.

## Chapter 5

Time resolved experiment to test the ferroelectricity by switching the polar structure of magnetite

## 5.1 Introduction

Magnetite, beside being the oldest known magnetic material and the first transition metal oxide to show a metal-insulator transition, it is also known as the classical example of charge ordering. The complex charge ordering below  $T_V$  and controversial experimental reports were already discussed in the chapter 4 [section 4.2.1]. The difficulty of understanding the Verwey transition has been aggravated by variations in sample stoichiometry [section 4.3] and the presence of micro-twinning of domains, strong absorption, multiple scattering etc were greatly hindering the investigation of single crystals by diffraction studies. It took more than 70 years to define the exact charge ordered pattern as well as its crystal structure below the Verwey transition [96]. Although the magnetite was proposed as a charge-order based ferroelectric, microscopic experimental proof was lacking [section 4.2.2]. If proven, magnetite would be the first example of ferroelectricity from charge ordering.

The definition of ferroelectricity implies the possibility of switching between two stable states of apposite polarization with application of electric field. Although the recently solved charge ordered structure is polar [96], the unambiguous proof of intrinsic ferroelectricity requires demonstrating the switching of this polar structure. So far the macroscopic indications of polarization switching is not clear. This is mainly due to the presence of residual conductivity, which inflates the  $P(E)$  loop. Recently proposed relaxor ferroelectric properties of magnetite indicated that polarization switching can be observed only at high frequencies. However there was no microscopic experimental proof to support this. This was one of the main aims of this thesis work to give conclusive microscopic proof of ferroelectricity in magnetite by switching the polar structure with the applied electric field. The experimental techniques and the obtained results are discussed in this chapter

Figure 5.1 explains the pictorial representation of the method implemented in the work. As an example, consider the structure of a prototypical ferroelectric material,  $\text{BaTiO}_3$ , with the opposite ferroelectric polarization is as shown in the figure 5.1 (The ferroelectric distortion in the figure is exaggerated). Ferroelectricity in this material is induced by the up or down displacement of the Ti atom and these two opposite structures are related by inversion through the inversion center " $I$ ". In a conventional experiment, measuring the intensity,  $I(hkl)$ , of one of the structures is equivalent to measuring the intensity,  $I(\overline{h}\overline{k}\overline{l})$  of the oppositely polarized structure by inverting "q" [5.1(a)]. The pair of reflections

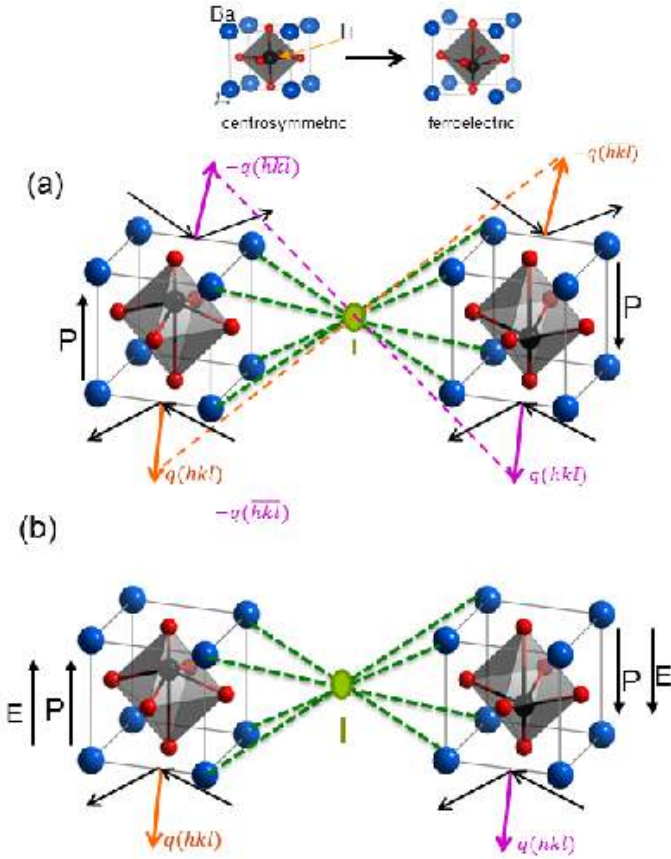


Figure 5.1: Pictorial representation of the method implemented in the work using classical BaTiO<sub>3</sub> with exaggerated ferroelectric distortion. (a) Explains the situation in conventional method of measuring intensity of the Friedel pairs,  $I(hkl)$  and  $I(\bar{h}\bar{k}\bar{l})$ , by inverting the "q". (b) Explains the situation where intensity of the Friedel pairs were measured by keeping the same "q" while switching the structure by an electric field, similar to the case of conventional method.

$(hkl)$  and  $(\bar{h}\bar{k}\bar{l})$  are called a Friedel mate. Analogous to the case (a), figure 5.1(b) explains the situation with the applied electric field, where both the intensities,  $I(hkl)$  and  $I(\bar{h}\bar{k}\bar{l})$  were measured by keeping the same "q" while switching the structure, which is equivalent to going over to the Friedel mate (inverting q) without switching the structure.

The intensity of the Bragg peaks is proportional to  $|F(hkl)|^2$  and the structure factor

$F(hkl)$  can be written as

$$F(hkl) = \sum_j f_j e^{2\pi i(hx_j + ky_j + lz_j)} \quad (5.1)$$

In the case of an incident x-ray energy, that is far from any absorption edge, all the atomic electrons scatter like free electrons with an atomic form factor,

$$f_j(\vec{Q}) = f_j^0(\vec{Q}) = \int_{atom\ j} \rho_j(r) e^{i\vec{Q} \cdot \vec{r}} d^3r \quad (5.2)$$

Where  $f_j^0(\vec{Q})$  is the Thomson scattering contribution and the atomic scattering density  $\rho_j$  is proportional to the electron density and thus real. When the atomic scattering density function,  $\rho_j(r)$ , is real, the intensity of the Friedel pairs are equal and can be written as

$$I_{hkl} \propto \left| \int_{atom\ j} \rho(r) e^{i\vec{Q} \cdot \vec{r}} dr \right|^2 = \left| \int_{atom\ j} \rho(r) e^{-i\vec{Q} \cdot \vec{r}} dr \right|^2 \quad (5.3)$$

This equation is known as Friedel's law, which holds for both centrosymmetric and non-centrosymmetric structure. When we use an incident x-ray energies near an absorption edge for atom  $j$ , the atomic scattering factor is no longer real and becomes a complex number. In this case the total scattering factor contribution from atom  $j$ ,  $f_j(\vec{Q})$ , takes the form

$$f(\vec{Q}, E) = f^0(\vec{Q}) + f'(E) + if''(E) \quad (5.4)$$

Where  $f'$  and  $f''$  are the real and imaginary parts of the dispersion correction which arises because of the anomalous scattering (see figure 5.2). The energy dependence of  $f''$  is proportional to the absorption cross section. Above the atomic absorption edges, the imaginary term  $f''$  becomes appreciable and the Friedel pairs show unequal intensities if the structure is non-centrosymmetric. The Friedel's law doesn't hold in this case. It is also important to note that, in contrast to normal (Thomson) scattering the anomalous scattering is independent of scattering angle and hence the effect is more pronounced at high scattering angle where the normal scattering is weak. The contrast between Friedel pairs can be significantly enhanced by choosing a wavelength at which significant absorption occurs corresponding to a large imaginary part of the structure factor. As mentioned before, in many cases,  $f''$  becomes significant close to one of the absorption edge energies of a major anomalous scatterer of the target material. In the present study we have used energies above the Fe-K absorption edge. Anomalous scattering factor of Fe

as a function of X-ray wavelength is shown in figure 5.2.

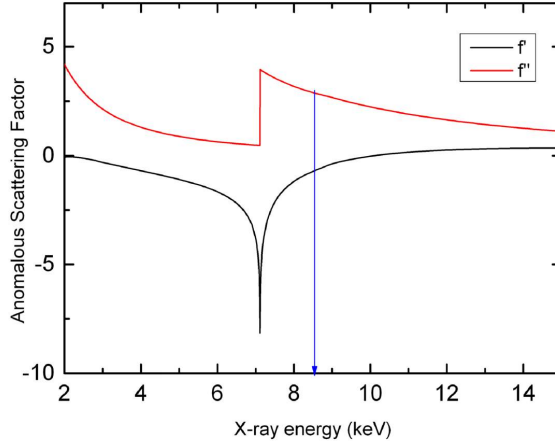


Figure 5.2: Variation of  $f'$  and  $f''$  for Fe with X-ray energies, near iron K-absorption edge.

This method has been successfully implemented on a multiferroic  $\text{DyMn}_2\text{O}_5$  system to study the polar atomic displacement [147]. In this system, the experiment was performed at the energies above the Mn  $K$ -edge ( $E = 6.550$  eV) and dc-voltage of  $\pm 900$  V was applied along opposite polarities in the sequence +, -, -, + on the Bragg reflection (3 6 2). The measured intensities of the Friedel pairs,  $I(hkl)$  and  $I(\bar{h}\bar{k}\bar{l})$ , showed intensity difference of  $\sim 6\%$ . In that case the polarization is retained at least at a time-scale of minutes so that dc electric field can be used. However the major obstacle for the low temperature ferroelectric phase of magnetite is the presence of intrinsic high conductivity as shown in figure 5.3 [97]. It is well known that the hysteresis measurements are based on the integration of the total current flowing through the ferroelectric capacitor. The real capacitor has two current components, one is the displacive current  $\delta D/\delta t$ , which gives the hysteresis loops in case of ferroelectrics and the other one is conducting current  $J_l$  which inflates the loop [148, 149]. In the figure 5.3 the presence of leakage current greatly altered the hysteresis loop in the sense that the loop is inflated, for e.g., the large hysteresis at 30 K. At least half convincing hysteresis loops with indications of saturation were observed only at very low temperature and at high frequency. In this case unambiguous proof of ferroelectricity can not be obtained by macroscopic measurements. Because of the presence of residual conductivity in the ferroelectric phase as well as

due to the relaxor properties (exhibits frequency dependence of dielectric properties) of magnetite the experiment needed to be time resolved. Time-resolved in-situ electric field measurements so far have been done only on piezoelectric crystals to study the microscopic and macroscopic strains induced by the applied periodic high voltage with fast switching between opposite polarities [150]. For the first time we have implemented this technique to study the ferroelectric properties in a proposed relaxor ferroelectric.

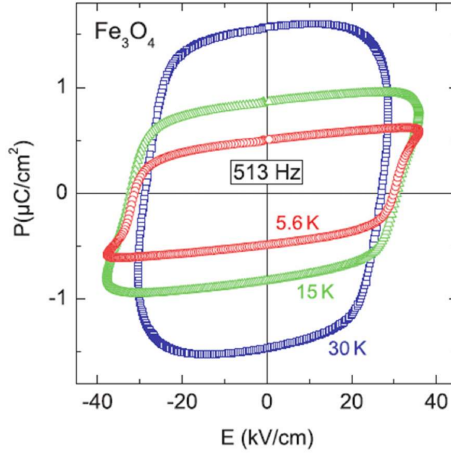


Figure 5.3: Ferroelectric polarization  $P$  as a function of external electric field  $E$  at 513 Hz, taken from reference [97]

## 5.2 Preliminary characterization

### 5.2.1 Simulation

The number of domains in the system is defined by symmetries. The room temperature cubic phase ( $\text{Fd}\bar{3}\text{m}$ ) of magnetite can have 48 equivalent choices (related to each other by rotation, reflection or inversion) of the vectors  $a, b$ , and  $c$ . They are all equivalent to each other. The crystal symmetry is reduced in the low temperature phase and transformed into monoclinic  $Cc$ . Monoclinic structure has only two equivalent orientations. The system can have 12 ferroelectric domains and each of them has two sets of inversion domains. Therefore totally there are 24 domains in the low temperature phase and they are related to each other by twinning matrices. Prior to applying for the beam

time we have done preliminary structure factor calculations using equation 5.1, taking into account of anomalous scattering, based on the recently refined polar structure of magnetite [96]. We have taken into account the presence of 24 CO domains during our calculation assuming equal population, and considering switching of all the domains. The ratio of the intensities can be calculated by  $R = \frac{|F(\bar{h}kl)|^2}{|F(hkl)|^2}$  and the difference between the Friedel mates should be  $(1-R) \times 100$ . While hunting for reflections with optimal absolute as well as relative Friedel-mate intensity differences we could find couple of good reflections which showed intensity difference by several percents.

### 5.2.2 Sample characterization

It is also important to note that the starting point of any ferroelectric measurement is by making ferroelectric material as a device, most typically a capacitor. Thus the whole measurement involves the contribution from interfaces, electrodes and wires. Sometimes the electrical response from these (artifact) can affect measurement of quantities from which the intrinsic properties of the material of interest are usually decreased. In this case it is very useful to look at the switching current by different methods. PUND (positive up negative down) method is one of the most extensively used technique to distinguish the ferroelectric switching from artifact. In this method, first the material will be polarized in a definite direction by applying the voltage pulse. Then the pulse 1 will be applied to switch the polarization in the positive up direction and this switching can be observed as an increased current which is associated with the ferroelectric polarization. Later pulse 2 will be applied after a certain delay time in the same direction as pulse 1 (figure 5.4). In this case switching will not be seen since the polarization is already switched. In the same way pulse 3 and 4 will be applied, but in the negative down direction. When the polarization state of the sample is reversed the corresponding charge also will be switched. Figure 5.4 display the results of PUND measurement performed on magnetite at the Cologne university in collaboration with Prof. Hemberger's group. The measurement was performed at different voltages as well as at different frequencies because the artifacts are generally highly frequency dependence. In order to see the switched ferroelectric polarization, currents from the pulse 2 is subtracted from pulse 1, (similarly pulse 4 from 3) and difference in the currents between the different polarization states are plotted in the figure 5.4(b). As can be seen in the figure the polarization switching was pronounced



with the increased voltage.

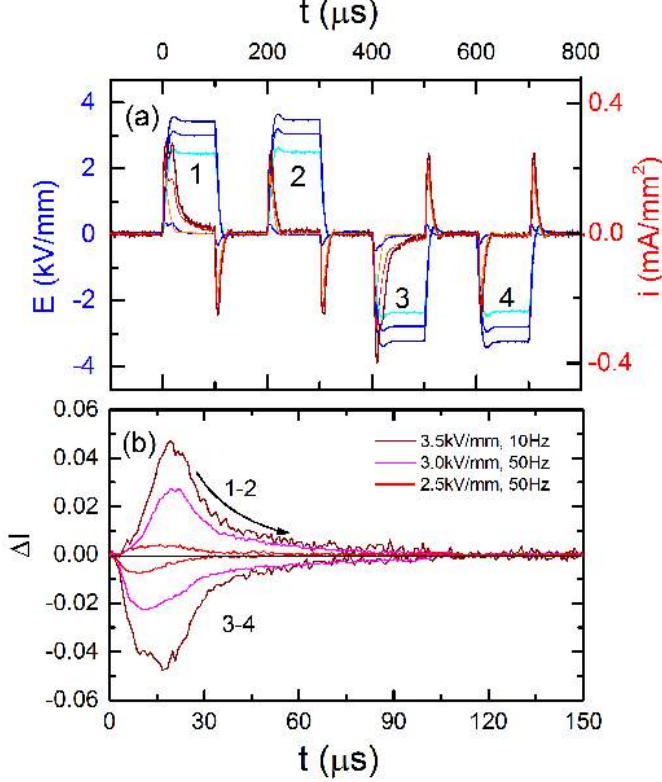


Figure 5.4: (a) Result of PUND measurement on a high quality magnetite single crystal at  $T = 5$  K. The delay time between pulses was  $100\mu$  s. (b) Difference between the measured currents for the 1st and 2nd, as well as 3rd and 4th pulses.

As discussed in section 1.1.2, the sample quality plays a major role in concluding the results, as Verwey transition is highly sensitive to the ideal metal-oxygen stoichiometry. For this reason a very high quality single crystal was chosen ( $T_V \sim 122.8$  K) for the measurement and characterized by macroscopic measurements. Figure 5.5 shows the heat capacity measurement performed at the instrument PPMS and dielectric measurement with an extended frequency range (compared to the 50 Hz to 20 kHz possible in Juelich, see figure 3.3) performed in collaboration with Prof. Hemberger's group from Cologne university. In the figure 5.5 (b) we have extracted the data from ref [97] (represented by full lines) and plotted along with our experimental data (represented by symbols) to

show, how the sample quality reflects in the results of ferroelectric measurements. By comparing the results we have concluded that quality of our sample, in terms of dielectric behavior is similar to the sample used by Schrettle for their measurements.

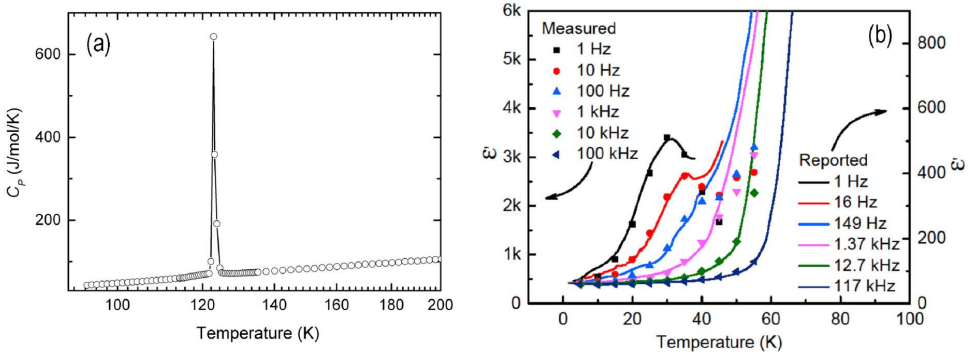


Figure 5.5: (a) Temperature dependent of the heat capacity of magnetite with  $T_V = 122.8$  K (b)  $\epsilon'(T)$  of magnetite measured at different frequencies and plotted together with the reported data, taken from ref [97], which confirmed high quality of the sample.

## 5.3 Experiment

After confirming the quality of the crystal a thin slab from the sample was cut along the (001) direction, polished down to a thickness of  $\sim 150 \mu\text{m}$  using sand paper and sputtered with gold of 100 nm thickness on both sides, by masking the edges of the crystal to avoid any short circuit during the experiment. The choice of gold over silver electrode was because gold has excellent corrosion resistance. But silver can tarnish very easily when exposed to the atmosphere which can be an effective insulator [151]. Moreover the work function of gold is higher than silver. Time resolved experiment was performed at the hard x-ray beam line P09, PETRA III. The experimental set up is shown in the figure 5.6.

We began our experiment by mounting the crystal on a alumina sample holder for electrical insulation. Although alumina is a good thermal conductor, during the experiment we observed that the sample temperature was much higher than we expected. With the available standard closed-cycle cryostat one could reach the base temperature of  $\sim 4$  K, but during our measurement the sample thermometer was displaying  $\sim 7 - 8$  K

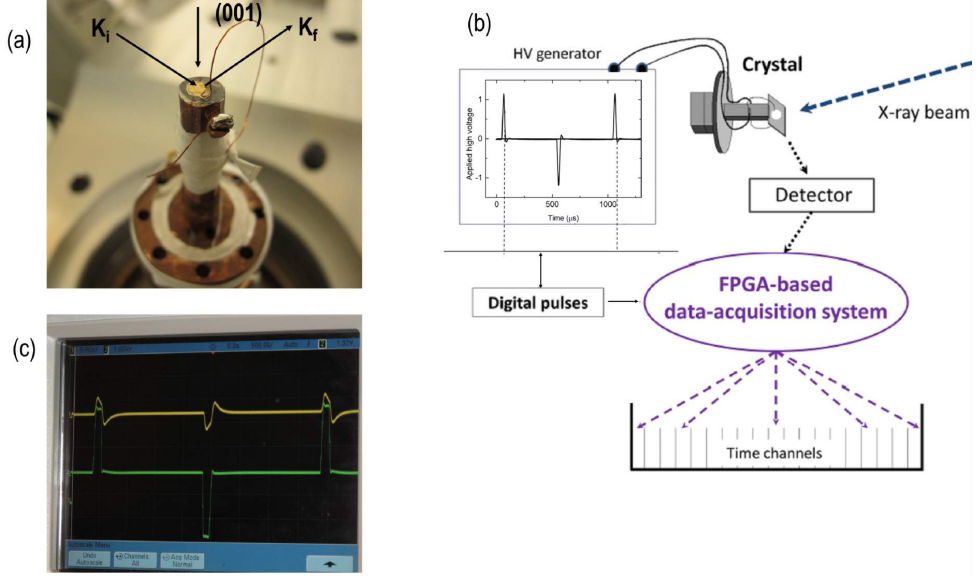


Figure 5.6: (a) Magnetite crystal sputtered with gold and mounted on the copper sample holder. (b) Flow chart of the novel data acquisition system, taken from reference [150]. High voltage (HV) electronics (left upper corner) generates the HV along with the digital pulses synchronized with the change in the HV polarities. The analog HV is directly delivered to the crystal. The digital signals, the current movement status of the diffractometer axes and the signals from the scintillating counter are processed by the field programmable gate array board (FPGA). (c) one of the many shapes of voltage pulses tried during the experiment (green color pulses are voltage and yellow color is current).

without the electric field and more than 10 K with the electric field. Along with the sample holder, there was also contribution from copper wiring made inside the chamber to apply the electric field; however, the effect of which was unavoidable. Considering the results of macroscopic polarization [figure 5.3], attaining as low temperature as possible was very crucial for the experiment to observe the intrinsic ferroelectric behavior. Hence, to overcome with the temperature issue, eventually we mounted the sample directly on the cold finger and made the electrical connections as shown in the figure 5.6 (a). One cable was directly connected on the top of the crystal and the other cable was grounded. And these two cables from the sample were connected to the periodic high voltage supply. The flow chart of the novel experimental setup developed by our collaborators at the university of Siegen at a different beamline for studies of piezoelectricity is shown in Fig 5.6. The crystal is subjected to x-rays and at the same time the periodic high voltage

is applied to the crystal. The diffracted photons coming out of the point detector were redistributed between 10000 time channels synchronized with the above state of the applied electric field. In this way each time channel probes the state of a crystal at a specific time delay after the beginning of a high voltage cycle. After adapting the setup to the P09, we had the time-resolution of at least several 100 Hz that is necessary for switching to occur, according to the macroscopic measurement (figures 5.3 and 5.4)

The experiment was challenging with a lot of technical issues. One of the necessary condition for the measurement was the presence of low temperature. As can be seen in figure 5.3 only the curve at 5.6 K shows indications of saturation at high field that is expected for intrinsic polarization switching [figure 5.3]. However, the presence residual conductivity at low temperature phase was hindering us to apply long voltage pulses by developing the heat load on the sample. Not only the voltage, but also the effect of beam heating, inductive current component and the switching current effecting the system to stay at low temperature. As the temperature increases sample becomes more conducting and leaky, as a result the extra charges from the sample coming back to the circuit and high voltage supply use to trip off. After several attempts we could optimize the system with the long dead time between the two voltage pulses, as shown in the figure 5.6(c). Apart from these technical issues another challenge was to choose a right reflection for the measurement. Though our preliminary structure factor calculation gave significant contrast between the Friedel pairs, not all the reflections could be reached at the Fe K-edge because of the rotation limit of the diffractometer. The rotation was severely restricted by the presence of the cryostat. The calculations showed that the relative difference between the intensities were high primarily for weak reflections. Considering the time constrains, due to the limited period of beam time, it was rather difficult to choose very weak reflection because it takes relatively longer time to collect the data with sufficient good statistics. With the above mentioned issues, and after testing the several structural reflections finally we have chosen the reflection (2 -2 10) for the continuation of the measurement.

As we had problem in attaining the low temperature (below 5 K) using a Displex closed cycle cryostat in the first beam time, to resolve the temperature issue we have used a cryostat with a lower base temperature of 1.7 K employing Joule-Thomson cooling in the second beam time. However the decision to use this cryostat turned out to be a mistake, because the thermal decoupling associated with the Joule-Thomson stage implied that the heat-load from the resistive heating of the sample could not be overcome, and

consequently the reachable temperatures were even higher than in the first beam time.

## 5.4 Results and discussion

For the reflection (2 -2 10) the calculated intensity difference was  $\sim 3\%$  considering that all 24 monoclinic domains are involved in the ferroelectric switching (assuming the presence of all 24 domains and of equal weight). This was even half of the intensity difference calculated by Azimonte *etal* on  $\text{DyMn}_2\text{O}_5$  which was around 6% for the reflection (3 6 2). Figure 5.7 shows the rocking curve measured during the experiment for the reflection (2 -2 10). The rocking is  $\sim 50$ -100 times broader than a rocking curve observed from a good single crystal for e.g., quartz [152].

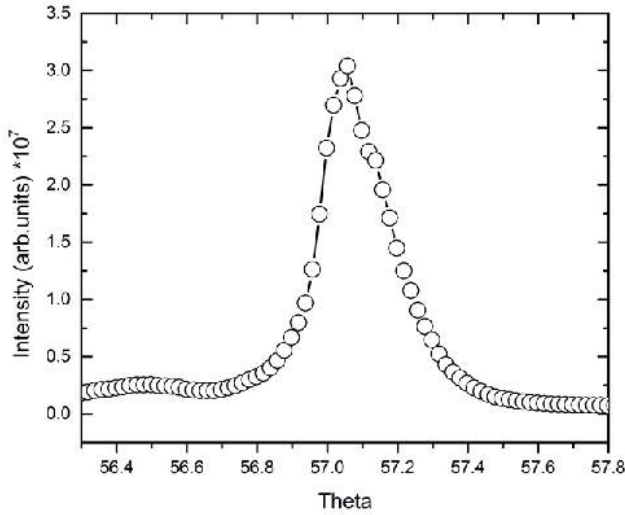


Figure 5.7: Theta vs intensity scan for the structural reflection (2 -2 10)

We have started our experiment by applying triangular waveform voltage (450 V), which is commonly used to measure the polarization, with the frequency of 500 Hz. The results of which is shown in figure 5.8. Since the intensities of the Bragg reflections were relatively weak and the resulting signals from point detector will be distributed to the different time channels, it required a long counting time ( $\sim 10$  hours) at each Bragg reflections to collect data with appropriate statistics. After spending one night to collect

the data with good statistics we realized that the voltage was not sufficient to switch the structure.

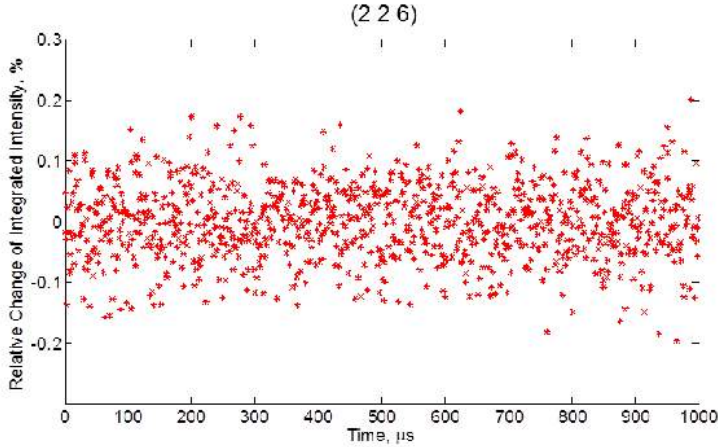


Figure 5.8: Absence of intensity change of the reflection (2 2 6)

Hence we had to spend ample time on experimenting with different voltages, shapes, frequencies as well as on the dead time between the two apposite voltage pulses. We also had to test the cable ad hoc because the applying voltage was exceeding what the cable was rated for. After several attempts, finally we were able to optimize the system with very short voltage pulses with zero voltage in between with the time day of  $\sim 400\mu\text{s}$ . The obtained result is shown in the figure 5.9. In order to obtain the significant contrast between the Friedel pairs, we have chosen a energy which is well above the Fe K-absorption edge of a anomalous scattering i.e.,  $E = 8.550 \text{ keV}$  and applied ac voltage pulses up to  $1 \text{ kV}/150\mu\text{m}$  with the frequency  $1\text{kHz}$ , prior to observing switching effect. Although it is possible to get significant contrast closer to the absorption edge, using the energies well above the absorption edge helps to stay well outside of the area affected by eg., EXAFS etc.

With the theoretical predictions and results from macroscopic measurements we expected relative large difference in the intensity between the Friedel pairs. From the Berry phase approach [67], the predicted polarization value was  $P_c = 4.12 \mu\text{C} / \text{cm}^2$  and from the point charge model [96] it is  $40.5 \text{ Ccm}^2$ , which is quite large compare to other improper multiferroics also compared to the macroscopic measurement which was  $0.5 \mu\text{C}/\text{cm}^2$ . Our preliminary structure factor calculations gave us  $\sim 3\%$  percent intensity

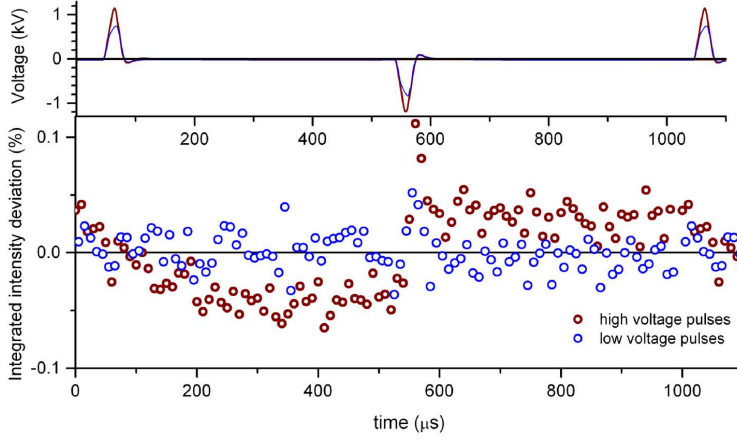


Figure 5.9: The change in the intensity of Bragg reflection (2-2 10) observed by an application of periodic high (1kV) and low (700V) voltage pulses with fast switches between opposite polarities. In order to avoid the heating effect on the sample, zero voltage was maintained between the single period, which included two 10 $\mu$ s switching pulses.

difference considering switching of all the ferroelectric domains. But the observed intensity difference was only 0.1% which is almost 30 times smaller than our calculation. This large difference in calculated and experimental values likely due to the following two reasons. Firstly the presence of high temperature: the whole measurement was performed at  $\sim 11$  K. Even after optimising to short voltage pulses, Joule-heating prevented us from reaching lower temperatures. It is very clear from the macroscopic measurements that the presence of residual conductivity at elevated temperatures greatly suppress the switchable ferroelectric polarization. For example in our PUND measurements performed at two different temperatures 2K and 5K, (though on different samples) we can see huge differences in the switching currents associated with the ferroelectric polarization between the two temperatures. Hence the observed low intensity difference could be due to the increased ohmic conductivity with temperature which partially obscured the switching. An ideal solution would be to stay at low temperature is the use of flow cryostat. However this is not possible with the high voltage because it will lead to breakthrough. The second possible reason could be that our calculations was done assuming that the polarities of all domains are switched, whereas with the electric field applied only those domains with direction of the polarization close to the direction of the applied voltage should be expected to switch. Other reasons like statistical character of switching such as how stable

the switching is and other conditions for e.g., domain size etc are could also contribute.

## 5.5 Conclusions

Electronic ferroelectricity from charge ordering was a long standing puzzle in magnetite. Though there has been reports on theoretical calculations supporting the improper ferroelectricity in magnetite due to charge ordering, the microscopic experimental proof was lacking. In order obtain the conclusive proof of ferroelectricity in magnetite, we have performed time resolved x-ray diffraction experiment in ac-electric field and tested if the alternating polarities of the field are able to switch steadily between the polar structures related by inversion symmetry. Though we were unable to test the several reflections within the limited period of beam time, the switching of the structural reflection (2 -2 10) with the intensity difference of 0.1% contributed significantly in providing microscopic proof of ferroic behaviour in magnetite. Though unambiguous proof requires testing several reflections within the available structure model, with the obtained result we can conclude that magnetite not only the oldest magnetic material known to mankind and the first material exhibiting the classical charge ordering transition, but also a first multiferroic material found on earth. Another significant contribution of this work was, a new method was developed at the beam line, which will be useful contribution to the beam line as well as to the users. Also, for the first time, time resolved in-situ experiment was implemented in proving the ferroelectricity in any material. But, as discussed in earlier chapter, for any practical applications materials should exhibit strong coupling and large polarization at room temperature. However, magnetite exhibit ferroelectric properties at low temperature, moreover the sample is not a good insulator. Nevertheless, the firm microscopic proof of intrinsic ferroelectric switching in  $\text{Fe}_3\text{O}_4$  is important as it provides a clear proof of principle that the "ferroelectricity from charge ordering" mechanism actually works, which should be relevant for other materials.





## Chapter 6

Growth, characterization and  
neutron polarization analysis on  
 $\text{SrFeO}_{3-\delta}$  single crystal

## 6.1 Introduction

Materials exhibiting colossal magnetoresistance effect (CMR) can potentially be used in building better disk drives read heads. The CMR effect was first discovered by [29, 153] and has been extensively studied in hole doped manganese based perovskite oxides [for details see section 1.2.1]. CMR effect arises due to the strong mutual coupling of spin, charge and lattice degrees of freedom [154–157]. Among all the materials which show CMR effect, only few materials show coexistence of charge ordering and ferromagnetism and the system  $\text{PrCa}_{1-x}\text{Mn}_x\text{O}_{3-\delta}$  is very noticeable in this category. Another category of materials with similar magnetic properties are oxygen-deficient perovskite strontium ferrite ( $\text{SrFeO}_3$ ).

Stoichiometric cubic perovskite  $\text{SrFeO}_3$  in which iron is present in the highly unusual +4 oxidation ( $\text{Fe}^{4+}$ ) state is isoelectronic with the  $\text{Mn}^{3+}$  ion of manganite system: both ions have the same  $3d^4$  configuration with three electrons in the  $t_{2g}$  level and one electron in the  $e_g$  level of the crystal field and both exhibit CMR effects [15, 158]. However in contrast to manganites, where the  $\text{Mn}^{3+}$  ion is responsible for Jahn-Teller effect,  $\text{SrFeO}_3$  does not show any evidence of Jahn-Teller effect and retains its cubic structure down to 4 K [159, 160]. Moreover, it is a metallic conductor and an antiferromagnet with  $T_N \sim 130$  K and also exhibits helical magnetic spin structure with propagation vector parallel to the [111] direction [15, 41]. The differences in the properties of  $\text{Fe}^{4+}$  when compared to  $\text{Mn}^{3+}$  are due to the presence of strong covalency between the  $\text{Fe}^{4+}$  - oxygen bonding. This is in agreement with the chemical trend – electronegativity increases from left to right in a transition metal series. The larger covalency leads to the larger width of the conduction bands which are formed by the strongly hybridised iron  $e_g$  and oxygen  $2p_\sigma$  orbitals and a large fraction of the charge transport is by the oxygen holes. The absence of Jahn-Teller distortion can be explained by increased itinerancy of the  $e_g$  electrons.

The crystal structure of  $\text{SrFeO}_3$  is shown the figure 6.1.  $\text{SrFeO}_3$  has a cubic perovskite structure with lattice constant  $a = 3.851 \text{ \AA}$  and space group  $Pm\bar{3}m$  (# 221). The structure consists of an ideal corner sharing octahedra with oxygen ions as a link between them. Non-stoichiometric  $\text{SrFeO}_{3-\delta}$  exhibits a rich variety of phase diagrams in the range of  $\delta$  from 0 - 0.25. With the decreasing oxygen concentration, the entire physical

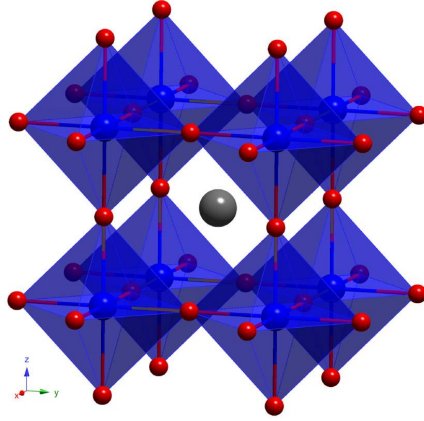


Figure 6.1: Crystal structure of  $\text{SrFeO}_3$ . The  $\text{Sr}^{2+}$  ion is in the center of the unit cell. Spheres of blue and red denote the iron and oxygen ions respectively.

and chemical properties will change in the broad temperature range, partial pressure of oxygen and also with the magnetic field. Extensive research on this compound reported that the oxygen vacancy ordering will affect the crystal structure and  $\text{SrFeO}_{3-\delta}$  shows one or mixture of two of the four different phases (which are mentioned in the following lines) in the composition range from  $0 < \delta < 0.5$  [161, 162]. The oxygen-deficient end member  $\text{SrFeO}_{2.5}$  (C,  $\delta = 0.5$  or  $\text{Sr}_2\text{Fe}_2\text{O}_5$ , Fe valence 3+) shows brownmillerite structure (*Ibm2* [163] or *Icmm* [161]) and the other end member  $\text{SrFeO}_3$  has cubic perovskite structure. The other two intermediate compositions,  $\text{SrFeO}_{2.875}$  (T,  $\delta = 0.125$  or  $\text{Sr}_8\text{Fe}_8\text{O}_{23}$ , Fe valence 3+ and 4+) and  $\text{SrFeO}_{2.75}$  (O,  $\delta = 0.25$  or  $\text{Sr}_4\text{Fe}_4\text{O}_{11}$ , Fe valence 3+ and 4+), are present in tetragonal (*I4/mmm*, # 139) and orthorhombic (*Cmmm*, # 65) phases respectively [161]. For all other intermediate  $\delta$  the composition is a mixture of the two nearest ideal phases. Because of the presence of phase mixtures in oxygen deficient  $\text{SrFeO}_3$  it is not an easy task to investigate its physical properties as it is not very straight-forward to deduce which property is due to which phase. The phase diagram of co-existence of different phases vs temperatures is shown in the figure 6.3.

Decreasing oxygen concentration, apparently leading to increased anion vacancy concentration, decreases the Neel temperature from 134 K (for  $\delta = 0$ ) to 70 K (for  $\delta = 0.15$ ) and also the electrical conductivity changes from metallic to semiconducting with increasing  $\delta$  [158, 160]. The metallic behavior of the  $\text{SrFeO}_3$  is due to the presence of itinerant  $e_g$  electrons in a broad  $\sigma^*$  band formed between the iron  $e_g$  and oxygen  $2p_\sigma$

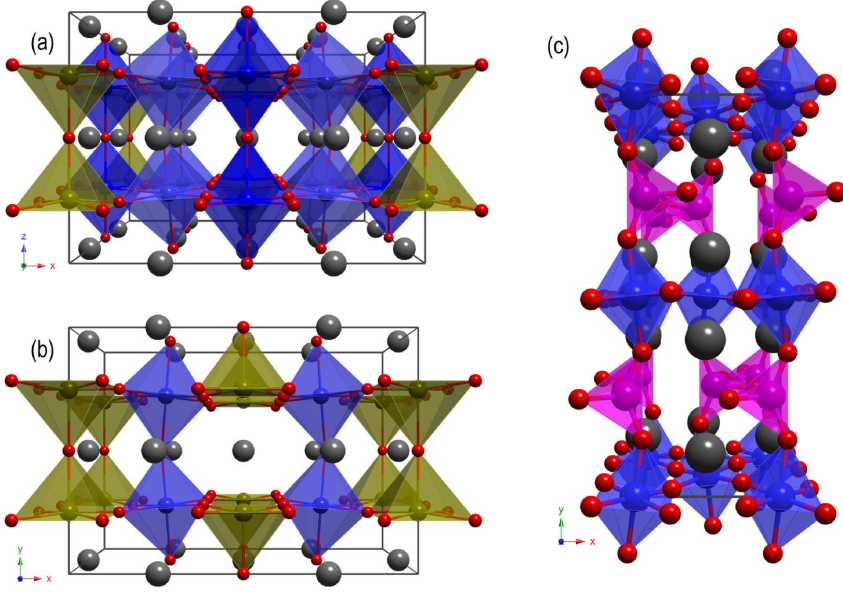


Figure 6.2: (a) Tetragonal structure of  $\text{Sr}_3\text{Fe}_8\text{O}_{23}$ , (b) orthorhombic structure of  $\text{Sr}_4\text{Fe}_4\text{O}_{11}$ , (c) brownmillerite structure of  $\text{Sr}_2\text{Fe}_2\text{O}_5$ . Spheres of gray and red denote the strontium and oxygen ions respectively.

bands. The presence of two separate valence states of ion,  $\text{Fe}^{3+}$  and  $\text{Fe}^{4+}$ , is responsible for such a change in the electrical properties.

Magnetic susceptibility measurements on different non-stoichiometric crystals of  $\text{SrFeO}_{3-\delta}$  are shown in figure 6.4. The figure shows different Neel temperatures for samples of different stoichiometry. The summary of temperatures corresponding to different anomalies is shown in the table 6.1. Stoichiometric  $\text{SrFeO}_{3-\delta}$  ( $\delta = 0$ ) shows an anomaly at 130 K, which corresponds to the onset of helical magnetic ordering and also shows a small cusp of susceptibility at 55 K. Mössbauer experiments performed by Lebon et al [15] showed that the  $\delta = 0$  compound contains only  $\text{Fe}^{4+}$  at all temperatures, which excludes any change in the valence state of the iron ion and suggests that the transition at 55 K is originating from the rearrangement of  $\text{Fe}^{4+}$  moments. In the  $\delta = 0.05$  and  $\delta = 0.15$  compounds, the anomaly at 130 K corresponds to the presence of residual C-phase and the sharp transition around 70 K in all the compositions are associated with the antiferromagnetic ordering of the T-phase. In the lowest oxygen content sample ( $\delta = 0.23$ ), the G-type antiferromagnetic ordering of  $\text{Fe}^{3+}$

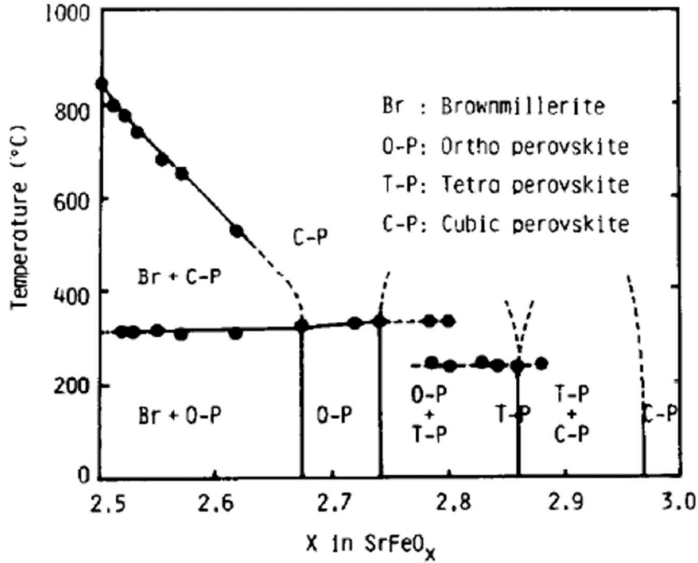


Figure 6.3: Pseudobinary phase diagram representing the single phase and coexistence of more phases of  $\text{SrFeO}_{3-\delta}$  as a function of temperature, taken from reference [162]

takes place at around 230 K and the anomaly which occurs at around 50 K corresponds to magnetically disordered  $\text{Fe}^{4+}$  [158]. The microscopic origin of anomalies which are observed at around 115 K, which is indicated by an arrow in figure 6.4, is still unknown.

In addition to all these interesting magnetic properties, non-stoichiometric  $\text{SrFeO}_{3-\delta}$  also display different types of magnetoresistance phenomena depending on the presence of different magnetic phases [158]. Figure 6.5 shows resistivity measurements on different non-stoichiometric crystals of  $\text{SrFeO}_{3-\delta}$ . The temperatures corresponding to different anomalies are presented in the table 6.1. As can be seen in the figure 6.5, the cubic phase is metallic and shows large negative MR ( $\sim -25\%$ ) in a narrow temperature region around 55 K, which is obviously related to the 55 K anomaly that is observed in magnetic susceptibility measurement. The behaviour of the  $\rho(T)$  curve of the compound  $\delta = 0.05$  can be explained by the existence of both C and T phases in the composition. Further decrease in the oxygen concentration, i.e. the system with  $\delta = 0.15$ , will lead to semiconducting behaviour and shows negative giant magnetoresistance ( $\sim -90\%$ ) near 70 K. The sudden increase in the resistivity near 70 K by an order of magnitude is associated with the charge ordering of  $\text{Fe}^{3+}$  and  $\text{Fe}^{4+}$  ions and is confirmed by the

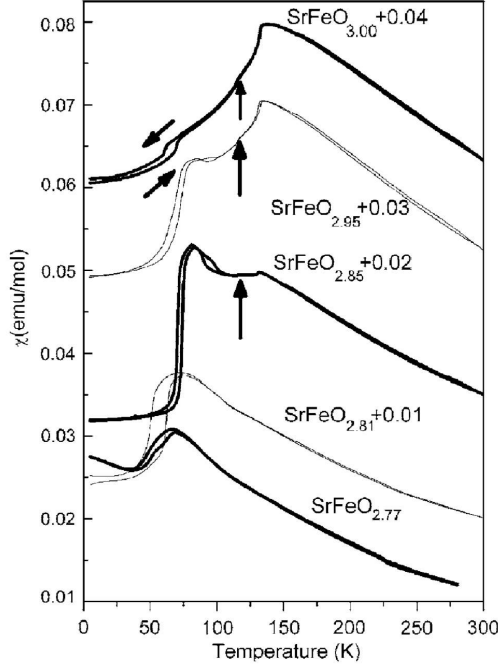


Figure 6.4: Magnetic susceptibility measurement: measured in both cooling and heating with 1 T magnetic field, taken from reference [158].

analysis of Mössbauer spectra [15]. The material becomes completely insulating and exhibits pronounced positive MR effect at around 50 K upon further decreasing oxygen concentration.

However, despite all the extensive research on understanding the crystal structure and physical properties in these oxygen deficient  $\text{SrFeO}_3$ , only few attempts were made to study the magnetic properties and the spin structure microscopically [164, 165]. Furthermore, the arrangement of the valences in the charge-ordered system ( $\delta = 0.15$ ) is not known. When we started our project spin structures of only two systems,  $\text{SrFeO}_3$  and  $\text{SrFeO}_{2.99}$ , were known. The difficulty in diffraction studies are due to the coexistence of different oxygen vacancy ordered phases and the corresponding superposition of different diffraction patterns in these mixed phases. Recently, in 2012, detailed neutron studies on different stoichiometric  $\text{SrFeO}_{3-\delta}$  were reported by Reehuis and coworkers [165]. Their

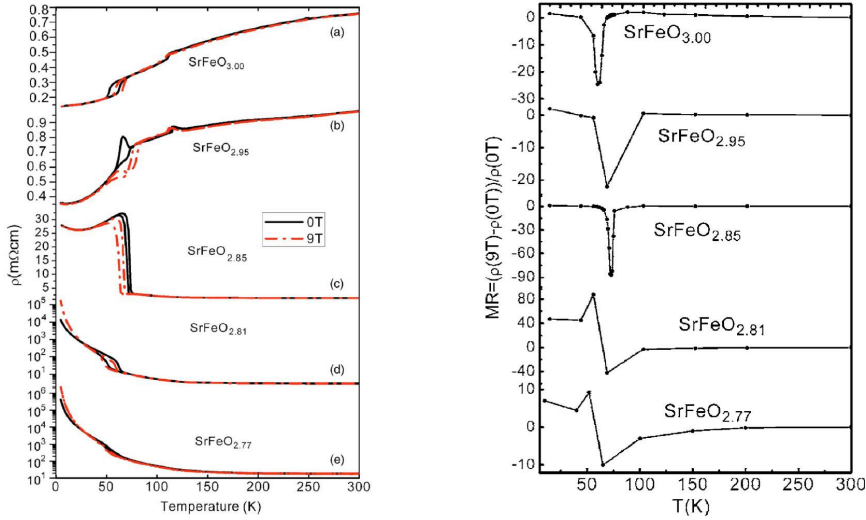


Figure 6.5: (a) Resistivity measurement: Black and red lines correspond to heating and cooling runs at zero field and 9 T field respectively. (b) Plot of MR vs temperature at 9 T field, taken from reference [158].

studies revealed 7 different magnetic structures in the range of  $\delta$  from 0 to 0.23. In this chapter we present the growth of two non stoichiometric crystals, studies of the crystal and magnetic structures and physical properties of these crystals. In order to study the spin structure and its orientation we have performed neutron polarization analysis. The obtained results are discussed in section 6.5.

## 6.2 Synthesis and single crystal growth

Polycrystalline materials were prepared by the conventional solid state method (see Section 2.1.1). Stoichiometric amount of precursors,  $\text{SrCO}_3$  and  $\text{Fe}_2\text{O}_3$ , were ball-milled for about one hour, transferred into an alumina crucible and calcined in a tube furnace in the presence of oxygen flow for about 24 hours at 1100 °C. Phase formation of the resulting materials was checked by powder x-ray diffraction. After phase confirmation, the feed and seed rods were prepared for the crystal growth by filling the powder into a rubber tube. Further, the tube was sealed, pressed in a hydrostatic press and again sintered in an alumina boat in flowing oxygen at 1300 °C. The crystals were grown by optical floating



Table 6.1: Summary of the temperatures of different anomalies observed in the magnetic susceptibility ( $T_m$ ) and zero field electrical resistivity measurements ( $T_\rho$ ). The values outside the round brackets correspond to the cooling mode and the values in the round brackets correspond to the heating mode (data taken from reference [158]).

Compound	$T_m(\text{K})$	$T_\rho(\text{K})$
$\text{SrFeO}_{3.00}$	131.9 (132.0)	
	114.9 (116.1)	110 (112)
	60.9 (70.1)	52 (62)
$\text{SrFeO}_{2.95}$	131.8 (131.1)	
	115.8 (115.5)	114 (115)
	69.8 (74.1)	63(73)
$\text{SrFeO}_{2.85}$	131.1 (131.1)	
	115.1 (115.1)	
	71.0 (74.1)	70 (74)
$\text{SrFeO}_{2.81}$	50.9 (62.1)	50 (62)
$\text{SrFeO}_{2.77}$	47.9 (50.2, 62.2)	48 (52) (60)
	225 (226)	

zone method in an infrared 4-mirror image furnace (see Section 2.1.2). The different stoichiometry of crystals typically depend on the growth conditions [166]. Oxygen deficient  $\text{SrFeO}_{3-\delta}$  with nominal  $\delta = 0.18$  (Sample A) and 0.25 (Sample B) crystals were grown under the tailored growth conditions as shown in table 6.6. Stoichiometric crystals of the end member  $\text{SrFeO}_3$  need post growth high oxygen pressure treatment of  $\sim 5$  Kbar at  $400^\circ\text{C}$  [166]. Since we did not have any in-house facility to post-anneal the crystal at high pressure, our studies focused on non-stoichiometric samples. The Laue pattern of one of the grown crystals is shown in figure 6.6(b). Changes in oxygen content from the melting/growth temperature to room temperature, due to the temperature dependence of equilibrium oxygen partial pressure of the different phases, will lead to severe cracks in the crystals and crystals will break into pieces of few cubic millimetre volume. The oxygen content of the as grown crystals was determined by chemical analysis and crystal structure refinement. Although crystals were grown using the conditions mentioned in the table 6.6(a), the actual oxygen content in the as grown crystals was lower than these nominal values. Sample A exhibits  $\delta = 0.27 (\pm 0.09)$  from infrared absorption analysis

and  $0.23 (\pm 0.03)$  from refinements. Similarly, sample B exhibits  $\delta = 0.35 (\pm 0.13)$  from infrared absorption analysis and  $0.32 (\pm 0.02)$  from structural refinement. This clearly indicates the inhomogeneities in the crystal.

Growth rate, (mm/h)	Oxygen pressure, (bar)	Nominal crystal composition
8.0	3.0	$\text{SrFeO}_{2.77 \pm 0.02}$
5.0	3.0	$\text{SrFeO}_x$
5.0	0.2	$\text{SrFeO}_{2.75 \pm 0.02}$
2.5	3.0	$\text{SrFeO}_x$
2.0	2.0	$\text{SrFeO}_{2.82 \pm 0.02}$
1.5	8.0	$\text{SrFeO}_{2.87 \pm 0.02}$
1.0	3.0	$\text{SrFeO}_{2.85 \pm 0.02}$

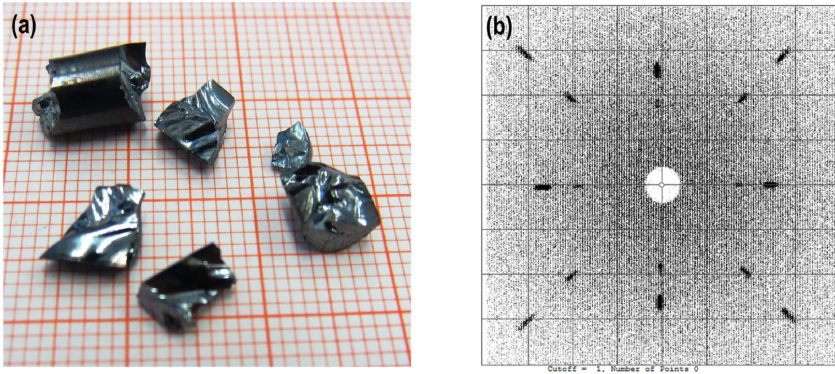


Figure 6.6: Upper panel: The growth conditions for nominal crystal composition, taken from the reference [166]. Lower panel: (a) As grown crystal of  $\text{SrFeO}_{3-\delta}$  (b) x-ray Laue photography of the as grown crystal.

## 6.3 Crystal structure

### 6.3.1 $\text{SrFeO}_{3-\delta}$ , $\delta \sim 0.27 \pm 0.04$

As mentioned previously,  $\text{SrFeO}_{3-\delta}$  exhibits number of phases for different  $\delta$ . Adding to this difficulty, the oxygen vacancy ordering in our case seems to be inhomogeneous throughout the crystal. As a result, different parts of crystal exhibit different physical and structural properties.

Because of the presence of the phase mixture it was difficult to analyze the crystal structure using normal laboratory diffractometer as the diffraction patterns of the different

phases have very similar  $d$ -spacing. Moreover, since x-rays interact with electron clouds of an atom, it is difficult to obtain precise structural information about light atoms, i.e. oxygen in our case, as these scatter relatively much weaker than heavier atoms (the scattering length is proportional to the atomic number). Neutrons, on the other hand, interact with the nuclei with similar scattering length for O, Fe and Sr. In addition, neutron has a magnetic moment and hence microscopic magnetic structures can also be studied. However, the major problem with the oxygen deficient  $\text{SrFeO}_3$  is the presence of twinning and the various minority phases, which hinder the full magnetic and structural refinement by single crystal diffraction (see figure 6.17.)

Neutron powder diffraction (NPD) patterns were hence collected at a high-resolution powder diffractometer, SPODI at MLZ, Garching. A vertical focusing monochromator, consisting of 17 Ge(551) crystal was used to achieve the neutron of wavelength 1.549 Å. About  $\approx 8$  g of polycrystalline powder sample was prepared by grinding the as grown single crystal and the diffraction pattern was collected at two temperatures, 4 K and 300 K. The structural refinement was performed by Rietveld method using the FullProf software. According to the reports, the system with  $\delta = 0.27$  should have orthorhombic structure. Therefore we have started our refinement with the orthorhombic structure (O,  $Cmmm$  space group) i.e., model 1 in the table 6.2. The refinement (of 300 K data) was done by letting the oxygen occupancies free and by fixing the occupancies of Sr and Fe to 100%. Other parameters including the background, atom position, lattice parameters, thermal parameters and instrumental parameters were refined. While refining the structure we have observed that the oxygen occupancies were crossing the maximum limit. For example, O1 in the table 6.4 can have a maximum occupancy of 0.125 per unit cell. When it exceeded this limit, we had to fix that atom position at its maximum occupancy and refine the remaining parameters. The reduced chi-square error (goodness of fit) between the data set and the model was 5.90 and the intensities between the observed and calculated diffraction patterns were well fitted at lower angles. However, there were some discrepancies in intensities at higher angles (figure 6.8(1)). In neutron diffraction the higher angle diffraction pattern contains purely the information about the crystal structure (nuclear scattering length is independent of Q). Therefore, it was necessary to fit the intensities at higher angles. Hence in the next step we have used the model 2, i.e. higher symmetry tetragonal phase (T,  $I4/mmm$ ), and refined the parameters similar to model 1. Although the chi-square value had improved ( $\chi^2 = 4.7$ ), higher angle intensity mismatch remained the same (figure 6.8(2)). Therefore, we fit the data with a model

that consists of mixture of different phases, such as O + C (model 3), T + C (model 4), T + O (model 5) and repeat the refinement again. The low agreement factors ( $R_p$ ,  $R_{wp}$ ,  $\chi^2$ ) obtained by different models are shown in table 6.2 and the refined structure of two selected phases are presented in the figure 6.7. Although the refinements had shown relatively good fit between the observed and calculated diffraction patterns with the different structural models, the discrepancy in intensities at the higher angle remain unsolved. Since there was only a slight lattice difference between the orthorhombic and tetragonal phase and the obtained low agreement factors were nearly the same for all the models, it was difficult to choose the best model for further analysis. Therefore, we have used Akaike information criteria (AIC) which measures the relative quality of a model. AIC value can be calculated by using the formula  $2k - 2\ln(L)$  where  $k$  is the number of free parameters used and  $L$  is the likelihood for an estimated model with  $k$  parameters. The model with the lowest AIC value is the preferred one. Among all the models, the tetragonal phase gave the lowest AIC value. The oxygen stoichiometry obtained from the model 2 gave us  $\delta = 0.23 (\pm 0.03)$  from refining the oxygen occupancies and  $0.27 (\pm 0.09)$  from the infrared absorption analysis. In the figure 6.3, the  $\delta$  with 2.75 and below should exhibit orthorhombic phase and  $\delta$  above 2.75 to 2.875 should exhibit the mixed phase (T+O). However, the presence of cubic and orthorhombic phases was not observed by structural refinement. The reason could be that within the instrumental resolution the small orthorhombic and cubic distortion might not have been observed. In the following we use the values obtained by infrared absorption analysis when referring to the different samples.

Table 6.2: Fraction of different phases and the discrepancy factors obtained in Rietveld refinement of PXRD pattern at 300 K. The values inside the brackets are the standard deviations.

Model	Phases	Fraction (in %)	Discrepancy Factors (in %)		
			$R_p$	$R_{wp}$	$\chi^2$
1	O	-	10.4	10.3	6.48
2	T	-	8.92	8.90	4.70
3	O+C	99.62(0.32) / 0.38(0.01)	10.8	10.6	6.20
4	T+C	99.71(1.33)/0.29(0.13)	8.63	8.46	3.98
5	T+O	81.13(0.84)/18.87(0.19)	8.62	8.64	4.42

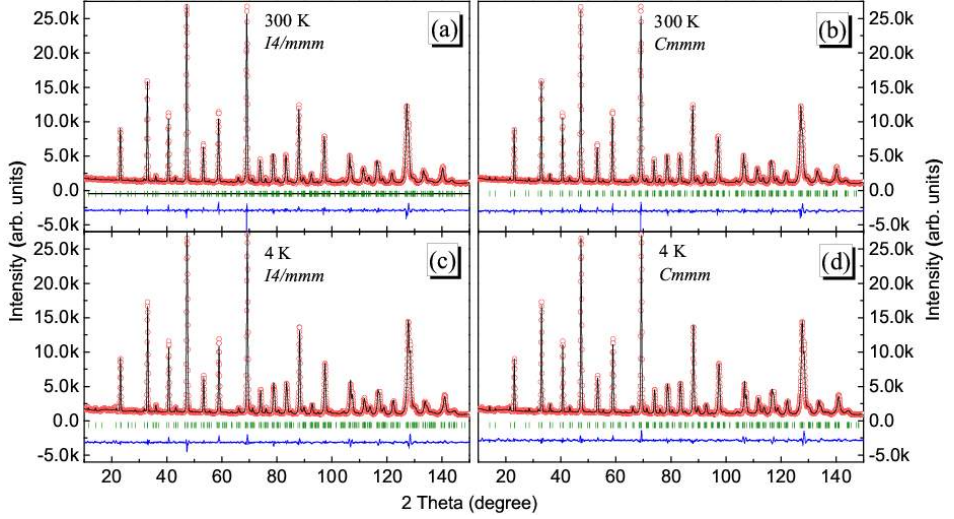


Figure 6.7: Rietveld refinement of the PXRD pattern at 300 K and 4 K. The refinement was performed considering the single phase. Red circles represent the data points, black and blue lines represent the calculated pattern and differences respectively.

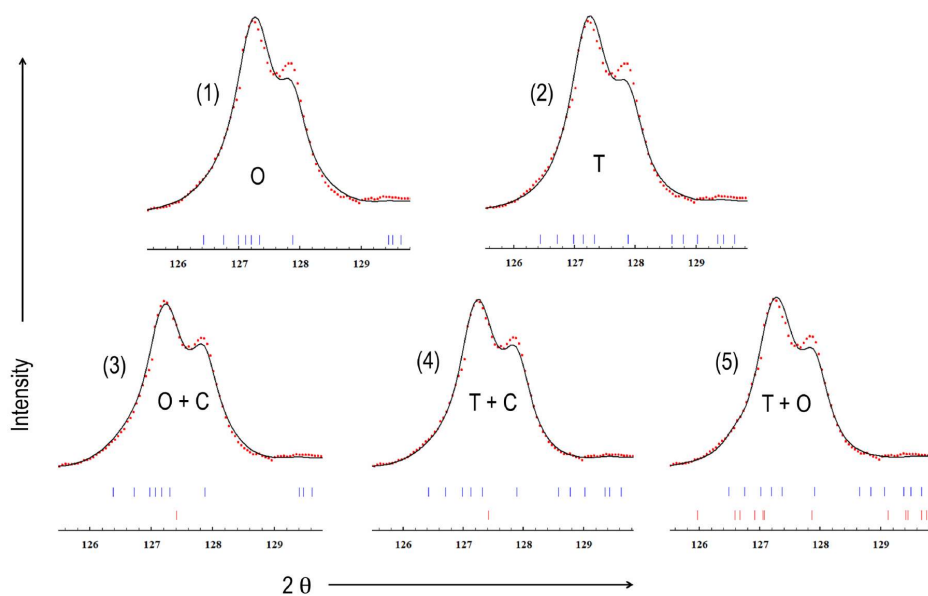


Figure 6.8: Discrepancy in intensity between the different models at 300 K. Red circles represent the data points and the black line represents the calculated pattern.

Table 6.3: Structural parameters obtained from the Rietveld refinement of 300 K NPD data in tetragonal space ( $I4/mmm$  space group) (model 2)

Atoms	Wyckoff positions	x	y	z	Biso
Sr1	8j	0.25639(67)	0	0	0.65138
Sr2	8j	0.24811(69)	0	0.5	0.65138
Fe1	4e	0	0	0.25244(138)	0.34083
Fe2	8f	0.25	0.25	0.25	0.34083
Fe3	4d	0.5(9)	0	0.25	0.34083
O1	2b	0	0	0.5	0.62834
O2	16m	0.11866(43)	0.11866(43)	0.23065(76)	0.62834
O3	8h	0.23741(54)	0.23741(54)	0.5	0.62834
O4	16k	0.12557(51)	0.62557(51)	0.25	0.62834
O5	4c	0.5	0	0.0	0.62834
Unit Cell Dimensions					
$a = 10.9319(22) \text{ \AA}$		$c = 7.70059(17) \text{ \AA}$		$V = 920.278(33) \text{ \AA}^3$	

### 6.3 Crystal structure

Table 6.4: Structural parameters obtained from the Rietveld refinement of 300 K NPD data in orthorhombic phase (Cmmm space group) (model 1).

Atoms	Wyckoff positions	x	y	z	Biso
Sr1	2c	0.5	0	0.5	0.58367
Sr2	2d	0	0	0.5	0.58367
Sr3	4g	0.25717(205)	0	0	0.58367
Fe1	4i	0.5	0.24578(269)	0	0.29011
Fe2	4f	0.25	0.25	0.5	0.29011
O1	2b	0.5	0	0	0.45880
O2	4h	0.26553(213)	0	0.5	0.45880
O3	16r	0.37449(151)	0.27893(180)	0.22413(340)	0.45880
Unit Cell Dimensions					
$a = 10.96264(76) \text{ \AA}$ $b = 7.69950(52) \text{ \AA}$ $c = 5.47090(48) \text{ \AA}$ $V = 461.782(60) \text{ \AA}^3$					

Table 6.5: Fraction of different phases and the discrepancy factors obtained in Rietveld refinement of PXRD pattern at 4 K. The values inside the brackets are the standard deviations.

Model	Phases	Fraction (in %)	Discrepancy Factors (in %)		
			$R_p$	$R_{wp}$	$\chi^2$
1	T	-	8.40	8.37	5.00
2	O	-	9.19	9.41	6.13
3	M	-	14.6	15.3	15.6
4	T+O	90.08(1.33) / 9.92(0.78)	8.08	8.00	4.35
5	T+C	85.14 (85.14)/14.86(0.20)	9.26	9.41	6.45
6	M+O	3.67(0.37)/96.33(6.84)	8.08	8.07	4.36
7	T+C+O	89.99(5.02)/2.55(0.27)/7.46(1.28)	8.09	7.96	4.29

In an ideal case of tetragonal phase of  $\text{SrFeO}_{3-\delta}$  ( $\delta = 0.125$  or  $\text{Sr}_8\text{Fe}_8\text{O}_{23}$ ), out of the three Fe sites, the Fe1 sites are five fold coordinated by oxygen atoms and form a square pyramid; the other two iron sites are sixfold coordinated and all polyhedra are connected through corner sharing oxygen atoms. Due to oxygen deficiency the Fe1 site



leads to the  $\text{FeO}_5$  square pyramids, two of which form dimers via sharing the O1 atom [167][see figure 6.2(a)]. Further decrease in oxygen leads to an orthorhombic phase ( $\delta = 2.75$  or  $\text{Sr}_4\text{Fe}_4\text{O}_{11}$ ) that contains corner-sharing square pyramidal  $\text{Fe1O}_5$  and  $\text{Fe2O}_6$  octahedra [168] (see figure 6.2(b)). The results of structural refinement with tetragonal phase showed that an ideal value of the z-parameter of Fe1 atom in  $\text{FeO}_5$  unit is shifted from 0.25 to 0.25244(138). The Fe atom is shifted out of the plane because of the oxygen deficiency at one of the apical oxygen sites. Refined structural parameters are tabulated in the tables 6.3 and 6.4. In order to solve the low-temperature crystal structure, the refinement was carried out in a combination of different phases as shown in table 6.5. The refinement was done in a similar way as mentioned earlier. Very recently Reehuis and co-workers refined the low temperature crystal structure of  $\text{Sr}_3\text{Fe}_8\text{O}_{23}$  (below the charge ordering temperature, 70 K) in monoclinic phase in the  $\text{I2/m}$  space group [165]. Since we have proposed that in our system the room temperature structure is tetragonal, similar attempts were made to solve the low temperature crystal structure. But we were unable to achieve a reliable fit using the  $\text{I2/m}$  space group. The obtained goodness of fit was 15.6 % and the results are tabulated in the table 6.6. The value of  $\chi^2$  is relatively high in all the models. This is due to the presence of additional intensities from magnetic structure in the low temperature phase. Therefore it is difficult to draw a firm conclusion as to which phase the low temperature structure belongs to.

### 6.3.2 $\text{SrFeO}_{3-\delta}$ , $\delta \sim 0.35 \pm 0.03$

Powder x-ray diffraction was performed using in-house laboratory X-ray diffractometer on a finely powdered crystal.  $\text{Cu-K}_\alpha$  radiation of  $\lambda = 1.54059 \text{ \AA}$  was used for the measurement. The diffraction patterns were collected in transmission geometry using Huber x-ray diffractometer equipped with a G670 Guiner camera with integrated imaging plate detector. The crystal structure was refined in tetragonal,  $\text{I4/mmm}$  space group and the refined lattice parameters were  $a = b = 10.9212(29) \text{ \AA}$ ,  $c = 7.6945(21) \text{ \AA}$  and the unit cell volume,  $V = 917.739(0.043) \text{ \AA}^3$ . The refinement was also performed in orthorhombic phase ( $\chi^2 = 1.05 \%$ ) as well as in the combination of O + T phases ( $\chi^2 = 0.973 \%$ ). But the best fit was obtained for tetragonal phase with  $\chi^2 = 0.643 \%$ . The refined structure is presented in figure 6.9.

Table 6.6: Structural parameters obtained from the Rietveld refinement of 4 K NPD data in monoclinic ( $I2/m$  space group) (model 3).

Atoms	Wyckoff positions	x	y	z	Biso
Sr1	4i	0.25862(231)	0	1.00790(358)	0.16752
Sr2	4g	0	0.26221(222)	0	0.16752
Sr3	4i	0.23642(211)	0	0.48680(296)	0.16752
Sr4	4h	0	0.25591(238)	0.5	0.16752
Fe1	4i	0.98939(173)	0	0.24604(175)	0.33696
Fe2	4e	0.25000	0.25	0.25	0.33696
Fe3	4f	0.25000	0.25	0.75	0.33696
Fe4	4i	0.50050(0)	0	0.25	0.33696
O1	2d	0	0	0.5	0.79972
O2	8j	0.12517(173)	0.12795(265)	0.23845(318)	0.79972
O3	8j	0.10600(191)	0.12640(189)	0.76074(255)	0.79972
O4	8j	0.23916(124)	0.23916(124)	0.49603(245)	0.79972
O5	8j	0.11327(196)	0.63316(222)	0.24021(425)	0.79972
O6	8j	0.13128(194)	0.61990(253)	0.74450(612)	0.79972
O7	2c	0.5	0	0.0	0.79972
O8	2c	0.0	0.5	0.0	0.79972
Unit Cell Dimensions					
$a = 10.8758(23) \text{ \AA}$		$b = 10.8777(21) \text{ \AA}$		$c = 7.72176(37) \text{ \AA}$	
$\beta = 90.09047^\circ$		$V = 913.520(265) \text{ \AA}^3$			

## 6.4 Macroscopic magnetic properties

### 6.4.1 $\text{SrFeO}_{3-\delta}$ ( $\delta \sim 0.27 \pm 0.04$ )

Field-cooled (FC, measured on cooling) and zero-field-cooled (ZFC) magnetization curves measured with an applied field of 1000 Oe are shown in the figure 6.10(a). On lowering the temperature the sample shows two major anomalies – one around 230 K and another around 70 K. The anomalies around 70 K correspond to well known antiferromagnetic

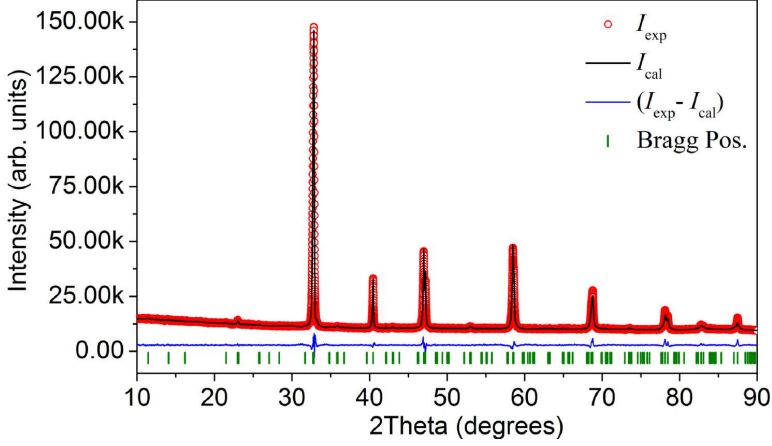


Figure 6.9: Rietveld refinement of the powder X-ray diffraction pattern at 300 K. The refinement was performed considering the tetragonal phase. Red circles represent the data points, black and blue lines represent the calculated pattern and differences respectively.

(AFM) ordering of tetragonal phase [167]. The anomaly observed around 230 K coincides exactly at the  $T_N$  of orthorhombic phase. Therefore, we predict that it could belong to the AFM ordering of orthorhombic phase. The small anomaly at around 130 K (represented by arrow) indicates the presence of a tiny fraction of cubic phase. Isothermal magnetization curves measured at different temperatures are presented in the figure 6.10(b). We did not observe any hysteresis loop in  $M(H)$  measurement above 100 K. After decreasing the temperature below the anomaly 70 K an extremely small hysteresis loop opening was observed and the magnetic moments are not saturated even at the high field 7 T. The presence of this coercivity could be an indication of the presence of ferromagnetic (FM) clusters in the system. Since the magnetic interactions are via nearest neighbor oxygen atoms, the presence of oxygen vacancies could change the interactions between the two iron atoms in the vicinity of the vacancy. The observed large difference between ZFC-FC magnetization curves indicates the appearance of a spin-glass like state in the low temperature phase of the system.

Spin glasses are disordered and frustrated magnetic systems. The spin glass states have been observed in various rare earth manganite systems [169, 170], amorphous materials [171, 172], spinels [173], and extensively in diluted magnetic alloys [174, 175]. In certain diluted magnetic alloys, for e.g. in AuFe, AgMn, CuMn, known as canonical

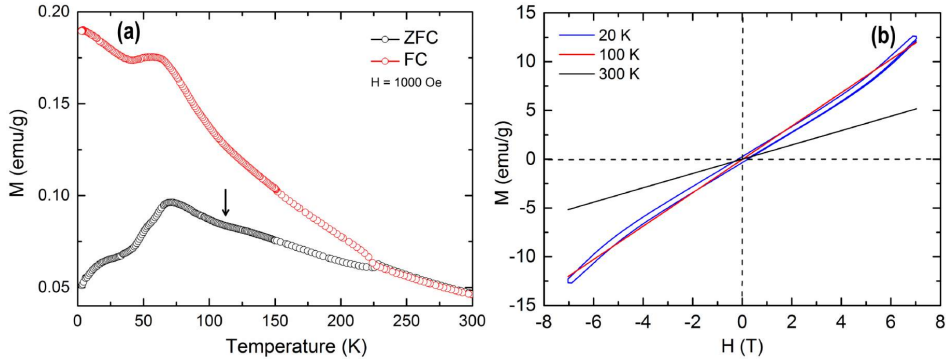


Figure 6.10: (a) DC magnetization of  $\text{SrFeO}_{3-\delta}$ , ( $\delta \sim 0.27$ ) at 1000 Oe (FC was measured on cooling). (b) Hysteresis curves measured at 20 K, 100 K and 300 K.

spin-glasses, the spin-glass state is formed by the competing ferromagnetic double exchange and anti-ferromagnetic superexchange near-neighbor interactions [176]. In case of dense magnetic systems, for e.g. in rare earth manganites, the spin-glass state arises due to disorder of sites or bonds, as well as due to competing exchange interactions. Some of the macroscopic experimental signatures of spin-glass state are frequency dependent AC-susceptibility below the spin-glass phase transition temperature ( $t_g$ ), divergence in the FC and ZFC curves in DC-magnetic susceptibility below  $t_g$ , aging and memory effect below  $t_g$  [176]. In order to study the presence of spin-glass like state, AC-susceptibility measurements at two frequencies and DC-magnetization memory experiments on the zero-field-cooled magnetization have been performed at PPMS. The frequency dependence of a cusp around at 60 K which is observed in AC-susceptibility measurement and shown in figure 6.11(a), indicates a glassy nature of the system. This was confirmed by memory experiments the results of which are presented in figure 6.11(b) and (c). The ZFC curves shown in the figure 6.11(b) were measured on reheating with 1000 Oe field, after direct cooling (black color) and cooling with an intermediate waiting time of 3 hours at 200 K and 20 K (red color) in zero field. Thus the system was aged during the waiting time and this aging was kept in memory on further cooling. The magnetic relaxation of the system is observed by the broad dip, the so called memory dip, at 20 K. This presence of memory effect clearly indicated the existence of glassy state below the anomaly 70 K. The clear difference between the two ZFC curves is shown in the 6.11(c). The maximum at 20 K observed exactly at the waiting time in the difference curve  $\Delta M = M_{\text{stop}} - M_{\text{No-Stop}}$  indicates a clear signature of the memory effect. In contrast, no dip was observed in  $M(T)$

for waiting at 200 K and this suggests an absence of spin glass like behavior below the anomaly 230 K.

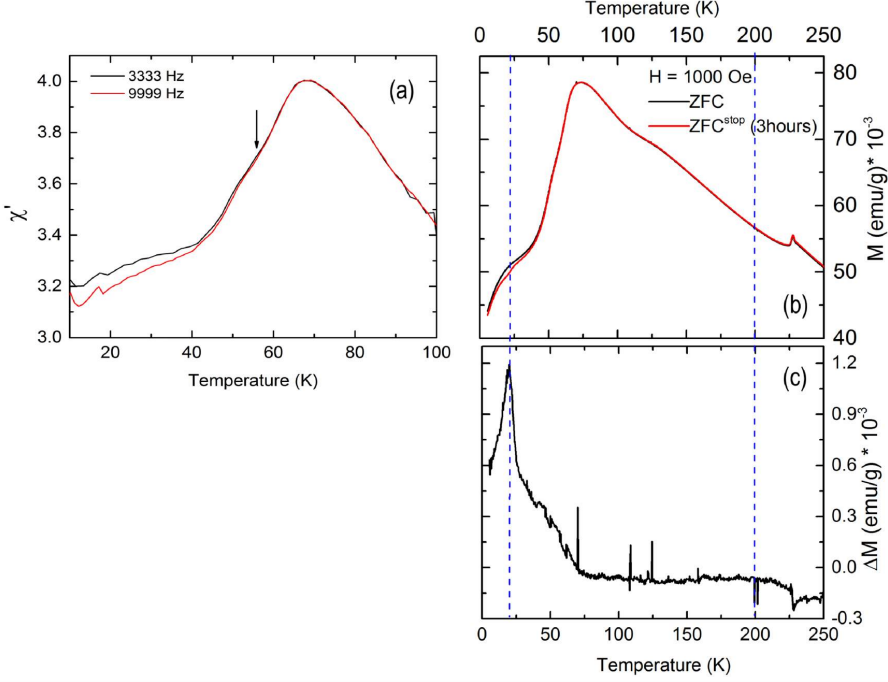


Figure 6.11: (a) Real component of the AC-susceptibility vs temperature at two frequencies. Black arrow indicates the frequency dependence of the cusp observed at around 60 K. (b) Memory effect observed in the ZFC-magnetization measurement. The black line represents the reference curve and the red line represents the curve measured with stop and waiting for 3 hours at 20 K and 200 K while cooling. (c) Plot of difference curve  $ZFC_{no-stop} - ZFC_{stop}$  vs temperature.

It is well known that the materials with multiple magnetic phases are likely to exhibit exchange bias (EB) effect [177, 178]. EB is a phenomenon associated with the exchange interaction between the spins at the interface of inhomogeneous magnetic systems, such as FM/AFM, FM/SG or hard/soft FM systems. Such an effect is manifested as a shift of the magnetic hysteresis loop, to either negative or positive direction relative to the zero field position, with respect to the applied magnetic field [179]. The EB has been measured at 15 K and 200 K by cooling the system in an applied magnetic field of +5 T. As shown in the figure 6.11(a), the measured  $M(H)$  loop is slightly shifted from the origin at 15 K. Similar exchange bias like effect was also observed in  $\delta = 0.25$  and 0.17 systems [167, 180]. Although the physical origin of this effect is not clear, different explanations

were stated by different authors depending on their experimental results. Srinath and co-workers attributed the observed effect to competing antiferro and ferromagnetic interactions in a helical spin system [180] whereas williams and co-workers attributed it to the  $\text{Sr}_4\text{F}_4\text{O}_{11}$  (orthorhombic) phase [167]. In the orthorhombic phase,  $\text{Fe}^{3+}$  magnetic moments order antiferromagnetically below the Neel temperature whereas  $\text{Fe}^{4+}$  magnetic moments remain spin frustrated [168, 181].

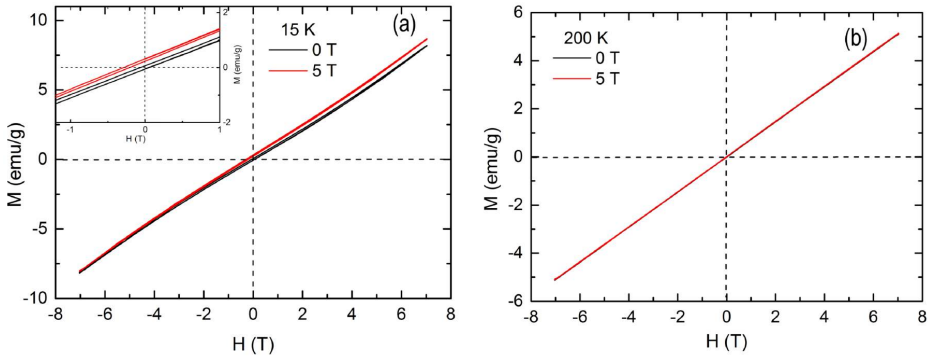


Figure 6.12: (a) and (b) are hysteresis measured at 15 K and 200 K, after cooling in 0 T and 5 T. The inset in the fig (a) is the enlarged view of shifted  $M(H)$  loop from the origin.

#### 6.4.2 $\text{SrFeO}_{3-\delta}$ ( $\delta \sim 0.35 \pm 0.03$ )

FC and ZFC magnetization curves of  $\text{SrFeO}_{2.65}$  system are presented in the figure 6.13(a). The anomaly observed at around 60 K in the temperature dependent magnetization is attributed to the tetragonal phase, however, shifted to a low temperature from 70 K in  $\text{SrFeO}_{2.73}$ . The anomaly observed at around 230 K in the FC and ZFC curves measured at 30 Oe indicates the presence of orthorhombic phase in the system (shown in the inset of figure 6.13(a)). Interestingly, the anomaly at around 60 K in magnetization curve demonstrates typical spin-glass like behavior, with a large bifurcation in the FC and ZFC curves. In order to test the existence of spin-glass state, ac-susceptibility and memory experiment was performed as explained in the previous section. The observed frequency dependent ac-susceptibility and memory effect in the low temperature phase, presented in the figure 6.14 (a), (b) and (c), clearly indicates the presence of glassy state. Similar to the system  $\delta \sim 0.27$ , ferromagnetic clusters and shift of  $M(H)$  loop from the origin was also observed below the anomaly 60 K, and are presented in the figures 6.13(b) and

6.15(a) respectively.

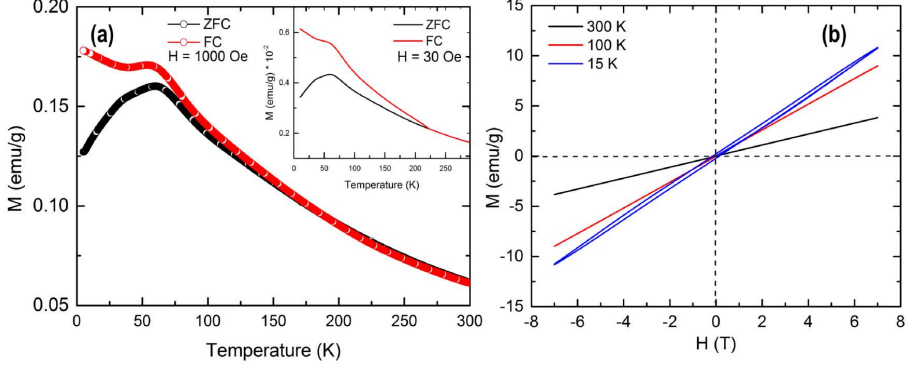


Figure 6.13: (a) DC magnetization of  $\text{SrFeO}_{3-\delta}$ , ( $\delta \sim 0.35$ ) at 1000 Oe. (b) Hysteresis curves measured at 15 K, 100 K and 300 K.

Our results of exchange bias effect on both the systems ( $\delta \sim 0.27$  and  $0.35$ ) completely disagree with the results reported by Srinath *et al* [180] on a similar system ( $\delta = 0.18$ ). Although the  $\delta$  is different in the present study and the reports, the magnetization and hysteresis curves look similar. Srinath *et al* mentioned that they have observed exchange-bias-like effect below the  $T_N$  of orthorhombic phase i.e., 230 K, and attributed the anomaly around 230 K in the system  $\delta = 0.18$  to competing ferro and antiferro magnetic interactions. However, in the present study, the absence of exchange-bias-like effect at 200 K completely ruled out the explanation stated by Srinath *et al*. Moreover the  $M(H)$  loop is not saturated even at 7 T. In such cases shift of the curve from the origin cannot be attributed to exchange-bias-like effect. The presence of spin-glass state for temperature below  $\sim 60$  K could be due to the spin frustrated  $\text{Fe}^{(4+)}$  moments of orthorhombic phase, disorder and competing exchange interactions.

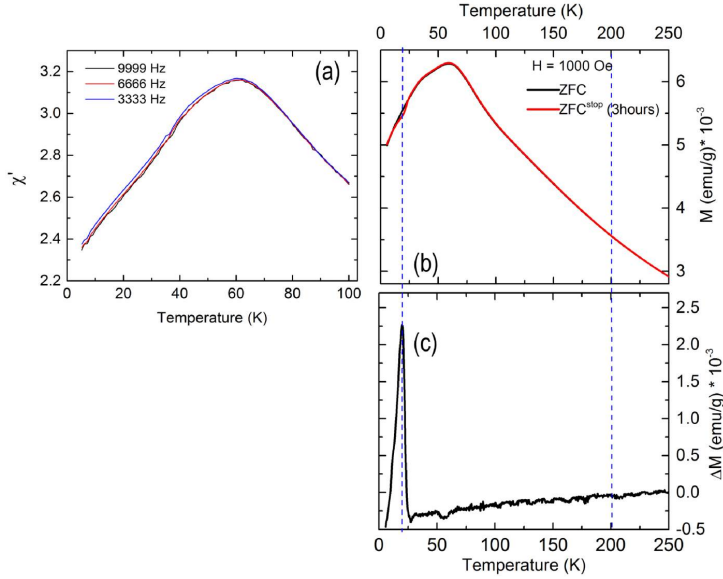


Figure 6.14: (a) Real component of the AC-susceptibility vs temperature at different frequencies. (b) Memory effect observed in the ZFC magnetization measurement. The black line represents the reference curve and the red line represents the curve measured with stop and waiting for 3 hours at 20 K and 200 K while cooling. (c) Plot of difference curve ZFC-ZFC<sub>No-Stop</sub> vs temperature.

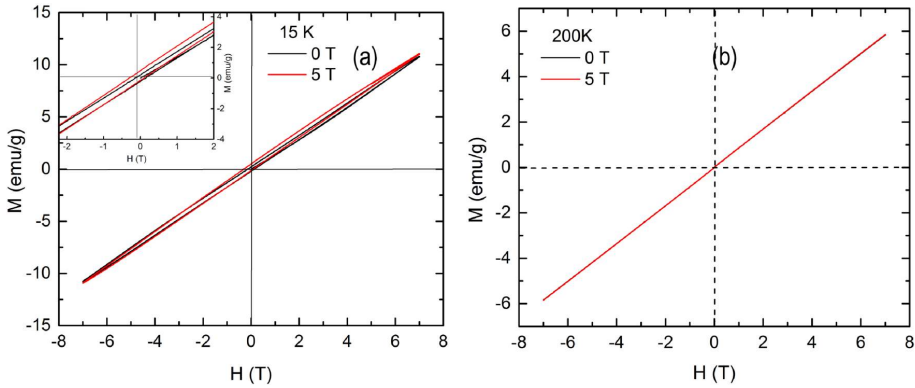


Figure 6.15: (a) and (b) are hysteresis measured at 15 K and 200 K, after cooling in 0 T and 5 T. The inset in the fig (a) is the enlarged view of shifted  $M(H)$  loop from the origin.



## 6.5 Neutron diffraction with $xyz$ -polarization analysis

Neutron scattering with  $xyz$ -polarization analysis was performed on oxygen deficient  $\text{SrFeO}_{3-\delta}$  ( $\delta = 0.77, 0.63$ ) crystals at the high flux Diffuse Neutron Spectrometer (DNS), MLZ Garching (see Section 2.6.4). Our idea was to map both  $hhl$  and  $h0l$  planes in reciprocal space at different temperatures on different stoichiometric crystals to study the magnetic structure and the directions of the magnetic moment. Though there were a few studies on the magnetic structure of  $\text{SrFeO}_3$  and  $\text{SrFeO}_{2.99}$  reporting screw spin structure with the  $k \parallel [111]$  direction [41, 164], a detailed study of non-stoichiometric system was lacking. Since the oxygen deficient systems are mixtures of multiple phases there could evolve more than one magnetic structure with decreasing  $\delta$ . It was also confirmed by recent neutron diffraction studies on  $\text{SrFeO}_{3-\delta}$  by Reehuis and coworkers [165], which was performed at the same time as the present study and which revealed seven different magnetic structure in the range of  $\delta = 0 - 0.23$  (table 6.19). The use of polarized neutrons and mapping the reciprocal space with polarization analysis enables us to distinguish unambiguously between lattice and magnetic part and thus would give more information about the magnetic structure by separating the non magnetic scattering contribution from the magnetic contribution. In addition, measuring the magnetic intensity in three orthogonal directions,  $xyz$ , of the incident polarization vector  $P$  with respect to scattering vector  $Q$  would give additional information about the anisotropic spin-correlations [182]. A single crystal approximately of 200 mg was pre-aligned in the ( $hhl$ ) scattering plane using in-house x-ray Laue diffractometer and mounted on a aluminum sample holder. After mounting on the sample holder, the orientation was checked and the holder was placed inside the sample chamber of the instrument. For obtaining the  $hhl$ -maps the sample was oriented in such a way that the  $c$ -axis and the  $[110]$ -axis build the horizontal scattering plane. Only  $\omega$  movement of the sample is allowed in DNS. By  $\omega$  rotation and  $2\theta$  degree of freedom from the position sensitive 1D detector it is possible to measure the whole  $hhl$ -plane. A neutron wavelength of  $4.74 \text{ \AA}$  corresponding to the incident energy of  $3.64 \text{ meV}$  was used for the experiment. The incident beam was polarized successively in the  $x, y$  and  $z$  directions. Measurements were carried out in both spin flip and non-spin flip channels with the different guide field directions defining the neutron spin quantization axis. The geometry of the  $xyz$  field directions is shown in the figure 6.16. As can be seen in the figure,  $x$  is in the horizontal scattering plane and in the

direction of the average  $Q$ -vector and  $z$  is vertical. The  $y$ -axis is perpendicular to both  $x$  and  $z$ . Measuring the spin flip and non-spin flip intensities in  $x$  and  $z$  - directions means aligning the neutron polarization  $P \parallel x \parallel Q$  and  $P \parallel z \perp Q$  respectively. Only the component of sample magnetization  $M \perp Q$  contributes to the scattering. Hence the  $x$ -component of  $M^{\perp Q}$  is  $\approx 0$  because  $x$  is parallel to the average vector  $Q$  [183]. With the polarization perpendicular to  $Q$  and in the  $z$ -direction, the conditions for spin-flip and non-spin-flip scattering intensities leads to [183]:

$$M^{\perp Q} \perp P \quad \text{Spin - Flip} \quad (6.1)$$

$$M^{\perp Q} \parallel P \quad \text{Non - Spin - Flip} \quad (6.2)$$

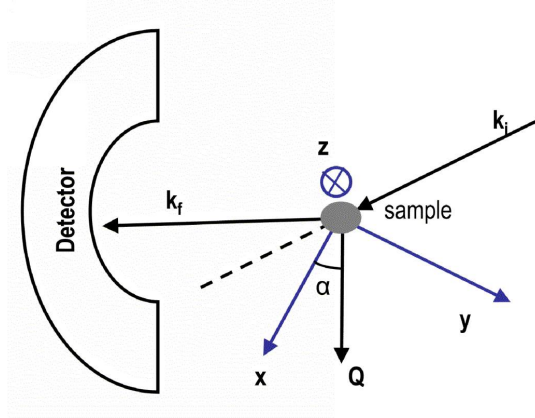


Figure 6.16: Different field directions at DNS

The DNS data were plotted using the program written by Dr. Artur Glavich [184]. Background corrections of all DNS images were done by subtracting measured intensities of the sample from the measured intensity of the empty sample holder and normalized to the nuclear incoherent scattering of a vanadium standard sample. 100% efficient neutron polarizers or analyzers are not achievable. Therefore, a small fraction of neutrons with wrong polarization enter the detector, which needs to be corrected before further processing the data. This is called the flipping ratio correction. This was done by measuring with an ideal isotropic incoherent scatterer NiCr alloy. A drawback of the DNS instrument is that it has ellipsoidal resolution with the low vertical (i.e. perpendicular to the scattering plane) resolution. This means that the obtained  $(hhl)$  intensities correspond to an integration of all intensities over a certain range in  $(h\bar{h}l)$  direction. This

bad vertical resolution has to be taken into account while analyzing the DNS data.

### 6.5.1 Results $\text{SrFeO}_{3-\delta}$ ( $\delta \sim 0.27 \pm 0.04$ )

Figure 6.18 shows contour plots of the observed magnetic intensities for  $(hhl)$  and  $(h0l)$  planes of the reciprocal space at 3.5 K. The polarization analysis was carried out with  $P \parallel x \parallel Q$  (approximately). With the  $x$  polarization of the incident beam, all the magnetic scattering regardless of the direction of the magnetic moment will be spin-flipped to a good approximation, because  $M^{\perp Q} \perp P \parallel Q$ . The UB matrix for the measurement was defined in tetragonal coordinate system with  $a = b = 10.929 \text{ \AA}$  and  $c = 7.698 \text{ \AA}$  (unit cell dimension  $2\sqrt{2}a_c \times 2\sqrt{2}a_c \times 2a_c$  with space group  $I_4/mmm$ ). The change from cubic to lower symmetry of  $\text{SrFeO}_3$  leads to twinning of the crystal by 90 degree. The schematic diagram of twinning in the crystal due to the lowering of symmetry from cubic to tetragonal phase is shown in figure 6.17. Because of the presence of twinning, determination of exact magnetic structure was complicated.

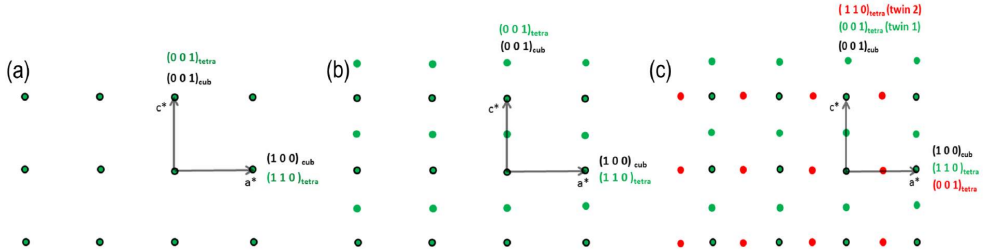


Figure 6.17: Schematic diagram of a two dimensional periodic lattice: (a) in cubic unit cell, (b) in tetragonal unit cell: doubling of the tetragonal  $c$ -axis is represented by green circle, (c) In case of twinning: interchange of  $a$  and  $c$ -axis, represented by red circle.

As visible in the figure 6.18 several sets of strong and weak magnetic reflections were observed at low temperature. The indexed magnetic Bragg peak with the propagation vector  $(001/2)_t$  or  $(001/4)_c$  is marked in pink in figure 6.18 left panel. The peak marked in black is equivalent and results from the tetragonal twin with  $[001]_{\text{tetra}}$  horizontal. This wave vector was also observed by Reehuis *et al* and labeled as phase IV in the table 6.19. According to Reehuis *et al* this phase corresponds to a canted antiferromagnetic spin structure of the tetragonal phase and the moments are canted with respect to the  $c$ -axis [165]. Other sets of Bragg peaks in the left panel could be

indexed as  $(0.15\ 0\ 0.15)_c$  (orange circle),  $(\overline{0.25}\ 0\ \overline{0.15})_c$  (blue circle)  $(\overline{0.25}\ 0\ 0.25)_c$  (yellow circle) and in the right panel  $(\overline{0.25}\ \overline{0.25}\ 0.5)_c$  (white circle) in cubic setting.

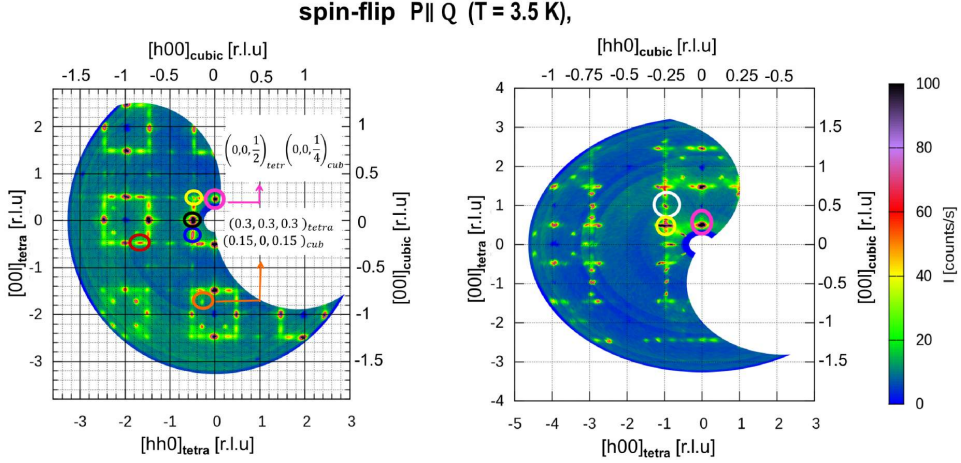


Figure 6.18: Scattered intensity in spin-flip channel with  $P \parallel x$  i.e., approximately  $\parallel Q$ , measured in  $hhl$ -plane and  $h0l$ -plane at 3.5 K.

Magnetic phase	Propagation vector $k$	Type of spin order	$T_N$ (K)	Samples	Crystal structure
Phase I	$(0.13, 0.13, 0.13)_{\text{cub}}$	Helical	133(1), 134 (Ref. 1)	$\text{SrFeO}_{2.87-3.00}$ (crystal)	$\text{SrFeO}_3$
Phase II	$(0.20, 0.20, 0.20)_{\text{cub}}$	Helical	75(2)	$\text{SrFeO}_{2.87}$ (crystal)	$\text{Sr}_3\text{Fe}_8\text{O}_{23}$
Phase III	$(0.17, 0.17, 0.17)_{\text{cub}}$ $(0.687, 0, 0.326)_{\text{mon}}$	SDW	75(2)	$\text{SrFeO}_{2.87}$ (powder)	$\text{Sr}_3\text{Fe}_8\text{O}_{23}$
Phase IV	$(0, 0, \frac{1}{2})_{\text{cub}}$ $(0, 0, \frac{1}{2})_{\text{tetra}}$	Canted AF	65(4)	$\text{SrFeO}_{2.77-3.00}$ (crystal)	Unknown
Phase V	$(0.30, 0.30, 0.75)_{\text{cub}}$	SDW or helical	110(4)	$\text{SrFeO}_{2.77}$ (crystal)	Unknown
Phase VI	$(0.79, 0.79, 0)_{\text{cub}}$	SDW or helical	60(5)	$\text{SrFeO}_{2.77}$ (crystal)	Unknown
Phase VII	0	AF	232(2), 232(4) (Ref. 8)	$\text{SrFeO}_{2.77}$ (crystal)	$\text{Sr}_4\text{Fe}_4\text{O}_{11}$

Figure 6.19: Seven magnetic structures in the system  $\text{SrFeO}_{3-\delta}$  ( $\delta$  from 0-0.24) observed by Neutron diffraction measurements, taken from reference [165]

Considering the bad vertical resolution of the instrument, the Bragg peak  $(0.15\ 0\ 0.15)_c$  is likely a remnant of the Bragg peak  $(0.15\ 0.15\ 0.15)_c$  visible in the right panel (also marked orange) – as these equivalent peaks have generally more intensity in the  $(hhl)_c$  plane. Considering the error bars in the magnitude of the propagation vector, these peaks can be matched as phase I in the table 6.19. This is also supported by the observation of this peak at even 120 K [see figure 6.20]. Fig 6.20 shows the  $(hhl)$  reciprocal planes measured at different temperatures. The phase I corresponds to helical spin ordering. The Bragg peak  $(\overline{0.25}\ \overline{0.25}\ 0.5)_c$  can be indexed as phase VII. This is a structural peak

### spin-flip ( $P \parallel Q$ )

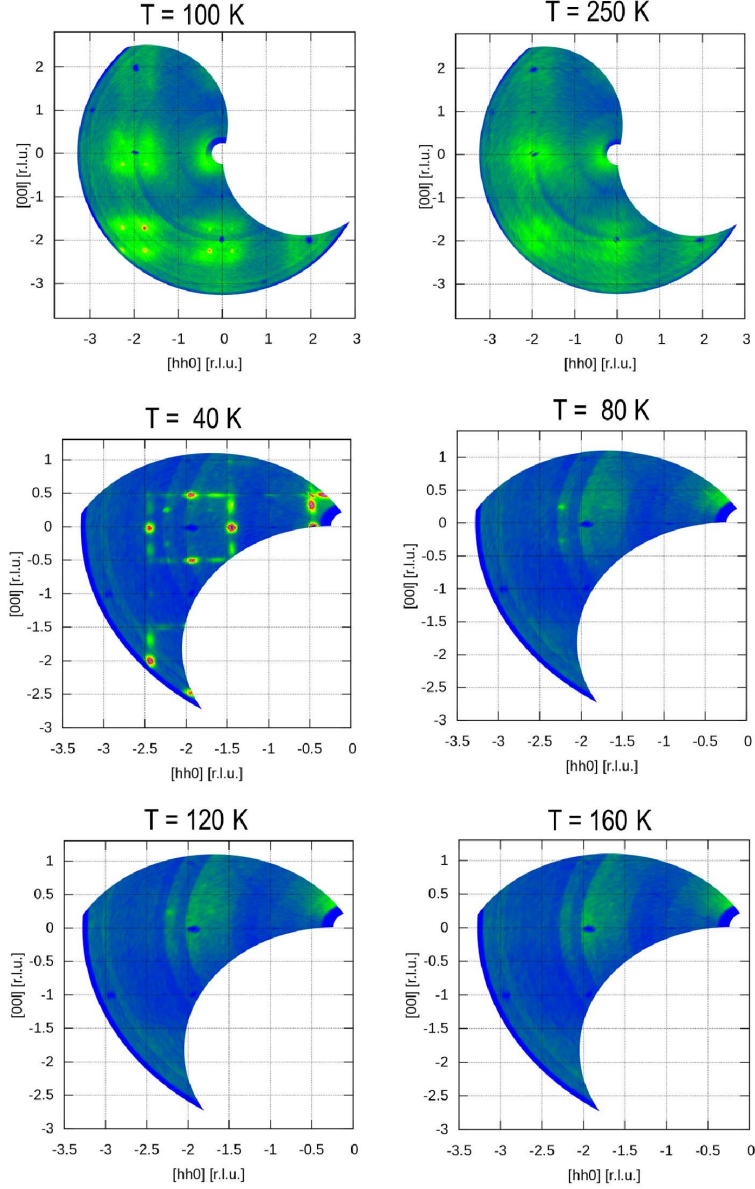


Figure 6.20: Scattered intensity in spin-flip channel with  $P \parallel x$  i.e., approximately  $\parallel$  to  $Q$ , measured in  $hhl$  - plane at different temperatures.

of the tetragonal and orthorhombic phases, which can also be seen in the non-spin-flip channel, figure 6.23 (white circle). The phase VII belongs to antiferromagnetic spin ordering. The Bragg reflection  $(\overline{0.25} \ 0 \ 0.25)_c$  is likely also a resolution effect with its real position  $(\overline{0.25} \ \overline{0.25} \ 0.25)_c$  as indexed by stronger intensity at the corresponding position in the  $(hhl)_c$  plane (figure 6.20 right panel, also marked in yellow) and  $(\overline{0.25} \ 0 \ \overline{0.15})_c$  is an observed new wave vector which was not reported before. The closest  $(0.30 \ 0.30 \ 0.75)_c$ , phase V, and  $(0.20 \ 0.20 \ 0.20)_c$ , phase II, is off by more than the error bars and the phase V has a completely different temperature dependence. Neither  $(0.25 \ 0.25 \ 0.25)_c$  nor  $(0.25 \ 0 \ 0.15)_c$  wave vectors were observed before. Hence this corresponds to a new magnetic phase. The presence of diffuse scattering around the magnetic bragg reflections indicate the presence of short range correlations in the system.

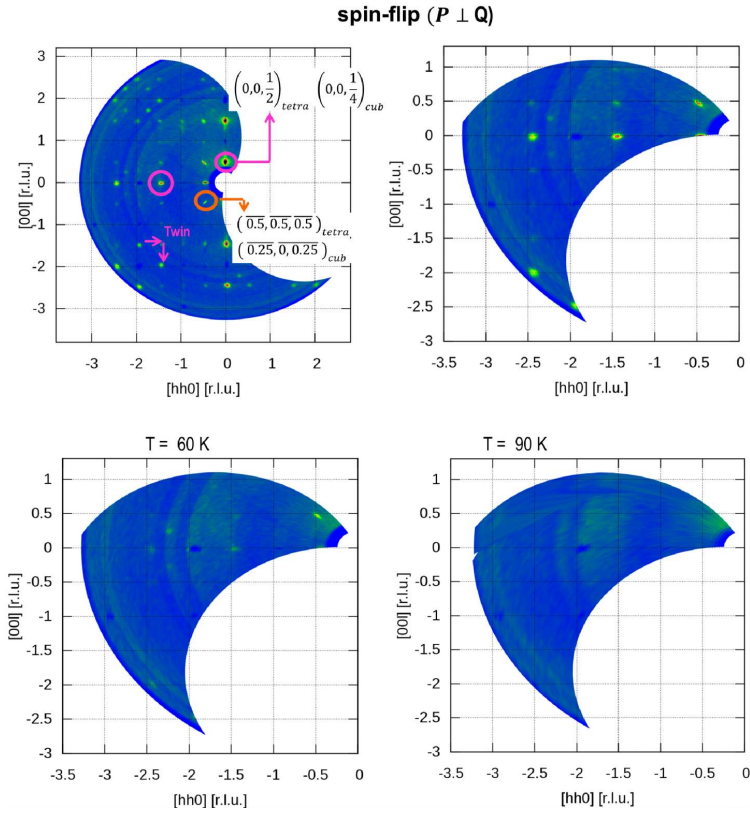


Figure 6.21: Scattered intensity in spin-flip channel with  $P \parallel Z$  i.e.,  $\perp Q$ , measured in  $hhl$  - plane at different temperatures.

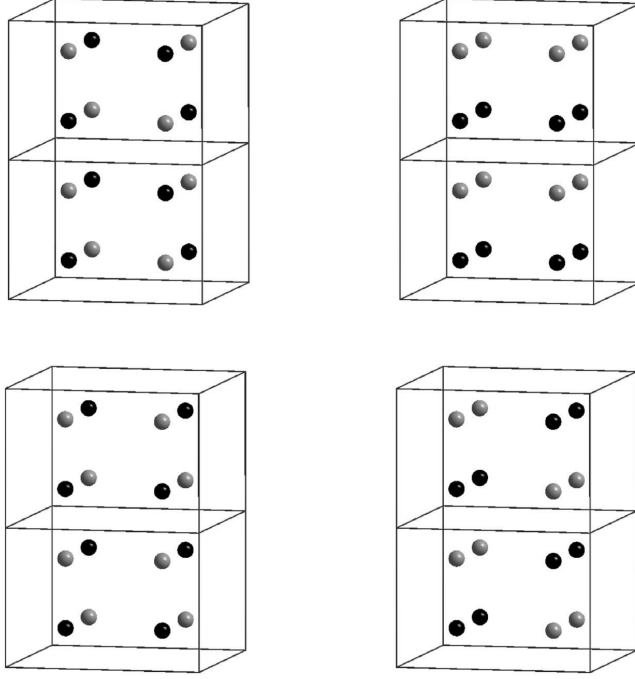


Figure 6.22: Sketch of possible charge configuration at the Fe2 site of tetragonal phase.

In order to determine the orientation of the spin moment, neutron polarization analysis with  $\mathbf{P} \parallel z$  i.e.,  $\mathbf{P} \perp$  to the scattering plane was performed. Figure 6.21 shows the contour plots of observed magnetic intensities for  $(hhl)$  plane of the reciprocal space at different temperatures. The intensity of the magnetic reflections, as well as the diffuse scattering reduced by changing the polarization direction from  $x$  to  $z$  and completely vanished above 60 K. The reduced intensity in  $z$ -polarization indicates that the majority of spins lie in the  $ab$ -plane and a small fraction of the spins are aligned along  $c$ . The observed strong magnetic intensities in figure 6.21 correspond to the propagation vector  $\mathbf{k} = (0\ 0\ 1/4)_c$  and  $(\overline{0.25}\ 0\ \overline{0.25})_c$ .

Figure 6.23 shows contour plots of the observed nuclear intensities for  $(hhl)_t$  and  $(h0l)_t$  planes of the reciprocal space at 3.5 K. For the first time,  $(\overline{2}\ \overline{2}\ \frac{3}{2})_t$  super structure reflection was observed in  $(hhl)$  plane which is indicated by the white circle. Although this could in principle be leak through (due to incomplete neutron polarization) from the strong magnetic peaks visible in the spin-flip channel, we considered this as a

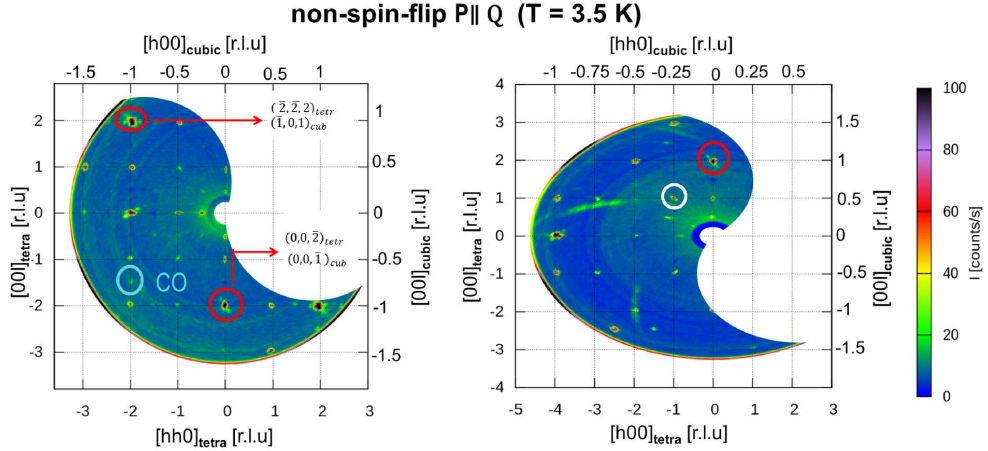


Figure 6.23: Scattered intensity in non-spin-flip channel with  $P \parallel x$  i.e., approximately  $\parallel$  to  $Q$ , measured in  $hhl$  - plane and  $h0l$  - plane at 3.5 K.

non-magnetic peak by comparing with the magnetic Bragg peak  $(\bar{2} \ \bar{2} \ \frac{1}{2})_t$ . The peak  $(\bar{2} \ \bar{2} \ \frac{1}{2})_t$  has more intensity compared to  $(\bar{2} \ \bar{2} \ \frac{3}{2})_t$  in the spin-flip channel. If the observed intensity in the non-flip channel was just by leak through, then the intensity ratios between  $(\bar{2} \ \bar{2} \ \frac{1}{2})_t$  and  $(\bar{2} \ \bar{2} \ \frac{3}{2})_t$  would be the same in spin-flip and non-spin-flip channels. Taking into account its disappearance at a temperature where Mössbauer spectroscopy [15] showed charge freezing, we tentatively concluded that the observed non-magnetic peak  $(\bar{2} \ \bar{2} \ \frac{3}{2})_t$  is a charge ordered reflection. In the tetragonal phase, Fe1 and Fe3 ions have +4 and the Fe2 ion have +3.5 valence states. At 70 K, Fe2 site (table 6.3) leads to charge ordering of the  $\text{Fe}^{3.5}$  to  $\text{Fe}^{3+}$  and  $\text{Fe}^{4+}$  [15, 158]. This was also supported by our observation of absence charge order reflection at 100 K [see figure 6.24]. This charge ordering produces a doubling of c-axis with respect to the cubic structure of the parent compound. With the identified propagation vector and site i.e. Fe2 (8f) there are four charge configurations possible as shown in the figure 6.22 at the four positions:  $\frac{1}{4} \ \frac{1}{4} \ \frac{1}{4}, \frac{3}{4} \ \frac{3}{4} \ \frac{1}{4}, \frac{3}{4} \ \frac{1}{4} \ \frac{1}{4}, \frac{1}{4} \ \frac{3}{4} \ \frac{1}{4}$  (four more possibilities arise when considering the I - centering operation, not shown). However, more extensive work is needed to determine the exact charge configuration.

The red circle in the figure 6.23 indicates the observed incommensurate lattice modulations with very large lattice periodicity and is temperature independent. Therefore we speculate that it is due to disordered oxygen vacancies. The origin of this lattice



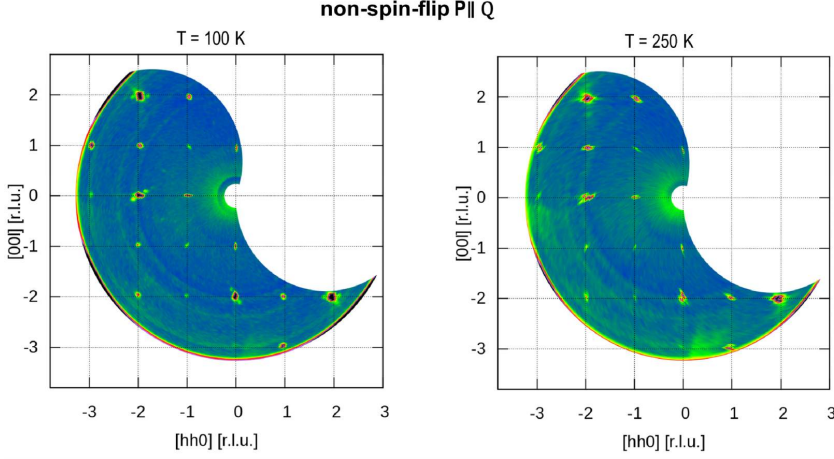


Figure 6.24: Scattered intensity in non-spin-flip channel with  $P \parallel x$  i.e., approximately  $\parallel$  to  $Q$ , measured in  $hhl$  - plane at different temperatures.

modulation is unknown. According to general reflection condition for primitive lattice ( $I$ ) only even reflections are allowed. The observed forbidden reflections, for e.g.,  $(\bar{2} \bar{2} 1)_{tetra}$ , are due to the presence of twin [see figure 6.17] which is equivalent to  $(1 1 \bar{2})_{twin2}$ .

### 6.5.2 Results $\text{SrFeO}_{3-\delta}$ ( $\delta \sim 0.35 \pm 0.03$ ):

Figure 6.25 shows contour plots of the observed magnetic and nuclear intensities for  $(hhl)$  plane of the reciprocal space at different temperatures. The polarization analysis was carried out with  $P \parallel x$  and hence approximately parallel to  $Q$ . The observed magnetic intensities were more diffuse compared to  $\delta = 0.27$  system.

The absence of intensity of the bragg reflection  $(0 0 \frac{1}{2})_t$  and  $(0.3 0.3 0.3)_t$  at 100 K clearly indicates that the structure belongs to tetragonal phase. The presence of weak intensity at 100 K, which is however absent below 200 K, indicates that the system contains a fraction of the cubic phase ( $T_N$  of cubic phase is 130 K). A weak diffuse scattering was observed around the nuclear Bragg peak in the non-spin-flip channel. The presence of this diffuse scattering could be because of the defects or disorder in the system induced by excess of oxygen vacancies. Fig 6.26 shows the contour plots of observed magnetic intensities for  $(hhl)$  plane of the reciprocal space at different temperatures. The measurement was carried out with the guide field direction parallel to  $z$ . Similar to  $\delta = 0.27$  system,

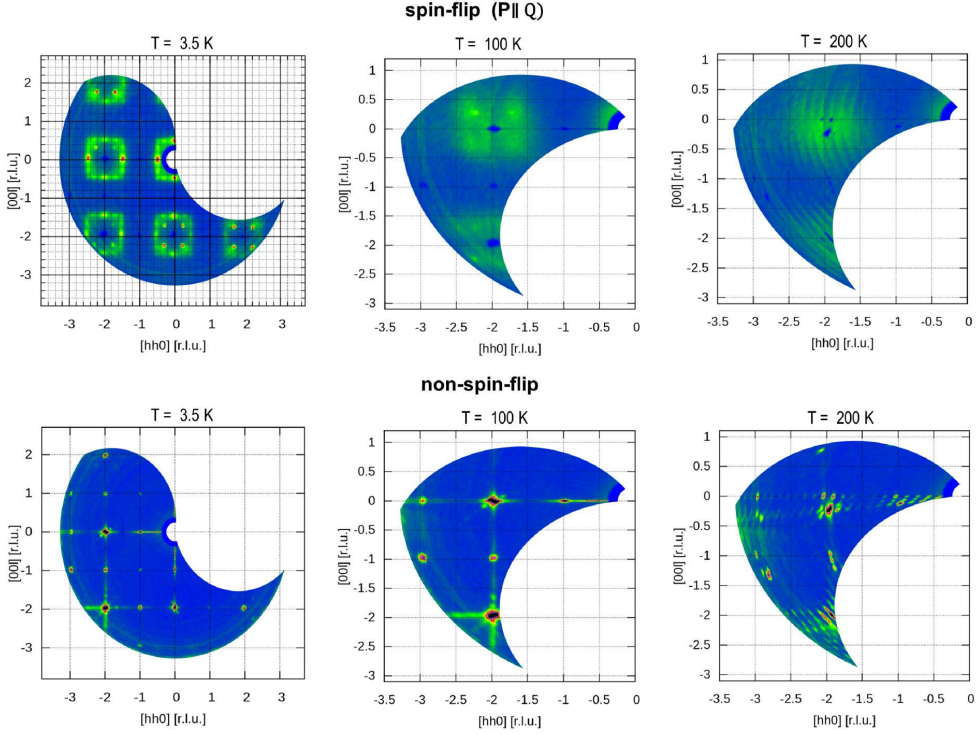


Figure 6.25: Polarization analysis with  $P \parallel x$  i.e.,  $P \parallel Q$ , measured in  $hhl$ -plane at 3.5 K, 100 K and 200 K. Upper panel represents  $hhl$ -plane in spin-flip channel and the lower panel represents  $hhl$ -plane in non-spin-flip channel.

the intensity of the Bragg reflections as well as the diffuse scattering was decreased by changing the field direction from  $x$  to  $z$ . This indicates that spins mostly lie in the  $ab$ -plane.

## 6.6 Summary

Oxygen deficient  $\text{SrFeO}_{3-\delta}$  with  $\delta \sim 0.27$  and 0.35 crystals were grown and characterized by x-ray and neutron powder diffraction (NPD). Rietveld refinement was performed with the combination of different phases in order to solve the crystal structure at room temperature, as well as at low temperature. Because of the superposition of different diffraction patterns from mixed-phases it was difficult to identify the exact crystal structure as the refinement results showed nearly the same low agreement factors. However, by considering the lowest AIC value and with respect to the fit we could best describe the data with a purely

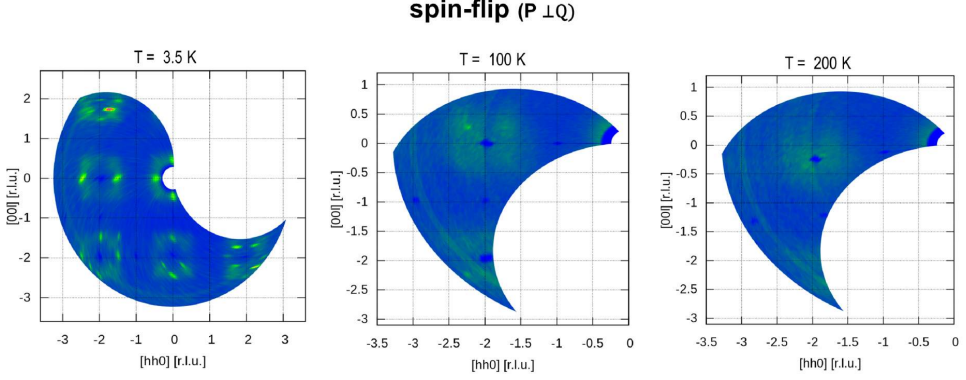


Figure 6.26: Scattered intensity in spin-flip channel with  $P \parallel Z$  i.e.,  $P \perp Q$ , measured in  $hhl$  - plane at 3.5 K, 100 K.

tetragonal phase. Although the presence of small fraction of cubic and orthorhombic phases was observed by further macroscopic and microscopic studies, this however could not be corroborated with the NPD data. This is mainly due to the instrumental resolution, which may not be high enough to see the small structural distortions.

To study the magnetic properties, magnetization and hysteresis measurements were performed. Magnetization measurements showed two anomalies corresponding to magnetic ordering of tetragonal (70 K) and orthorhombic (230 K) phases. For the first time, spin-glass like behavior was observed and confirmed by memory effect. Though the physical origin of this glassy nature is unknown, we attributed this to the presence of disorder, competing exchange interaction and the presence of spin frustrated  $\text{Fe}^{4+}$  magnetic moments of the orthorhombic phase.

Further, to study the magnetic structure and spin orientation, neutron scattering with  $xyz$  - polarization analysis was performed. Reciprocal space mapping of  $(hhl)$  and  $(h0l)$  showed that the crystal was heavily twinned by 90 degree. Though finding the magnetic structure was difficult with the presence of both twinning and different phases, several sets of magnetic Bragg reflections were indexed and compared with the recently reported seven magnetic structures in the series of oxygen deficiency systems. Several magnetic phases were matched, and the conclusion is that the crystal studied contains phase fractions of all three (cubic, tetragonal and orthorhombic) phases. Two additional magnetic peaks were identified at  $k = (0.25 \ 0.25 \ 0.25)_c$  and  $(0.25 \ 0 \ 0.15)_c$  which are inconsistent with any previously observed magnetic phases. The presence of diffuse scattering around the magnetic Bragg peak indicates the presence of short-range spin

correlation. Similar  $k$ -vectors were observed in the case of  $\delta = 0.35$ . However, intensities were more diffuse compared to  $\delta \sim 0.27$  system. This indicates the lack of long-range magnetic order with increased oxygen deficiency. In both the systems the presence of cubic phase was evidenced by the observation of Bragg reflection at the wave vector  $(0.15\ 0\ 0.15)_c$ . Cubic phase of  $\text{SrFeO}_3$  ( $T_N = 130\text{ K}$ ) exhibits helical spin ordering with the wave vector parallel to  $[111]$  direction. From the observation of microscopic and macroscopic experimental results it can be concluded that the  $T_N$  at  $130\text{ K}$  does not depend on the oxygen content in the system. Incommensurate lattice modulations were observed in  $\delta = 0.27$  system and are temperature independent. We speculate that it is due to the disordered vacancies in the crystal. More deficiency of oxygen lead to defects in the crystal, which were observed as diffuse scattering in non-spin flip channel of the  $\delta = 0.35$  system. For the first time we have observed a non-magnetic super structure reflection at  $(\bar{2}\ \bar{2}\ \frac{3}{2})_t$  position. As this reflection disappeared at  $70\text{ K}$  which corresponds to charge freezing according to a previous Mössbauer spectroscopy study, this is most likely a charge ordered superstructure reflection. In this case symmetry analysis suggested that only four charge ordered arrangements are possible. Further work is required to distinguish between these.



## Chapter 7

### Summary and Outlook

In this thesis I have investigated microscopic ferroelectric properties of multiferroic magnetite and various microscopic and macroscopic physical properties of oxygen-deficient strontium ferrite ( $\text{SrFeO}_3$ ).

Dielectric spectroscopy is a key technique to study the ferroelectric properties of any material. Although multiferroic and magnetoelectric materials are investigated heavily at our institute, a dielectric measurement setup was lacking. Therefore a new dielectric measurement system was developed as a part of the project. A new PPMS insert was designed in such a way that samples can be measured with electric field either in perpendicular or parallel to the external magnetic field. A LabVIEW program was developed, which enables a computer to communicate with the capacitance bridge and to control PPMS operations. The state of the art features of the ultra-precision capacitance bridge, AH 2700A, offers frequency range from 50 Hz to 20 kHz and can measure the accuracy for small-capacitance samples of better than 1 aF at 1 kHz. Test measurements on  $\text{MnWO}_4$  demonstrated the capability of the new setup. The investigation of a possibly multiferroic magnetite constituted the most important part of this thesis project.

The Verwey transition in magnetite is very sensitive to the ideal meta-oxygen stoichiometry. The best way to obtain high-quality crystals is the direct synthesis in an appropriate  $\text{CO}/\text{CO}_2$  flow. High quality polycrystalline samples were prepared by tuning the  $\text{CO}_2$  and  $\text{Ar}(\text{H}_2)_4$  gas ratios. The phase purity was confirmed by x-ray diffraction measurement. The verwey transition was preliminarily characterized by thermoremanent magnetization and heat capacity measurements. These results were used for the growth of high quality crystals. The crystals were grown by optical floating zone furnace by tuning the ratios of CO and  $\text{CO}_2$  gas mixtures. As grown high quality crystals were used for microscopic investigations by scattering experiments. In order to study the relaxor ferroelectric property of magnetite, diffuse scattering by high energy x-rays and neutrons below the verwey transition were performed on different quality crystals. We have observed a very weak diffuse scattering around  $\sim 3.5$  K by neutron scattering, which however, was absent in high energy x-ray scattering. Therefore, we have tentatively concluded that the observed diffuse scattering is magnetic in origin.

Very recently low temperature charge ordered structure of magnetite was solved and proved to be polar. However, for a material to be ferroelectric this polar structure needs to be switchable by an external electric field. In order to achieve that, for the first time we have performed a time resolved experiment to investigate the ferroelectric behavior of magnetite by monitoring the intensity of Bragg-peaks in an electric field. The observed

---

intensity difference of (2 -2 10) Bragg reflection to its inversion symmetry-related variant was 0.1%. This is less than expected based on our structure factor calculation, which was 3%, considering switching of all the 24 charge ordered domains. We could find two main reasons for this discrepancy in the intensity: (1) polarization of some of the domains are not aligned to electric field, so that effective projection of electric field to the polarization direction is small, (2) the presence of high temperature ( $\sim 11$  K) partially obscured the switching due to increased ohmic conductivity. Regardless of the weakness of the effect, this work gives an unambiguous microscopic proof of ferroic property of magnetite. Thus, we achieved the first proof of the mechanism of ferroelectricity originating from charge ordering in any material.

Another material studied in this thesis is non-stoichiometric  $\text{SrFeO}_{3-\delta}$ . This material exhibits four phases due to oxygen vacancy ordering: cubic (for  $\delta = 0$ ), tetragonal (for  $\delta = 0.125$ ), orthorhombic (for  $\delta = 0.25$ ) and brownmillerite (for  $\delta = 0.5$ ). For intermediate  $\delta$  the system is a phase mixture.  $\delta = 0.27$  and  $0.35$  crystals were grown by optical floating zone method using different growth conditions. The  $\delta$  was determined by chemical analysis by infrared absorption and structural refinement. Neutron powder diffraction and x-ray diffraction experiments were performed to solve the crystal structure. The data was best described with a purely tetragonal phase although the presence of cubic and orthorhombic phases were confirmed by further macroscopic and microscopic measurements. The reason for not observing the presence of these two phases could be due to the instrumental resolution. Three anomalies were observed by magnetization measurement. The anomaly around 70 K corresponds to  $T_N$  of tetragonal phase,  $\sim 130$  K corresponds to  $T_N$  of cubic phase and  $\sim 230$  K corresponds to  $T_N$  of orthorhombic phase. We have observed frequency dependence of AC-susceptibility below  $\sim 60$  K and memory effect in the low temperature phase. This indicates the presence of glassy state in the low temperature phase. In order to study the magnetic structure and spin orientation, neutron diffraction with  $xyz$ -polarization analysis was carried out. Observed results indicated that the majority of the spins lie in  $ab$ -plane. Several magnetic Bragg peaks were indexed. Majority of the  $k$ -vectors belong to tetragonal phase. New magnetic phases were observed at the propagation vector  $(0.25\ 0.25\ 0.25)_c$  and  $(0.25\ 0\ 0.15)_c$ . Incommensurate wave vectors with large lattice periodicity were observed in the  $\delta \sim 0.27$  system. Since these modulations were temperature independent we speculated that this is due to the disordered oxygen vacancies. For the first time we have observed a charge ordered reflection at  $(\bar{2}\ \bar{2}\ \frac{3}{2})_{tetra}$  position. The presence of short-range spin correlation was evidenced by the observation



of diffuse scattering in the spin-flip channel. With the decreasing oxygen content, the system is more disordered and diffuse scattering was more enhanced.

Despite the detailed study of ferroelectric behavior of magnetite, a few questions are still open. One amongst these is the absence of diffuse scattering related to relaxor ferroelectric. This leads to the question of whether magnetite is a relaxor ferroelectric in the classical sense or not. What is the origin of diffuse magnetic scattering, although it is very weak? Conclusive results for this could be obtained by polarization analysis. With the polarization analysis the intensity of the diffuse scattering can be greatly enhanced by resolving the magnetic diffuse scattering by suppressing the non-magnetic background. Since the magnetite is ferrimagnetic, which will depolarize the neutrons, the experiment needs to be performed under the magnetic field. Although our results of structural switching by electric field gave a first microscopic proof of ferroic behavior in magnetite, unambiguous proof requires switching of the several reflections, including the charge ordered reflection, within the available structure models. The confirmation would be relevant because this would constitute the first unambiguous proof of ferroelectricity from charge order in any material. Further, we propose to do the measurement by increasing the delay time between opposite polarities of the applied voltage to observe the decrease in the effective polarization with time, which gives the conclusive proof of proposed relaxor ferroelectricity in magnetite. A major problem with single crystals is that they are difficult to be prepared with thicknesses below  $\sim 1$  mm. Apparently, the voltage needed to switch the structure is also very high. Nevertheless, the voltage can be reduced by making the sample very thin or may be an epitaxial film on a suitable substrate can be the ultimate solution. Relatively larger polarization was observed in thin films compared to single crystals. The compound  $\text{SrFeO}_{3-\delta}$  is very complex and exhibits a variety of interesting properties, such as colossal magnetoresistance, spin-glass like behavior, charge ordering etc. The physics behind these variety of phenomena is still not clear. Although we have observed a charge ordering, an extensive work is needed to determine the exact charge. Overall results of oxygen deficient  $\text{SrFeO}_3$  indicated that the crystal is not in thermodynamic equilibrium and oxygen vacancies were not ordered in the system. Good way to obtain the homogeneous crystal is by post annealing the as grown crystal by oxygen pressure or by tuning the growth condition.

## BIBLIOGRAPHY

---



# Bibliography

- [1] N.F Mott. Metal-insulator transition. *Rev. Mod. Phys.*, 40(4):677, 1968.
- [2] Masatoshi Imada, Atsushi Fujimori, and Yoshinori Tokura. Metal-insulator transitions. *Rev. Mod. Phys.*, 70(4):1039, 1998.
- [3] E.J.W Verwey. Electronic conduction of magnetite ( $\text{Fe}_3\text{O}_4$ ) and its transition point at low temperatures. *Nature*, 144(3642):327–328, 1939.
- [4] John Bardeen, Leon N Cooper, and J Robert Schrieffer. Theory of superconductivity. *Phys. Rev.*, 108(5):1175, 1957.
- [5] J George Bednorz and K Alex Müller. Possible high  $T_c$  superconductivity in the Ba-La-Cu-O system. *Zeitschrift für Physik B Condensed Matter*, 64(2):189–193, 1986.
- [6] M. Fiebig. Revival of the magnetoelectric effect. *J. Phys. D: Appl. Phys.*, 38(8):R123, 2005.
- [7] W. Eerenstein, N. D. Mathur, and J. F. Scott. Multiferroic and magnetoelectric materials. *Nature*, 442(7104):759–765, 2006.
- [8] J. Volger. Further experimental investigations on some ferromagnetic oxidic compounds of manganese with perovskite structure. *Physica*, 20(1):49–66, 1954.
- [9] A. P. Ramirez. Colossal magnetoresistance. *J. Phys.: Condens. Matter*, 9(39):8171, 1997.
- [10] G. R. Stewart. Heavy-fermion systems. *Rev. Mod. Phys.*, 56(4):755, 1984.
- [11] Ch. Renner, G. Aeppli, B-G Kim, Yeong-Ah Soh, and S-W Cheong. Atomic-scale images of charge ordering in a mixed-valence manganite. *Nature*, 416(6880):518–521, 2002.

- 
- [12] J. A. Alonso, J. L. García-Muñoz, M. T. Fernández-Díaz, M. A. G. Aranda, M. J. Martínez-Lope, and M. T. Casais. Charge disproportionation  $\text{RNiO}_3$  perovskites: Simultaneous metal-insulator and structural transition in  $\text{YNiO}_3$ . *Phys. Rev. Lett.*, 82(19):3871, 1999.
- [13] J. A. Alonso, M. J. Martínez-Lope, M. T. Casais, J. L. García-Muñoz, and M. T. Fernández-Díaz. Room-temperature monoclinic distortion due to charge disproportionation in  $\text{RNiO}_3$  perovskites with small rare-earth cations ( $\text{R} = \text{Ho}, \text{Y}, \text{Er}, \text{Tm}, \text{Yb}, \text{and Lu}$ ): A neutron diffraction study. *Phys. Rev. B*, 61(3):1756, 2000.
- [14] M. J. Konstantinović, J. Dong, M. E. Ziaei, B. P. Clayman, J. C. Irwin, K. Yakushi, M. Isobe, and Y. Ueda. Charge ordering and optical transitions of  $\text{LiV}_2\text{O}_5$  and  $\text{NaV}_2\text{O}_5$ . *Phys. Rev. B*, 63(12):121102, 2001.
- [15] A. Lebon, P. Adler, C. Bernhard, A. V. Boris, A. V. Pimenov, A. Maljuk, C. T. Lin, C. Ulrich, and B. Keimer. Magnetism, charge order, and giant magnetoresistance in  $\text{SrFeO}_{3-\delta}$  single crystals. *Phys. Rev. Lett.*, 92:037202, 2004.
- [16] Yasusada Yamada, Shinichiro Nohdo, and Naoshi Ikeda. Incommensurate charge ordering in charge-frustrated  $\text{LuFe}_2\text{O}_4$  system. *Journal of the Physical Society of Japan*, 66(12):3733–3736, 1997.
- [17] M. Angst, Peter Khalifah, R. P. Hermann, H. J. Xiang, M-H Whangbo, Viji Varadarajan, Joseph W Brill, Brian C Sales, and David Mandrus. Charge order superstructure with integer iron valence in  $\text{Fe}_2\text{OBO}_3$ . *Phys. Rev. Lett.*, 99(8):086403, 2007.
- [18] I. D. Brown and D. Altermatt. Bond-valence parameters obtained from a systematic analysis of the inorganic crystal structure database. *Acta Crystallographica Section B: Structural Science*, 41(4):244–247, 1985.
- [19] I. D. Brown. Valence: a program for calculating bond valences. *J. Appl. Crystallogr.*, 29(4):479–480, 1996.
- [20] Jean-Louis Hodeau, Vincent Favre-Nicolin, Sandra Bos, Hubert Renevier, Emilio Lorenzo, and Jean-Francois Berar. Resonant diffraction. *Chem. Rev.*, 101(6):1843–1868, 2001.

- [21] X. S. Xu, M. Angst, T. V. Brinzari, R. P. Hermann, J. L. Musfeldt, Andrew D. Christianson, David Mandrus, B.C. Sales, Steve McGill, J-W Kim, et al. Charge order, dynamics, and magnetostructural transition in multiferroic  $\text{LuFe}_2\text{O}_4$ . *Phys. Rev. Lett.*, 101(22):227602, 2008.
- [22] <http://wwwchem.uwimona.edu.jm/courses/cft.html>.
- [23] Hermann Arthur Jahn and Edward Teller. Stability of polyatomic molecules in degenerate electronic states. i. orbital degeneracy. *Proceedings of the Royal Society of London. Series A, Mathematical and Physical Sciences*, pages 220–235, 1937.
- [24] Werner Heisenberg. Zur theorie des ferromagnetismus. *Zeitschrift für Physik*, 49(9-10):619–636, 1928.
- [25] Stuart B. Wilkins, Thomas A. W. Beale, Peter D Hatton, John A Purton, Peter Bencok, D. Prabhakaran, and Andrew T. Boothroyd. Probing orbital order with soft x-rays: the case of the manganites. *New Journal of Physics*, 7(1):80, 2005.
- [26] A.A. Abrikosov. *Fundamentals of the theory of metals*. Fundamentals of the Theory of Metals. North-Holland, 1988.
- [27] Mario Norberto Baibich, JM Broto, Albert Fert, F Nguyen Van Dau, F Petroff, P. Etienne, G. Creuzet, A. Friederich, and J. Chazelas. Giant magnetoresistance of (001) Fe/(001) Cr magnetic superlattices. *Phys. Rev. Lett.*, 61(21):2472, 1988.
- [28] Grünberg Binasch, Peter Grünberg, F Saurenbach, and W Zinn. Enhanced magnetoresistance in layered magnetic structures with antiferromagnetic interlayer exchange. *Phys. Rev. B*, 39:4828–4830, 1989.
- [29] S. Jin, Th. H. Tiefel, M. McCormack, R. A. Fastnacht, R. Ramesh, and L. H. Chen. Thousandfold change in resistivity in magnetoresistive La-Ca-Mn-O films. *Science*, 264(5157):413–415, 1994.
- [30] John B. Goodenough. Theory of the role of covalence in the perovskite-type manganites  $[\text{La}, \text{m(II)}]\text{MnO}_3$ . *Phys. Rev.*, 100:564–573, 1955.
- [31] John B. Goodenough. An interpretation of the magnetic properties of the perovskite-type mixed crystals  $\text{La}_{1-x}\text{Sr}_x\text{CoO}_{3-\lambda}$ . *J. Phys. Chem. Solids*, 6(2):287–297, 1958.

- 
- [32] Clarence Zener. Interaction between the  $d$ -shells in the transition metals. ii. ferromagnetic compounds of manganese with perovskite structure. *Phys. Rev.*, 82:403–405, 1951.
- [33] A. P. Ramirez, P. Schiffer, S. W. Cheong, C. H. Chen, W. Bao, T. T. M. Palstra, P. L. Gammel, D. J. Bishop, and B. Zegarski. Thermodynamic and electron diffraction signs of charge and spin ordering in  $\text{La}_{1-x}\text{Ca}_x\text{MnO}_3$ . *Phys. Rev. Lett.*, 76(17):3188, 1996.
- [34] Y. Tomioka, A. Asamitsu, Y. Moritomo, H. Kuwahara, and Y. Tokura. Collapse of a charge-ordered state under a magnetic field in  $\text{Pr}_{1/2}\text{Sr}_{1/2}\text{MnO}_3$ . *Phys. Rev. Lett.*, 74(25):5108, 1995.
- [35] Y. Moritomo, Y. Tomioka, A. Asamitsu, Y. Tokura, and Y. Matsui. Magnetic and electronic properties in hole-doped manganese oxides with layered structures:  $\text{La}_{1-x}\text{Sr}_{1+x}\text{MnO}_4$ . *Phys. Rev. B*, 51(5):3297, 1995.
- [36] K. Liu, X. W. Wu, K. H. Ahn, T. Sulchek, C. L. Chien, and John Q. Xiao. Charge ordering and magnetoresistance in  $\text{Nd}_{1-x}\text{Ca}_x\text{MnO}_3$  due to reduced double exchange. *Phys. Rev. B*, 54:3007–3010, 1996.
- [37] A. J. Millis, Boris I. Shraiman, and R. Mueller. Dynamic jahn-teller effect and colossal magnetoresistance in  $\text{La}_{1-x}\text{Sr}_x\text{MnO}_3$ . *Phys. Rev. Lett.*, 77:175–178, 1996.
- [38] A. Shengelaya, Guo-meng Zhao, H. Keller, and K. A. Müller. Epr evidence of jahn-teller polaron formation in  $\text{La}_{1-x}\text{Ca}_x\text{MnO}_{3+y}$ . *Phys. Rev. Lett.*, 77(26):5296, 1996.
- [39] A. Asamitsu, Y. Moritomo, Y. Tomioka, T. Arima, and Y. Tokura. A structural phase transition induced by an external magnetic field. *Nature*, 373(6703):407 – 409, 1995.
- [40] K-I Kobayashi, T. Kimura, H. Sawada, K. Terakura, and Y. Tokura. Room-temperature magnetoresistance in an oxide material with an ordered double-perovskite structure. *Nature*, 395(6703):677–680, 1998.
- [41] Takayoshi Takeda, Yasuo Yamaguchi, and Hiroshi Watanabe. Magnetic structure of  $\text{SrFeO}_3$ . *J. Phys. Soc. Jpn*, 33(4):967–969, 1972.

- [42] S. Kawasaki, M. Takano, and Y. Takeda. Ferromagnetic properties of  $\text{SrFe}_{1-x}\text{Co}_x\text{O}_3$  synthesized under high pressure. *Journal of Solid State Chemistry*, 121(1):174–180, 1996.
- [43] A. E. Bocquet, A. Fujimori, T. Mizokawa, T. Saitoh, H. Namatame, S. Suga, N. Kimizuka, Y. Takeda, and M. Takano. Electronic structure of  $\text{SrFe}^{4+}\text{O}_3$  and related fe perovskite oxides. *Phys. Rev. B*, 45(4):1561, 1992.
- [44] Hans Schmid. Multi-ferroic magnetoelectrics. *Ferroelectrics*, 162(1):317–338, 1994.
- [45] N. A. Spaldin and M. Fiebig. The renaissance of magnetoelectric multiferroics. *Science*, 309(5733):391, 2005.
- [46] Martin Gajek, Manuel Bibes, Stephane Fusil, Karim Bouzehouane, Josep Fontcuberta, Agnes Barthelemy, and Albert Fert. Tunnel junctions with multiferroic barriers. *Nature materials*, 6(4):296–302, 2007.
- [47] P. Curie. Sur la symétrie dans les phénomènes physiques, symétrie d’un champ électrique et d’un champ magnétique. *Journal de Physique théorique et appliquée* 3, pages 393–415, 1894.
- [48] D. N. Astrov. The magnetoelectric effect in antiferromagnetic materials. *Zhurnal Eksperimental’noi i Teoreticheskoi Fiziki*, 37:881, 1959.
- [49] D. N. Astrov. Magnetoelectric effect in chromium oxide. *Sov. Phys. JETP*, 13(4):729–733, 1961.
- [50] G. Lawes, M. Kenzelmann, N. Rogado, K. H. Kim, G. A. Jorge, R. J. Cava, A. Aharony, O. Entin-Wohlman, A. B. Harris, T. Yildirim, et al. Competing magnetic phases on a kagomé staircase. *Phys. Rev. Lett.*, 93(24):247201, 2004.
- [51] W. F. Brown, R. M. Hornreich, and S. Shtrikman. Upper bound on the magnetoelectric susceptibility. *Phys. Rev.*, 168:574–577, 1968.
- [52] Nicola A. Hill. Why are there so few magnetic ferroelectrics? *The Journal of Physical Chemistry B*, 104(29):6694–6709, 2000.
- [53] Ram Seshadri and Nicola A. Hill. Visualizing the role of bi 6s “lone pairs” in the off-center distortion in ferromagnetic  $\text{BiMnO}_3$ . *Chem. Mater.*, 13(9):2892–2899, 2001.



- [54] Sang-Wook Cheong and Maxim Mostovoy. Multiferroics: a magnetic twist for ferroelectricity. *Nature materials*, 6(1):13–20, 2007.
- [55] Bas B. Van Aken, Thomas T. M. Palstra, Alessio Filippetti, and Nicola A. Spaldin. The origin of ferroelectricity in magnetoelectric YMnO<sub>3</sub>. *Nature materials*, 3(3):164–170, 2004.
- [56] M. Kenzelmann, A. B. Harris, S. Jonas, C. Broholm, J. Schefer, S. B. Kim, C. L. Zhang, S.-W. Cheong, O. P. Vajk, and J. W. Lynn. Magnetic inversion symmetry breaking and ferroelectricity in TbMnO<sub>3</sub>. *Phys. Rev. Lett.*, 95:087206, 2005.
- [57] I. A. Sergienko and E. Dagotto. Role of the dzyaloshinskii-moriya interaction in multiferroic perovskites. *Phys. Rev. B*, 73:094434, 2006.
- [58] Qichang Li, Shuai Dong, and J.-M. Liu. Multiferroic response and clamped domain structure in a two-dimensional spiral magnet: Monte carlo simulation. *Phys. Rev. B*, 77:054442, 2008.
- [59] Hosho Katsura, Naoto Nagaosa, and Alexander V. Balatsky. Spin current and magnetoelectric effect in noncollinear magnets. *Phys. Rev. Lett.*, 95:057205, 2005.
- [60] Jiangping Hu. Microscopic origin of magnetoelectric coupling in noncollinear multiferroics. *Phys. Rev. Lett.*, 100:077202, 2008.
- [61] Y. J. Choi, H. T. Yi, S. Lee, Q. Huang, V. Kiryukhin, and S-W Cheong. Ferroelectricity in an ising chain magnet. *Phys. Rev. Lett.*, 100(4):047601, 2008.
- [62] Jeroen Van Den Brink and Daniel I. Khomskii. Multiferroicity due to charge ordering. *J. Phys.: Condens. Matter*, 20(43):434217, 2008.
- [63] Dmitry V. Efremov, Jeroen Van Den Brink, and Daniel I. Khomskii. Bond-versus site-centred ordering and possible ferroelectricity in manganites. *Nature materials*, 3(12):853–856, 2004.
- [64] P. Monceau, F. Ya. Nad, and S. Brazovskii. Ferroelectric mott-hubbard phase of organic (TMTTF)2X conductors. *Phys. Rev. Lett.*, 86:4080–4083, 2001.
- [65] Naoshi Ikeda, Hiroyuki Ohsumi, Kenji Ohwada, Kenji Ishii, Toshiya Inami, Kazuhisa Kakurai, Youichi Murakami, Kenji Yoshii, Shigeo Mori, Yoichi Horibe, et al.

- Ferroelectricity from iron valence ordering in the charge-frustrated system  $\text{LuFe}_2\text{O}_4$ . *Nature*, 436(7054):1136–1138, 2005.
- [66] J. de Groot, T. Mueller, R. A. Rosenberg, D. J. Keavney, Z. Islam, J-W Kim, and M. Angst. Charge order in  $\text{LuFe}_2\text{O}_4$ : An unlikely route to ferroelectricity. *Phys. Rev. Lett.*, 108(18):187601, 2012.
- [67] Kunihiko. Yamauchi, Tetsuya. Fukushima, and Silvia. Picozzi. Ferroelectricity in multiferroic magnetite  $\text{Fe}_3\text{O}_4$  driven by noncentrosymmetric  $\text{Fe}^{2+}/\text{Fe}^{3+}$  charge-ordering: First-principles study. *Phys. Rev. B*, 79:212404, 2009.
- [68] Hanna A. Dabkowska and Bruce D. Gaulin. Growth Of Oxides Single Crystals By The Optical Floating Zone Method. *International School on Crystal Growth of Technologically Important Electronic Materials*, page 341, 2003.
- [69] Shigeyuki Kimura and Kenji Kitamura. Floating zone crystal growth and phase equilibria: A review. *Journal of the American Ceramic Society*, 75(6):1440–1446, 1992.
- [70] Mike McElfresh. Fundamentals of magnetism and magnetic measurements. *Quantum Design, Inc*, 1994.
- [71] Quantum Design. Magnetic Property Measurement System: MPMS MultiVu Application User’s Manual.
- [72] Quantum Design. Magnetic Property Measurement System: SQUID VSM User’s Manual, 2009.
- [73] Quantum Design. Physical Property Measurement System: Vibrating Sample Magnetometer (VSM) Option User’s Manual, 2003.
- [74] L. Lundgren, P. Svedlindh, and O. Beckman. Measurement of complex susceptibility on a metallic spin glass with broad relaxation spectrum. *J. Magn. Magn. Mater.*, 25(1):33–38, 1981.
- [75] Quantum Design. Magnetic Property Measurement System: Heat Capacity Option User’s Manual, 2004.
- [76] Albrecht Messerschmidt. *X-ray crystallography of biomacromolecules: a practical guide*. John Wiley & Sons, 2007.

- [77] Thomas Brückel. Atomic and Magnetic Structures in Crystalline Materials: Neutron and X-ray Scattering. *ChemInform*, 39(32), 2008.
- [78] Marcus Frederick Charles Ladd and Rex Alfred Palmer. *Structure determination by X-ray crystallography*. Springer, 1985.
- [79] <http://www.ccp14.ac.uk/ccp/web-mirrors/lmgp-laugier-bochu/>.
- [80] <http://multiwire.com/index.shtml>.
- [81] Jörg Strempler, Sonia Francoual, D. Reuther, D Kumar. Shukla, A. Skaugen, H. Schulte-Schrepping, T. Kracht, and H. Franz. Resonant scattering and diffraction beamline P09 at PETRA III. *Journal of synchrotron radiation*, 20(4):541–549, 2013.
- [82] <http://www.aps.anl.gov/sectors/sector6/6idd/>.
- [83] Thomas. Brückel. *Polarized Neutron Scattering: Lectures of the 1st Summer School Held at the Forschungszentrum Jülich from 10 to 14 September 2002*. Schriften des Forschungszentrums Jülich : Materie und Material. Forschungszentrum Jülich GmbH - Zentralbibliothek, Verlag, 2002.
- [84] G.L. Squires. *Introduction to the Theory of Thermal Neutron Scattering*. Dover books on physics. Dover Publications, 1978.
- [85] P. Schweika, W. and Böni. The instrument DNS: polarization analysis for diffuse neutron scattering. *Physica B: Condensed Matter*, 297(1):155–159, 2001.
- [86] Thomas Brückel, G Heger, D Richter, and R Zorn. Neutron scattering. Lectures of the JCNS laboratory course held at Forschungszentrum Juelich and the research reactor FRM II of TU Munich, 2007.
- [87] Markus Hoelzel, Anatoliy Senyshyn, N Juenke, Hans Boysen, W Schmahl, and H Fuess. High-resolution neutron powder diffractometer SPODI at research reactor FRM II. *Nuclear Instruments and Methods in Physics Research Section A: Accelerators, Spectrometers, Detectors and Associated Equipment*, 667:32–37, 2012.
- [88] <http://www.mlz-garching.de/spodi>.
- [89] Karin M. Rabe, Charles H. Ahn, and Jean-Marc Triscone. *Physics of ferroelectrics: a modern perspective*, volume 105. Springer, 2007.

- [90] E.V. Colla, E. Yu. Koroleva, N. M. Okuneva, and S. B. Vakhrushev. Low-frequency dielectric response of  $\text{PbMg}_{1/3}\text{Nb}_{2/3}\text{O}_3$ . *J. Phys.: Condens. Matter*, 4(13):3671, 1992.
- [91] Dwight Viehland, S. J. Jang, L. Eric Cross, and Manfred. Wuttig. Freezing of the polarization fluctuations in lead magnesium niobate relaxors. *Journal of Applied Physics*, 68(6):2916–2921, 1990.
- [92] MN Avadhanulu and Kshir Sagar. A text book of engineering physics, s. *Chand & Co, New Delhi*, 2007.
- [93] D. Niermann, F. Waschowski, J. de Groot, M. Angst, and J. Hemberger. Dielectric Properties of Charge-Ordered  $\text{LuFe}_2\text{O}_4$  Revisited: The Apparent Influence of Contacts. *Phys. Rev. Lett.*, 109:016405, 2012.
- [94] A. H. Arkenbout, T. T. M. Palstra, T. Siegrist, and T. Kimura. Ferroelectricity in the cycloidal spiral magnetic phase of  $\text{MnWO}_4$ . *Phys. Rev. B*, 74(18):184431, 2006.
- [95] Daniel. I. Khomskii. Multiferroics: Different ways to combine magnetism and ferroelectricity. *J. Magn. Magn. Mater.*, 306(1):1–8, 2006.
- [96] Mark S. Senn, Jon P. Wright, and J Paul. Attfield. Charge order and three-site distortions in the verwey structure of magnetite. *Nature*, 481(7380):173–176, 2011.
- [97] F. Schrettle, S. Krohns, P. Lunkenheimer, V. A. M. Brabers, and A. Loidl. Relaxor ferroelectricity and the freezing of short-range polar order in magnetite. *Phys. Rev. B*, 83:195109, 2011.
- [98] J. García, G. Subías, M. G. Proietti, J. Blasco, H. Renevier, J. L. Hodeau, and Y. Joly. Absence of charge ordering below the verwey transition temperature in magnetite. *Phys. Rev. B*, 63:054110, 2001.
- [99] Gloria Subías, Joaquín García, Javier Blasco, M. Grazia Proietti, Hubert Renevier, and M. Concepción Sánchez. Magnetite, a model system for mixed-valence oxides, does not show charge ordering. *Phys. Rev. Lett.*, 93:156408, 2004.
- [100] E. Nazarenko, J. E. Lorenzo, Y. Joly, J. L. Hodeau, D. Mannix, and C. Marin. Resonant x-ray diffraction studies on the charge ordering in magnetite. *Phys. Rev. Lett.*, 97:056403, 2006.

- 
- [101] G. T. Rado and J. M. Ferrari. Linear and bilinear magnetoelectric effects in magnetically biased magnetite ( $\text{Fe}_3\text{O}_4$ ). *Phys. Rev. B*, 15(1):290, 1977.
- [102] K. Kato, S. Iida, K. Yanai, and K. Mizushima. Ferrimagnetic ferroelectricity of  $\text{Fe}_3\text{O}_4$ . *J. Magn. Magn. Mater.*, 31:783–784, 1983.
- [103] Marin Alexe, Michael Ziese, Dietrich Hesse, Pablo Esquinazi, Kunihiko Yamauchi, Tetsuya. Fukushima, Silvia. Picozzi, and Ulrich. Gösele. Ferroelectric switching in multiferroic magnetite ( $\text{Fe}_3\text{O}_4$ ) thin films. *Adv. Mater.*, 21(44):4452–4455, 2009.
- [104] J. P. Shepherd, J. W. Koenitzer, R. Aragón, J. Spalek, and J. M. Honig. Heat capacity and entropy of nonstoichiometric magnetite  $\text{Fe}_{3(1-\delta)}\text{O}_4$ : The thermodynamic of the verwey transition. *Phys. Rev. B*, 43:8461–8471, 1991.
- [105] Ricardo Aragón, Douglas J. Buttrey, John P. Shepherd, and Jurgen M. Honig. Influence of nonstoichiometry on the verwey transition. *Phys. Rev. B*, 31:430–436, 1985.
- [106] rdo Aragón, Harold R. Harrison, Robert. H. McCallister, and Charles J Sandberg. Skull melter single crystal growth of magnetite ( $\text{Fe}_3\text{O}_4$ )-ulvospinel ( $\text{Fe}_2\text{TiO}_4$ ) solid solution members. *Journal of Crystal Growth*, 61(2):221–228, 1983.
- [107] Ze Zhang and Sashi Satpathy. Electron states, magnetism, and the Verwey transition in magnetite. *Phys. Rev. B*, 44(24):13319, 1991.
- [108] Akira. Yanase and Noriaki. Hamada. Electronic structure in high temperature phase of  $\text{Fe}_3\text{O}_4$ . *J. Phys. Soc. Jpn*, 68:1607–1613, 1999.
- [109] E.J.W. Verwey and P. W. Haayman. Electronic conductivity and transition point of magnetite ( $\text{Fe}_3\text{O}_4$ ). *Physica*, 8(9):979–987, 1941.
- [110] E.J. Verwey, P. W. Haayman, and F. C. Romeijn. Physical properties and cation arrangement of oxides with spinel structures II. electronic conductivity. *J. Chem. Phys.*, 15:181, 1947.
- [111] P.W. Anderson. Ordering and antiferromagnetism in ferrites. *Phys. Rev*, 102(4):1008, 1956.
- [112] P. A. Miles, W. B. Westphal, and A. Von Hippel. Dielectric spectroscopy of ferromagnetic semiconductors. *Reviews of modern physics*, 29(3):279, 1957.

- [113] Walter C. Hamilton. Neutron diffraction investigation of the 119 K transition in magnetite. *Phys. Rev.* 110(5):1050, 1958.
- [114] M Iizumi, TF Koetzle, G Shirane, S Chikazumi, M Matsui, and S Todo. Structure of magnetite ( $\text{Fe}_3\text{O}_4$ ) below the verwey transition temperature. *Acta Crystallographica Section B: Structural Crystallography and Crystal Chemistry*, 38(8):2121–2133, 1982.
- [115] J. M Zuo, J. C. H. Spence, and W. Petuskey. Charge ordering in magnetite at low temperatures. *Phys. Rev. B*, 42(13):8451, 1990.
- [116] E. De Grave, R. M. Persoons, R. E. Vandenberghe, and P. M. A. de Bakker. Mössbauer study of the high-temperature phase of co-substituted magnetites,  $\text{Co}_x\text{Fe}_{3-x}\text{O}_4$ . I.  $x \leq 0.04$ . *Phys. Rev. B*, 47:5881–5893, 1993.
- [117] P. Novák, H. pánková, J. Englich, J. Kohout, and V. A. M. Brabers. Nmr in magnetite below and around the verwey transition. *Phys. Rev. B*, 61:1256–1260, 2000.
- [118] Toshiro Yamada, Kunio Suzuki, and Soshin Chikazumi. Electron microscopy of orthorhombic phase in magnetite. *Appl. Phys. Lett.*, 13(5):172–174, 1968.
- [119] Emil J. Samuelsen, E. J. Bleeker, L. Dobrzynski, and T. Riste. Neutron scattering from magnetite below 119 K. *Journal of Applied Physics*, 39(2):1114–1115, 1968.
- [120] Koji Chiba, Kunio Suzuki, and Soshin Chikazumi. Diffuse electron scattering from magnetite above the verwey transition temperature. *Journal of the Physical Society of Japan*, 39:839, 1975.
- [121] Yoshiko Miyamoto and Mikio Shindo. Magnetoelectric measurement of magnetite ( $\text{Fe}_3\text{O}_4$ ) at low temperatures and direct evidence for nonexistence of ac mirror plane. *Journal of the Physical Society of Japan*, 62(5):1423–1426, 1993.
- [122] Jon P. Wright, J Paul. Attfield, and Paolo G. Radaelli. Charge ordered structure of magnetite  $\text{Fe}_3\text{O}_4$  below the verwey transition. *Phys. Rev. B*, 66(21):214422, 2002.
- [123] Jon P. Wright, J Paul. Attfield, and Paolo G. Radaelli. Long range charge ordering in magnetite below the verwey transition. *Phys. Rev. Lett.*, 87(26):266401, 2001.
- [124] Koichi. Kato and Shuichi. Iida. Observation of ferroelectric hysteresis loop of  $\text{Fe}_3\text{O}_4$  at 4.2 K. *J. Phys. Soc. Jpn*, 51:1335, 1982.

- 
- [125] Masakazu Kobayashi, Yukikuni Akishige, and Etsuro Sawaguchi. Dielectric and conducting properties of single crystal of magnetite below the verwey point. *J. Phys. Soc. Jpn.*, 55(11):4044–4052, 1986.
- [126] G. T. Rado and J. M. Ferrari. Electric field dependence of the magnetic anisotropy energy in magnetite ( $\text{Fe}_3\text{O}_4$ ). *Phys. Rev. B*, 12:5166–5174, 1975.
- [127] R. D. King-Smith and David Vanderbilt. Theory of polarization of crystalline solids. *Phys. Rev. B*, 47:1651–1654, 1993.
- [128] Raffaele Resta. Macroscopic polarization in crystalline dielectrics: the geometric phase approach. *Rev. Mod. Phys.*, 66:899–915, 1994.
- [129] A. A. Bokov and Z Ye. Dielectric dispersion and critical behavior in relaxor ferroelectric  $\text{Pb}(\text{Mg}_{1/3}\text{Nb}_{2/3})\text{O}_3\text{--PbTiO}_3$ . *Appl. Phys. Lett.*, 77(12):1888–1890, 2000.
- [130] Ricardo Aragón. Magnetization and exchange in nonstoichiometric magnetite. *Phys. Rev. B*, 46(9):5328, 1992.
- [131] Hsin-Yu Lin, Yu-Wen Chen, and Chiuping Li. The mechanism of reduction of iron oxide by hydrogen. *Thermochimica Acta*, 400(1):61–67, 2003.
- [132] SATORU IZUMISA WA. Heat capacity and thermodynamic properties of nearly stoichiometric wiistite from 13 to 450 K. *American Mineralogist*, 81:973–981, 1996.
- [133] L Eric Cross. Relaxorferroelectrics: an overview. *Ferroelectrics*, 151(1):305–320, 1994.
- [134] A. A. Bokov and Z-G Ye. Recent progress in relaxor ferroelectrics with perovskite structure. In *Frontiers of Ferroelectricity*, pages 31–52. Springer, 2007.
- [135] Gerald Burns and F. H. Dacol. Glassy polarization behavior in ferroelectric compounds  $\text{Pb}(\text{Mg}_{1/3}\text{Nb}_{2/3})\text{O}_3$  and  $\text{Pb}(\text{Zn}_{1/3}\text{Nb}_{2/3})\text{O}_3$ . *Solid State Commun.*, 48(10):853–856, 1983.
- [136] I-K Jeong, T. W. Darling, J. K. Lee, Th Proffen, R. H. Heffner, J. S. Park, K. S. Hong, Wojtek Dmowski, and Takeshi Egami. Direct observation of the formation of polar nanoregions in  $\text{Pb}(\text{Mg}_{1/3}\text{Nb}_{2/3})\text{O}_3$  using neutron pair distribution function analysis. *Phys. Rev. Lett.*, 94(14):147602, 2005.

- [137] George A Samara. The relaxational properties of compositionally disordered  $\text{ABO}_3$  perovskites. *J. Phys.: Condens. Matter*, 15(9):R367, 2003.
- [138] H. You and Q. M. Zhang. Diffuse X-Ray Scattering Study of Lead Magnesium Niobate Single Crystals. *Phys. Rev. Lett.*, 79:3950–3953, 1997.
- [139] K. Hirota, Z.-G. Ye, S. Wakimoto, P. M. Gehring, and G. Shirane. Neutron diffuse scattering from polar nanoregions in the relaxor  $\text{Pb}(\text{Mg}_{1/3}\text{Nb}_{2/3})\text{O}_3$ . *Phys. Rev. B*, 65:104105, 2002.
- [140] T. R. Welberry, M. J. Gutmann, Hyungje Woo, D..J. Goossens, Guangyong Xu, C. Stock, W. Chen, and Z-G Ye. Single-crystal neutron diffuse scattering and monte carlo study of the relaxor ferroelectric  $\text{PbZn}_{1/3}\text{Nb}_{2/3}\text{O}_3$  (PZN). *J. Appl. Crystallogr.*, 38(4):639–647, 2005.
- [141] T. R. Welberry, D. J. Goossens, and M. J. Gutmann. Chemical origin of nanoscale polar domains in  $\text{PbZn}_{1/3}\text{Nb}_{2/3}\text{O}_3$ . *Phys. Rev. B*, 74(22):224108, 2006.
- [142] S. M. Shapiro, M. Iizumi, and G. Shirane. Neutron scattering study of the diffuse critical scattering associated with the verwey transition in magnetite ( $\text{Fe}_3\text{O}_4$ ). *Phys. Rev. B*, 14:200–207, 1976.
- [143] Kiiti Siratori, Yoshinobu Ishii, Yukio Morii, Satoru Funahashi, Sakae Todo, and Akira Yanase. Neutron Diffuse Scattering Study of the High Temperature Phase of  $\text{Fe}_3\text{O}_4$ -I, Determination of Atomic Displacements at the X Point in the Brillouin Zone. *J. Phys. Soc. Jpn.*, 67:2818–2827, 1998.
- [144] Y. Fujii, G. Shirane, and Y. Yamada. Study of the 123-K phase transition of magnetite by critical neutron scattering. *Phys. Rev. B*, 11:2036–2041, 1975.
- [145] Y. Yamada, N. Wakabayashi, and R. M. Nicklow. Neutron diffuse scattering in magnetite due to molecular polarons. *Phys. Rev. B*, 21(10):4642, 1980.
- [146] B. A. Calhoun. Magnetic and electric properties of magnetite at low temperatures. *Phys. Rev.*, 94:1577–1585, 1954.
- [147] C. Azimonte, E. Granado, H. Terashita, S. Park, and S. W. Cheong. Polar atomic displacements in multiferroics observed via anomalous x-ray diffraction. *Phys. Rev. B*, 81(1):012103, 2010.



- [148] Mario. Maglione and M. A. Subramanian. Dielectric and polarization experiments in high loss dielectrics: A word of caution. *Appl. Phys. Lett.*, 93(3):032902–032902, 2008.
- [149] B. Shri Prakash and K. B. R. Varma. Ferroelectriclike and pyroelectric behavior of  $\text{CaCu}_3\text{Ti}_4\text{O}_{12}$  ceramics. *Appl. Phys. Lett.*, 90(8):082903–082903, 2007.
- [150] Semen. Gorfman, Oleg. Schmidt, Michael. Ziolkowski, Marc. von Kozirowski, and Ullrich. Pietsch. Time-resolved x-ray diffraction study of the piezoelectric crystal response to a fast change of an applied electric field. *Journal of Applied Physics*, 108(6):064911–064911, 2010.
- [151] H. E. Bennett, R. L. Peck, D. K. Burge, and J. M. Bennett. Formation and growth of tarnish on evaporated silver films. *J. Appl. Phys.*, 40(8):3351–3360, 1969.
- [152] Semen Gorfman, Vladimir Tsirelson, Andreas Pucher, Wolfgang Morgenroth, and Ullrich Pietsch. X-ray diffraction by a crystal in a permanent external electric field: electric-field-induced structural response in- $\text{GaPO}_4$ . *Acta Crystallographica Section A: Foundations of Crystallography*, 62(1):1–10, 2005.
- [153] R. von Helmolt, J. Wecker, B. Holzapfel, L. Schultz, and K. Samwer. Giant negative magnetoresistance in perovskite like  $\text{La}_{2/3}\text{Ba}_{1/3}\text{MnO}_x$  ferromagnetic films. *Phys. Rev. Lett.*, 71:2331–2333, 1993.
- [154] Ken-ichi Chahara, Toshiyuki Ohno, Masahiro Kasai, and Yuzoo Kozono. Magnetoresistance in magnetic manganese oxide with intrinsic antiferromagnetic spin structure. *Appl. Phys. Lett.*, 63:1990, 1993.
- [155] B. Raveau, M. Hervieu, A. Maignan, and C. Martin. The route to CMR manganites: what about chargeordering and phase separation? *J. Mater. Chem.*, 11(1):29–36, 2001.
- [156] M.S. Reis, A. M. Gomes, J. P. Araújo, P. B. Tavares, I. S. Oliveira, and V. S. Amaral. Positive and ‘colossal’ magnetocaloric effect due to charge ordering in CMR manganites. *J. Magn. Magn. Mater.*, 272:2393–2394, 2004.
- [157] Andrew J. Millis, Peter B. Littlewood, and Boris I. Shraiman. Double exchange alone does not explain the resistivity of  $\text{La}_{1-x}\text{Sr}_x\text{MnO}_3$ . *Phys. Rev. Lett.*, 74(25):5144, 1995.

- [158] P. Adler, A. Lebon, V. Damjanović, C. Ulrich, C. and Bernhard, A. V Boris, A Maljuk, C. T Lin, and B Keimer. Magnetoresistance effects in  $\text{SrFeO}_{3-\delta}$ : Dependence on phase composition and relation to magnetic and charge order. *Phys. Rev. B*, 73(9):094451, 2006.
- [159] P. K. Gallagher, J. B. MacChesney, and D. N. E Buchanan. Mössbauer effect in the system  $\text{SrFeO}_{2.5-3.0}$ . *J. Chem. Phys.*, 41(8):2429–2434, 2004.
- [160] J. B. MacChesney, R. C. Sherwood, and J. F. Potter. Electric and magnetic properties of the strontium ferrates. *J. Chem. Phys.*, 43(6):1907–1913, 2004.
- [161] J. P Hodges, S. Short, J. D. Jorgensen, X. Xiong, B. Dabrowski, S. M Mini, and C. W Kimball. Evolution of Oxygen-Vacancy Ordered Crystal Structures in the Perovskite Series  $\text{Sr}_n\text{Fe}_n\text{O}_{3n1}$  ( $n= 2, 4, 8$ , and), and the Relationship to Electronic and Magnetic Properties. *Journal of Solid State Chemistry*, 151(2):190–209, 2000.
- [162] Y. Takeda, K. Kanno, T. Takada, O. Yamamoto, M. Takano, N. Nakayama, and Y. Bando. Phase relation in the oxygen nonstoichiometric system,  $\text{SrFeO}_x$  ( $2.5 \leq x \leq 3.0$ ). *Journal of Solid State Chemistry*, 63(2):237–249, 1986.
- [163] M. Schmidt and S. J. Campbell. Crystal and Magnetic Structures of  $\text{Sr}_2\text{Fe}_2\text{O}_5$  at Elevated Temperature. *Journal of Solid State Chemistry*, 156(2):292–304, 2001.
- [164] Hitoshi Oda, Yasuo Yamaguchi, Humihiko Takei, and Hiroshi Watanabe. Single Crystal Neutron Diffraction Study of  $\text{SrFeO}_{3-x}$  ( $x= 0.1$ ). *J. Phys. Soc. Jpn*, 42(1):101–106, 1977.
- [165] M. Reehuis, C. Ulrich, A. Maljuk, Ch. Niedermayer, B. Ouladdiaf, A. Hoser, T. Hofmann, and B. Keimer. Neutron diffraction study of spin and charge ordering in  $\text{SrFeO}_{3-\delta}$ . *Phys. Rev. B*, 85(18):184109, 2012.
- [166] A. Maljuk, J. Stremper, C. Ulrich, and C. T Lebon, A .and Lin. Growth and characterization of high-quality  $\text{SrFeO}_x$  single crystals. *Journal of crystal growth*, 257(3):427–431, 2003.
- [167] G. V. M. Williams, E. K Hemery, and D. McCann. Magnetic and transport properties of  $\text{SrFeO}_x$ . *Phys. Rev. B*, 79(2):024412, 2009.

- 
- [168] R. Vidya, P. Ravindran, H. Fjellvåg, and A. Kjekshus. Spin-and charge-ordering in oxygen-vacancy-ordered mixed-valence  $\text{Sr}_4\text{Fe}_4\text{O}_{11}$ . *Phys. Rev. B*, 74(5):054422, 2006.
- [169] X. L. Wang, J. Horvat, H. K. Liu, A. H. Li, and S. X. Dou. Spin glass state in  $\text{Gd}_2\text{CoMnO}_6$  perovskite manganite. *Solid State Commun.*, 118(1):27–30, 2001.
- [170] X.L. Wang, M. James, J. Horvat, F. Gao, A.H. Li, and S.X. Liu, H.K.and Dou. Structure and spin glass behaviour in non-metallic  $\text{Yb}_2\text{CoMnO}_6$  perovskite manganite. *J. Magn. Magn. Mater.*, 246(1):86–92, 2002.
- [171] Yasuhiko Syono, Atsuko Ito, and Osamu Horie. Mössbauer Study on the Structural and Magnetic Properties of Amorphous  $\text{BaO-Fe}_2\text{O}_3\text{-B}_2\text{O}_3$  System. *J. Phys. Soc. Jpn*, 46(3):793–801, 1979.
- [172] Y. Yeshurun, M. B. Salamon, K. V. Rao, and H. S. Chen. Spin-Glass-Ferromagnetic Critical Line in Amorphous Fe-Mn Alloys. *Phys. Rev. Lett.*, 45:1366–1369, 1980.
- [173] J. Hubsch and G. Gavoille. Semi-spin-glass behavior in the  $\text{Co}_2\text{TiO}_4$  compound. *Phys. Rev. B*, 26:3815–3823, 1982.
- [174] Eduard Obradó, Antoni Planes, and Benjamín Martínez. Spin-glass transition in Cu-Al-Mn shape-memory alloys. *Phys. Rev. B*, 59:11450–11457, 1999.
- [175] J. O. Andersson, J. Mattsson, and P. Nordblad. Overlap length in a cu-mn spin glass probed by ac susceptibility. *Phys. Rev. B*, 48:13977–13980, 1993.
- [176] John A. Mydosh. *Spin glasses: an experimental introduction*, volume 125. Taylor & Francis London, 1993.
- [177] Josep Nogués and Ivan K Schuller. Exchange bias. *J. Magn. Magn. Mater*, 192(2):203–232, 1999.
- [178] Florin Radu and Hartmut Zabel. Exchange bias effect of ferro-/antiferromagnetic heterostructures. In *Magnetic heterostructures*, pages 97–184. Springer, 2008.
- [179] William H Meiklejohn and Charles P Bean. New magnetic anisotropy. *Phys. rev*, 105(3):904, 1957.

- [180] S. Srinath, M. Mahesh Kumar, M. L Post, and H Srikanth. Magnetization and magnetoresistance in insulating phases of  $\text{SrFeO}_3$ . *Physical review. B, Condensed matter and materials physics*, 72(5), 2005.
- [181] M. Schmidt, M. Hofmann, and S. J Campbell. Magnetic structure of strontium ferrite  $\text{Sr}_4\text{Fe}_4\text{O}_{11}$ . *J. Phys.: Condens. Matter*, 15(50):8691, 2003.
- [182] Werner Schweika. XYZ-polarisation analysis of diffuse magnetic neutron scattering from single crystals. In *J. Phys.: Conf. ser*, volume 211, page 012026. IOP Publishing, 2010.
- [183] Thomas Brückel, Gernot Heger, Dieter Richter, Georg Roth, and Reiner Zorn. *Neutron Scattering Lectures of the JCNS Laborator Course held at Forschungszentrum Jülich and the research reactor FRM II of TU Munich In cooperation with RWTH Aachen and University of Münster*, volume 39. Forschungszentrum Jülich, 2012.
- [184] <http://tiny.cc/hchwfy>.



# Acknowledgements

This work could not have been possible without the help of many people. First and foremost I would like to express my sincere gratitude to my doctoral thesis advisor Prof. Dr. Manuel Angst. Thank you for giving me the opportunity to work with you. I always enjoyed the privileges and freedom you gave me to explore and learn. Your profound physics insight and constant presence provided me with great guidance in the course of my PhD. I would like to thank Prof. Dr. Uwe Klemradt for agreeing to take the second revision of this thesis. I am always grateful to Prof. Dr. Thomas Brückel for giving me the opportunity to work in his institute.

During my studies I had the opportunity to work together with many collaborators. Our time resolved experiment at the beamline P09 wouldn't be possible without the help of Semen, Stefan, Pavel, Hyeokmin and Dr. Joerge Stremper. It was a lot of fun to work with you all. My special thanks to Prof. Dr. Joachim Hemberger for his timely help in characterizing the sample. I would like to thank Dr. Yixi Su and Dr. Kirill Nemkovskiy for their help during experiment at the instrument DNS and Dr. Anatoliy Senyshyn for carrying out the measurement at SPODI. I would like to thank Dr. Benedikt Klobes (my wonderful office mate) and Jürgen lauer for their help in developing LabVIEW program. I would like to thank DP Jörg Perßon and Mr. Berthold Schmitz for their assistance in laboratory. I extend my heart filled thanks to all the people from the institute scattering methods for their kind help and helpful discussions during my PhD time. My special thanks to Joost, Pankaj, Thomas, Haiely and Giorgi, the members of the Young Investigators Group "Complex Ordering Phenomena in Multifunctional Oxides". I truly enjoyed working with you all. My gratitude to secretary, Frau. Barbara Köppchen, for her help with arranging accommodation and assisting with all the administrative work. I really admire your patience and efficient work.

I would like to thank my previous supervisors Dr. Vishnu Prasad Bhotla, Prof. H. L Bhat and Dr. Suja Elizabeth for giving me the opportunity to work in their lab at IISc.

If I look back my journey towards Jülich with my broken English and leaving away my lovely family for the first time, I wonder how I could survive so far and emerged as a strong person! All the credits goes to you Naveen! You were the guardian for me since the time I landed in Germany. Thank you for all your support, immense care, love and help from near and far. The memories are always cherishing. Uday, how can I forget those days! I still remember those drops of water in your eyes seeing my awful situation. Thank you for being with me whenever I was in need and thanks for all the help and care you showed me. Hari, you being around in Jülich means a huge moral support for me. I enjoyed our chit chat and scientific discussions during lunch time. Thank you for all the help. Sayee, without you our small family in Jülich is incomplete. I enjoyed our dinner together and those dances :). Pankaj, I got to know you as a person since my last year of PhD. I can only say that you are a wonderful human being, who is ready to help anybody and everybody in Jülich. Thank you for cooking for me whenever I had no time to have dinner and thank you for all your help and care. I am always grateful to you. Without you guys my life in Jülich and my PhD wouldn't have been so easy.

My heart filled thanks to our Indian janatha in Jülich. Those weekend parties and celebrations were always cheerful during the stressful PhD days. My special thanks to tea-friend Raji and Christian. Our evenings walk in the campus and outing in the weekends were always refreshing. Thank you Raji for your help when I was sick and in the hospital.

My dear pals Nicky, Dona and Poornima- thank you for your immense love and care. You guys are always very special for me.

I can't thank enough the members of my giant family. Naming each one of you takes half a thesis. Thank you one and all for your love, care, affection and the support. You people are always my backbone! Amma, its because of you who I am today. Thank you for all the sacrifices you made for us. I owe you everything!

Band / Volume 121

**Scanning tunneling microscopy of single-molecule magnets and hybrid-molecular magnets: Two approaches to molecular spintronics**

V. Heß (2016), x, 127 pp

ISBN: 978-3-95806-128-6

Band / Volume 122

**Bulk and surface sensitive energy-filtered photoemission microscopy using synchrotron radiation for the study of resistive switching memories**

M. C. Patt (2016), viii, 247 pp

ISBN: 978-3-95806-130-9

Band / Volume 123

**Group IV Epitaxy for Advanced Nano- and Optoelectronic Applications**

S. Wirths (2016), vi, 116, XXX pp

ISBN: 978-3-95806-132-3

Band / Volume 124

**Strained Silicon-Germanium/Silicon Heterostructure Tunnel FETs for Low Power Applications**

S. Blaeser (2016), iv, 91, xvii pp

ISBN: 978-3-95806-135-4

Band / Volume 125

**Nanocavity Arrays for Extracellular Recording and Stimulation of Electroactive Cell Systems**

A. Czeschik (2016), x, 162 pp

ISBN: 978-3-95806-144-6

Band / Volume 126

**Band Structure Engineering in 3D Topological Insulators Investigated by Angle-Resolved Photoemission Spectroscopy**

M. Eschbach (2016), VIII, 153 pp

ISBN: 978-3-95806-149-1

Band / Volume 127

**Dynamics in colloid and protein systems: Hydrodynamically structured particles, and dispersions with competing attractive and repulsive interactions**

J. Riest (2016), ix, 226 pp

ISBN: 978-3-95806-153-8

Band / Volume 128

**Self-purifying  $\text{La}_{2/3}\text{Sr}_{1/3}\text{MnO}_3$  epitaxial films: Observation of surface precipitation of  $\text{Mn}_3\text{O}_4$  particles for excess Mn ratios**

A. Steffen (2016), 154 pp

ISBN: 978-3-95806-162-0



Band / Volume 129

**Strain and electric field mediated manipulation of magnetism  
in  $\text{La}_{(1-x)}\text{Sr}_x\text{MnO}_3/\text{BaTiO}_3$  heterostructures**

M. Schmitz (2016), VI, 141 pp

ISBN: 978-3-95806-164-4

Band / Volume 130

**High-Throughput Live-Cell Imaging for Investigations of Cellular  
Heterogeneity in *Corynebacterium glutamicum***

S. Helfrich (2016), xvi, 217 pp

ISBN: 978-3-95806-167-5

Band / Volume 131

**Laser-Induced Ultrafast Electron- and Spin-Dynamics in the Electronic  
Band Structure of Co(001)**

M. A. Plötzing (2016), ii, 109, XXXIV pp

ISBN: 978-3-95806-168-2

Band / Volume 132

**Robot-Assisted Phenotyping of Genome-Reduced *Corynebacterium  
glutamicum* Strain Libraries to Draft a Chassis Organism**

S. Unthan (2016), 122 pp

ISBN: 978-3-95806-169-9

Band / Volume 133

**Characterization of amino acid ammonia lyases & aminomutases  
for the production of chiral  $\alpha$ - and  $\beta$ -amino acids**

A. Dreßen (2016), ix, 112 pp

ISBN: 978-3-95806-176-7

Band/Volume 134

**7th Georgian-German School and Workshop in Basic Science**

Kacharava, A. (Ed.) erscheint nur als CD (2016)

ISBN 978-3-95806-179-8

Band / Volume 135

**Crystal growth and scattering studies on two ferrites**

S. Adiga (2016), iv, 150 pp

ISBN: 978-3-95806-183-5

Weitere **Schriften des Verlags im Forschungszentrum Jülich** unter

<http://www.zb1.fz-juelich.de/verlagextern1/index.asp>



**Schlüsseltechnologien /**  
**Key Technologies**  
**Band / Volume 135**  
**ISBN 978-3-95806-183-5**

